THÈSE POUR OBTENIR LE GRADE DE DOCTEUR DE L'UNIVERSITÉ DE MONTPELLIER

En Électronique

École doctorale I2S - Information Structures et Systèmes

IES - Institut d'Electronique et des Systèmes

Impact of circuit modelling and low energy particles on Single-Event Effect rate prediction

Présentée par Cleiton MAGANO MARQUES
le 20 Février 2025

Sous la direction de Frédéric WROBEL et Alain MICHEZ

Devant le jury composé de

Fernanda KASTENSMIDT, Professeur, Universidade Federal do Rio Grande do Sul	Rapporteur
Florent MILLER, Ingénieur, Nucletudes	Rapporteur
Karine COULIÉ, Maîtresse de conférences, Aix Marseille Université	Examinateur
Jerôme BOCH, Professeur, Université de Montpellier, IES	Président du Jury
Ygor AGUIAR, Ingénieur, CERN	Membre invité
Frédéric WROBEL, Professeur, Université de Montpellier, IES	Directeur de thèse
Alain MICHEZ, Maître de conférences, Université de Montpellier, IES	Encadrant

UNIVERSITÉ DE MONTPELLIER

List of Figures

1.1 Overview of RADNEXT work packages [20]. 15

1.2 Overview of SEE modeling approaches. This work can be divided in three main approaches: Analytical methods, Monte Carlo simulations, and TCAD simulations. 15

2.1 Space Radiation Environment [21]. 17

2.2 Flux of galactic cosmic ray particles [23]. 18

2.3 Energy spectrum of galactic cosmic ray particles [24]. 19

2.4 Solar Cycle Flux Progression [28]. 20

2.5 Van Allen's Radiation Belts [21]. 21

2.6 Flux intensity map showing the distribution of protons with energies above 10 MeV at an altitude of 500 km. The higher proton flux are concentrated in the South Atlantic Anomaly (SAA) region [29]. 22

2.7 Cascade of secondary particles generated by the interaction of cosmic rays with atmosphere [31]. 22

2.8 Atmospheric particle flux as a function of altitude [34]. 23

2.9 Different accelerator setups: (a) Linear structure and (b) cyclotron structure [40]. 25

2.10 CERN accelerator complex: The LHC is the final stage of a chain composed of five accelerators[42]. 26

2.11 Variation of LET as a function of energy for several ions that may result from neutron interactions with silicon [44]. The proton (p) and alpha (α) labels are associated to Hydrogen (H) and Helium (He) ions, respectively. 28

2.12 Representation of Direct Ionization and Indirect Ionization for heavy ions, neutrons and protons interaction with matter [45]. 29

2.13 Charge collection mechanisms due to an ion strike in a p-n junction: (a) ion track, (b) drift process, and (c) diffusion process. [1]. 29

2.14 Double-exponential current injection: (a) NMOS and (b) PMOS strikes. 32

3.1 Neutron differential flux given by two standards JEDEC [36] (for ground level application) and IEC [37] for avionic applications. For the sake of comparison, IEC flux has been divided per 300. 36

3.2 IEC spectra divided by 300 in the 1-10 MeV energy range. The red line is a fit of the spectrum with a power law. 37

3.3 IEC spectra divided by 300 in the 1-100 GeV energy range. The red and the black lines are a fit with a power law respectively below and above 300 MeV. . . 37

3.4 Illustration of cross-section versus neutron energy in a typical case (where the onset is between 1 and 10 MeV) and the worst-case scenario yielding the highest SER. 39

3.5 Experimental cross-sections for the interaction of neutron with ^{28}Si in the 1-10 MeV energy range [36]. There is no data for neutron absorption. 41

3.6 cumulative distribution of production rate of silicon at ground level for the neutron energy range of 1-10 MeV and 1-200 MeV. 42

3.7 Illustration of the relationship between the threshold LET and the range of the particle. 43

3.8 I_S and I_V as a function of LET for atmospheric neutrons in the 1 MeV–200 MeV energy range. I_S (left y-axis) is the contribution to the SER to be multiplied by the visible area of the sensitive volume. I_V (right y-axis) is the contribution to the SER to be multiplied by the size of the sensitive volume. This is calculated using DHORIN [67]. 46

3.9 Comparison between the SER (at ground level) obtained by Monte Carlo simulations and the analytical approach developed in this document. 48

3.10 I_V calculation as a function of LET threshold for atmospheric neutrons in the 1-10 MeV energy range. 49

3.11 I_S calculation as a function of LET threshold for atmospheric neutrons in the 1-10 MeV energy range. 49

3.12 Relative contribution of the 1–10 MeV energy range compared to the 1–200 MeV range to the functions I_S and I_V as a function of threshold LET. 50

4.1 Elastic reaction leading to the deflection of the incident nucleon and the recoil of the target nucleus. The recoil ion may be responsible for an SEE. 54

4.2 Nonelastic reaction leading to the production of secondary particles. The secondaries may ionize the matter and trigger SEE. 54

4.3 Nuclear cross-sections for p + ^{28}Si interaction. Data from IAEA data [84]. . . . 55

4.4 Differential cross-section for incident neutrons and protons at 5 MeV and as a function of recoiling energy. 57

4.5 Differential cross-section for incident neutrons and protons at 10 MeV and as a function of recoiling energy. 57

4.6 Elastic cross-section as a function of proton energy for different threshold energies. 58

4.7 Illustration of an elastic collision in the BEOL. The recoiling silicon loses energy along its track and can reach the sensitive region with different LET. 59

4.8 Cumulative probability to obtain a silicon recoil with a LET $> LET_{th}$ for different proton energies. In this example, the BEOL thickness is 10 μm. The sensitive region layer is 1 μm. 61

4.9 90 nm SRAM results: (a) Heavy-ion cross-section fitted with a power law and (b) SEU cross-section calculation. Experimental data taken from [88]. 63

4.10 65 nm SRAM results: (a) Heavy-ion cross-section fitted with a power law and (b) SEU cross-section calculation. Experimental data taken from [87]. 64

4.11 40 nm SRAM results: (a) Heavy-ion cross-section fitted with a power law and (b) SEU cross-section calculation. Experimental data taken from [88]. 65

5.1 The diffusion–collection model: (a) the carriers arriving to the OFF-state drain at a given time t, and a given distance r, of the ion generation point; (b) segmentation of the ion track and the drain surface [97]. 70

5.2 Example of the I_{DS} vs V_{DS} curves for different V_{GS} values of simplified NMOS transistor with the W/L = 1. 71

5.3 Standard 6T SRAM electrical diagram. 72

5.4 Simplified flowchart of PredicSEE code. 73

5.5 Three different layout designs that can be applied to 6T SRAM cell: (a) “tall” design [101]; (b) “thin” design [99]; (c) “ultra-thin" design [102]. 75

5.6 PredicSEE view of the simplified 3D structure used in the simulations. The BEOL is modeled with SiO_2. 77

5.7 Heavy-ion SEU cross-section for 90 nm SRAM. Experimental data taken from [106]. 78

5.8 Heavy-ion SEU cross-section for 65 nm SRAM. Experimental data taken from [101]. 78

5.9 Heavy-ion SEU cross-section for 45 nm SRAM. Experimental data taken from [107]. 79

5.10 Heavy-ion SEU cross-section for 32 nm SRAM. Experimental data taken from [108]. 80

5.11 Heavy-ion SEU cross-section for 65nm SRAM considering the voltage scaling situation. Experimental data taken from [101]. 80

5.12 Heavy-ion SEU cross-section for 65 nm SRAM with variation in different input parameters. The standard plot is the golden result using the following input parameters: CR = 1.5, Layout = ”Tall”, BEOL = 8 μm, and Doping = $10^{18} atoms/cm^3$. For the other curves, we would only see one of the parameters and observe the simulation response. The cell ratio curve applies an CR = 2.0. The layout curve uses the “Thin” layout approach. The no layout curve does not follow a layout structure, just spacing the transistors for each other. The BEOL curve applies BEOL thickness of 3 μm. The doping curve uses the N-P WELL = $10^{17} atoms/cm^3$. 82

6.1 Structure of the 2D TCAD bulk-planar transistor implemented on ECORCE. . . 86

6.2 The I_{drain} vs V_{gate} curve of the NMOS transistor for 65 nm modeling. 87

6.3 Transistor SEU cross-section estimation methodology: (a) x-axis injection and (b) area estimation. 89

6.4 Total SEU cross-section of the cell. Blue rectangular area is the NMOS SEU cross-section, while the orange area is estimated by the cell ratio (CR=1.5). . . . 89

6.5 Heavy-ion SEU cross-section for 65 nm SRAM. Experimental data taken from [101]. 90

6.6 Heavy-ion SEU cross-section for 45 nm SRAM. Experimental data taken from [107]. 91

7.1 Cylindrical geometry and structure of the SBD used for simulations. 94

7.2 First step: generation of electron-hole pairs and displacement of charges depending on the electric field ($t = 0$). 98

7.3 Second step: charges are separated by the electric field, a high positive charge appears at the contact. The electric field in the epi layer is reduced, while the electric field increases near the Schottky contact. It speeds up the pair separation at this point. 98

7.4 Third step: the impact ionization is triggered. Additional pairs are generated by impact ionization (yellow). The electric field is limited when the impact ionization rate is high enough. 98

7.5 Chart to compare the Si and SiC properties [133]. 99

7.6 Impact ionization rate as a function of electric field for Si (blue) and SiC (red). . 101

7.7 Simulation results as a function of time: (a) Power heat density, (b) Electric field, and (c) Temperature. The red dots highlight the diode burnout point. . . . 102

7.8 Band-to-Band tunneling as a function of time. Burnout occurs only for red curve.The maximum BTT is highlighted for each curve. 105

7.9 Impact ionization rate as a function of time. Burnout occurs only for red curve. The maximum impact ionization rate is highlighted for each curve. 105

7.10 Impact ionization rate as a function of temperature. 106

7.11 Band-to-Band tunneling as a function of temperature. 107

7.12 Band-to-Band tunneling as a function of electric field. 107

8.1 Controler FPGA Module with AMD Artix™ 7A35T-2C [139]. 113

8.2 Memory daughter board. 113

8.3 40 nm SRAM neutron beam test setup. 114

List of Tables

3.1 Contribution of four main energy ranges to the SER in the framework of the worst-case analysis, assuming constant SEE cross-sections for neutrons above 1 MeV. Calculations use the IEC standard flux divided by 300 to estimate ground-level contributions. 39

3.2 Reaction products as a function of incident energy for low energy neutrons (1-10 MeV) interacting with ^{28}Si [66]. 40

3.3 Comparison between the SER (at ground level) obtained by Monte Carlo simulations and the analytical approach developed in this document. 47

4.1 Reaction products as a function of incident energy for neutrons and protons in ^{28}Si below 10 MeV. 54

4.2 Typical critical charge (Qc), LET_{th}, and E_{th} for different technologies. 58

4.3 Typical recoiling ranges of ions in silicon. 58

5.1 Simplified model; basic parameters for different technologies [95]. 69

6.1 TCAD parameters for different technology nodes [50, 95] 87

7.1 Electrical and Thermal models for SiC [124, 125, 126, 127, 128] 96

7.2 Parameters for Si and SiC SBD structures. 97

7.3 Ionization coefficients for Si and 4H-SiC used in ECORCE modeling [128, 129] . 100

8.1 Specification of tested devices. 112

Contents

1 Context **13**

1.1 Objectives and Contributions 15

1.2 Thesis Organization 16

2 Radiation effects background **17**

2.1 Radiation Environments 17

2.1.1 Galactic Cosmic Rays 18

2.1.2 Solar cosmic rays 19

2.1.3 Belt trapped particles 20

2.1.4 Atmospheric radiation 21

2.1.5 Experimental radiation 24

2.2 Radiation Effects in Electronics 26

2.2.1 Energy Deposition 26

2.2.2 Charge collection 29

2.3 SEE modeling and prediction 30

2.3.1 Circuit level simulation 31

2.3.2 Device level simulation 32

2.3.3 Alternative modeling approaches 33

2.4 Conclusion 34

3 Impact of low-energy Neutrons on SER **35**

3.1 Neutrons in Earth's atmosphere 36

3.2 Methodology to Evaluate the Soft Error Rate (SER) 38

3.2.1 Worst case scenario 38

3.3 Neutron interaction in 1-10 MeV energy range 39

3.4 Development of a simplified tool to evaluate SER 41

3.4.1 Ion generation rate and probability to reach the sensitive volume 41

3.4.2 Ion range and Threshold LET 43

3.4.3 Probability to trigger a soft error . . . 44
3.4.4 Soft Error Rate Calculation . . . 45
3.5 Main Results and Discussions . . . 46
3.5.1 Contribution of the 1-10 MeV energy range to the SER . . . 47
3.6 Conclusions . . . 50

4 SEE cross-section analysis for low-energy Protons 52
4.1 Nuclear-matter interaction background . . . 53
4.2 Approach to calculate SEE cross-section . . . 55
4.2.1 Nuclear Elastic cross-section Analysis . . . 56
4.2.2 Typical Ion Recoiling Ranges . . . 58
4.2.3 Energy loss modeling . . . 59
4.2.4 Cumulative probability calculation . . . 60
4.3 Results and discussion . . . 62
4.4 Conclusions . . . 66

5 Heavy-Ions SEE predictions using Monte Carlo tool 67
5.1 Circuit modeling . . . 67
5.1.1 Electrical model . . . 68
5.1.2 SEE triggering model . . . 69
5.2 The proposed methodology . . . 71
5.3 Simulation Setup . . . 73
5.3.1 Circuit-level description . . . 74
5.3.2 Layout-level parameters . . . 74
5.3.3 SEE analysis . . . 76
5.4 Experimental data vs. simulation results . . . 77
5.5 Impact of the input parameters . . . 81
5.6 Conclusions . . . 82

6 SEU cross-section estimation using 2D TCAD modeling 84
6.1 Proposed modeling . . . 85
6.1.1 TCAD modeling and parameters . . . 85
6.1.2 SPICE implementation . . . 87
6.1.3 SEU cross-section calculation . . . 88
6.2 Experimental data validation . . . 90
6.3 Influence of different TCAD parameters on the accuracy . . . 91

6.4 conclusions 92

7 Modeling SiC Schottky diodes susceptibility for SEB 93

7.1 Schottky diode modeling 94

7.2 Main mechanism of thermal runaway 97

7.3 TCAD modeling results 99

7.3.1 Impact ionization modeling 99

7.3.2 Thermal runaway results 101

7.3.3 Band-to-band tunneling analysis 104

7.4 Conclusion 107

8 Conclusions 109

8.1 Thesis summary 109

8.2 Contributions to the RADNEXT EU Project 110

8.3 Future works 116

Abstract

As microelectronic technology continues to scale down, electronic devices have become increasingly sensitive to radiation effects, particularly Single Event Effects (SEE). The study of SEE characterization relies heavily on the use of radiation testing. However, experimental activities are complex, time-consuming, and costly. In this context, modeling and prediction tools offer a complementary alternative to predict behavior before testing and to understand post-irradiation data. However, obtaining realistic parameters for modeling the simulations can be challenging, as they are typically confidential or not openly available from manufacturers. Furthermore, depending on the method used, the modeling may require a high computational effort, which impacts in very long simulations. Given the importance of SEE modeling and the obstacles associated with traditional methods, it is crucial to explore alternative modeling approaches that can overcome these limitations. This thesis investigates the impact of circuit modeling and low-energy particles on the prediction of SEE, focusing on alternative and simplified approaches. The study encompasses different methodologies, including analytical modeling, Monte Carlo simulations, electrical models, and Technology Computer-Aided Design (TCAD), to explore the advantages and limitations of these alternative modeling approaches, while providing significant insights into critical concerns related to radiation effects on electronic components.

Résumé

À mesure que la technologie microélectronique continue de se miniaturiser, les dispositifs électroniques deviennent de plus en plus sensibles aux effets des radiations, en particulier les effets d'événements uniques (SEE). L'étude de la caractérisation des SEE repose largement sur l'utilisation des tests de radiation. Cependant, les activités expérimentales sont complexes, longues et coûteuses. Dans ce contexte, les outils de modélisation et de prédiction offrent une alternative complémentaire pour prédire le comportement avant les tests et comprendre les données post-irradiation. Toutefois, l'obtention de paramètres réalistes pour la modélisation des simulations peut être un défi, car ces derniers sont généralement confidentiels ou non accessibles publiquement auprès des fabricants. De plus, selon la méthode utilisée, la modélisation peut nécessiter un effort de calcul important, ce qui entraîne des simulations très longues. Étant donné l'importance de la modélisation des SEE et les obstacles associés aux méthodes traditionnelles, il est crucial d'explorer des approches alternatives de modélisation qui puissent surmonter ces limitations. Cette thèse étudie l'impact de la modélisation des circuits et des particules de basse énergie sur la prédiction des SEE, en se concentrant sur des approches alternatives et simplifiées. L'étude englobe différentes méthodologies, notamment la modélisation analytique, les simulations de Monte Carlo, les modèles électriques et la conception assistée par ordinateur (TCAD), afin d'explorer les avantages et les limitations de ces approches alternatives, tout en apportant des éclairages significatifs sur les préoccupations majeures liées aux effets des radiations sur les composants électroniques.

Chapter 1

Context

As electronic technologies continue to shrink, they become increasingly sensitive to external interactions, such as temperature variations, noise, and particularly radiation effects [1, 2, 3, 4]. The deposition of energy by a single energetic particle in the sensitive areas of a circuit can result in both destructive and non-destructive failures, known as Single-Event Effects (SEE). Nowadays, SEE has become a major reliability concern for electronic systems, making their characterization essential for applications in radiation-prone environments such as aerospace, particle accelerators, and safety-critical systems [5, 6, 7, 8].

Research into radiation effects on electronic systems began in the 1960s. *J.T. Wallmark and S.M. Marcus* [9] were the first to show that cosmic rays could cause ionization and atomic displacements in semiconductor materials, resulting in temporary failures or permanent damage. However, it was not until 1975 that the first anomalies attributed to space radiation were documented. *D. Binder et al.* [10] identified that anomalies in satellite communication were due to unexpected bit-flipping in flip-flop circuits, induced by cosmic rays. In 1978, *T.C. May and M.H. Woods* [11] reported failures in dynamic random-access memories (DRAM) at sea level, caused by particles emitted during the decay of radioactive elements that had contaminated the packaging material during manufacturing. This study introduced the term "Soft Errors" to distinguish transient faults from permanent ones. By 1979, *C.S. Guenzer et al.* [12] linked Soft Errors to nuclear reactions induced by high-intensity protons and neutrons, coining the term Single Event Upset (SEU), which remains widely referenced in the literature today.

With the advancement of microelectronics and the miniaturization of circuits, SEE became increasingly significant in the early 2000s. The rising number of failures reported by telecommunications companies, high-end servers, and Cisco's computer networks demonstrated the significant impact of SEE. The Semiconductor Industry Association (SIA) recognized soft errors as one of the major threats to future electronic systems [13]. Since then, numerous studies have been conducted to better understand and mitigate the impact of radiation-induced faults on electronics [14, 15, 16, 17, 18].

T. Granlund and N. Olsson [14], in their research involving neutron testing at Los Alamos National Laboratory, demonstrated that the Soft Error Rate (SER) increased as semiconductor process technology scaled down below 0.25 μm. This observation contradicted earlier expectations that SER would decrease with smaller technology nodes.

Their findings revealed that newer generations of SRAM, manufactured using processes as small as 0.16 μm, were significantly more susceptible to soft errors. This heightened vulnerability was attributed to factors such as reduced critical charge (Q_{crit}) and decreased charge collection efficiency.

O.A. Amusan et al. [15] presented an analysis of charge-sharing effects between adjacent NMOS and PMOS transistors, showing that OFF-state PMOS transistors collected significantly more charge than OFF-state NMOS transistors. The authors attributed this behavior to the differences in the diffusion coefficients of electrons and holes, as well as the bipolar amplification effect, which increased charge collection in PMOS devices.

N.N. Mahatme et al. [16] further contributed to understanding SEE by demonstrating that, despite expectations that combinational logic errors would dominate beyond the 65 nm technology node, experimental data revealed that sequential logic errors still played a significant role even at the 32 nm node. Their work introduced models to explain the frequency dependence of combinational logic errors and highlighted critical factors influencing the SER, such as charge collection efficiency, sensitive area, and the critical charge required for errors to occur.

L. Artola [17] explored the effects of elevated temperatures on Single Event Transients (SETs) in CMOS devices for technologies beyond the 65 nm node. Their analysis used the MUSCA SEP3 platform and Cadence simulations to model the behavior of CMOS logic cells under high-temperature conditions, showing that increased temperatures led to broader SET pulse widths, thereby increasing the likelihood of SEUs.

More recently, *S. Vartanian* [18] presented an analysis of SEE testing on several Commercial-Off-The-Shelf (COTS) microcontrollers and microprocessors, focusing on Analog Devices components to evaluate their resilience in radiation environments.

In this context, emerging applications in industrial sectors such as space, automotive, the Internet of Things (IoT), nuclear dismantling, medical devices, and accelerators require innovative radiation testing and modeling methodologies. In response to industrial demand and market timelines, streamlined and coordinated testing is becoming highly necessary. For this reason, the European Union's Horizon 2020 research and innovation program approved a project to create a network of facilities and related irradiation methodologies aimed at addressing the emerging needs of electronic component and system irradiation.

The Europe Union RADiation facility Network for EXploration of effects for indusTry and research (RADNEXT) is a an international project that aims to create a network of facilities and related irradiation methodology for responding to the emerging needs of electronics component and system irradiation [19]. It also seeks to combine different irradiation and simulation techniques to optimize radiation hardness assurance for systems, with a particular focus on risk assessment. Figure 1.1 presents the structure of the RADNEXT project.

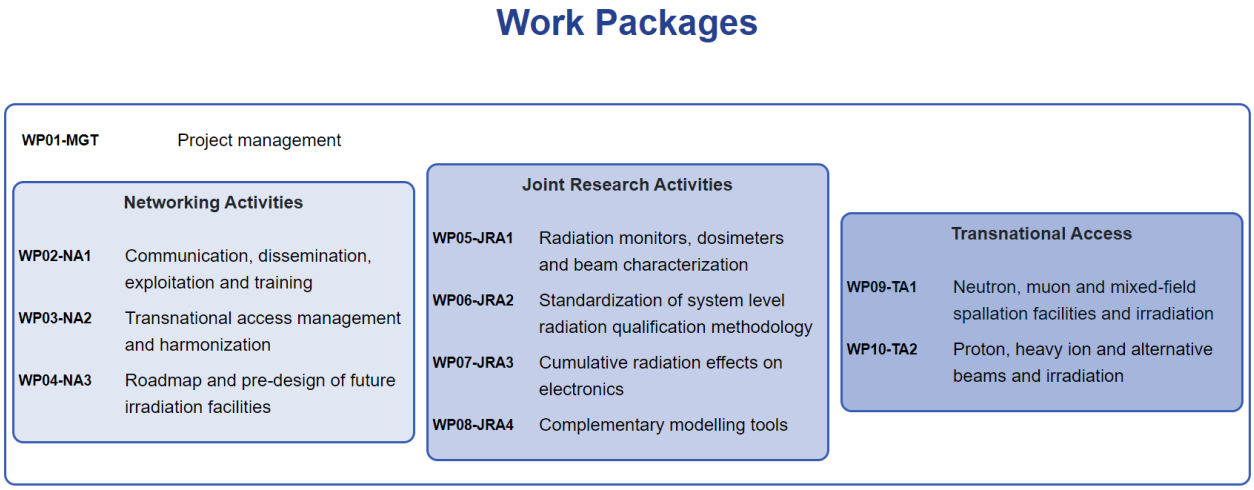

Figure 1.1: Overview of RADNEXT work packages [20].

1.1 Objectives and Contributions

This PhD thesis is part of work package 8 (WP08-JRA4), which aims to develop and apply alternative approaches for modeling radiation effects on electronics. These approaches require a multi-physics perspective that takes into account radiation-matter interaction, semiconductor physics, and circuit-level behavior. The modeling efforts will focus on benchmarking simulation tools to complement experimental data, enhancing the understanding and interpretation of results, and extending the applicability of these models to scenarios inaccessible through experimental methods. Another key objective is to establish SEE equivalences between different radiation fields, thereby expanding qualification alternatives when requirements between testing and application are comparable. Figure 1.2 provides a overview of the contributions of this thesis.

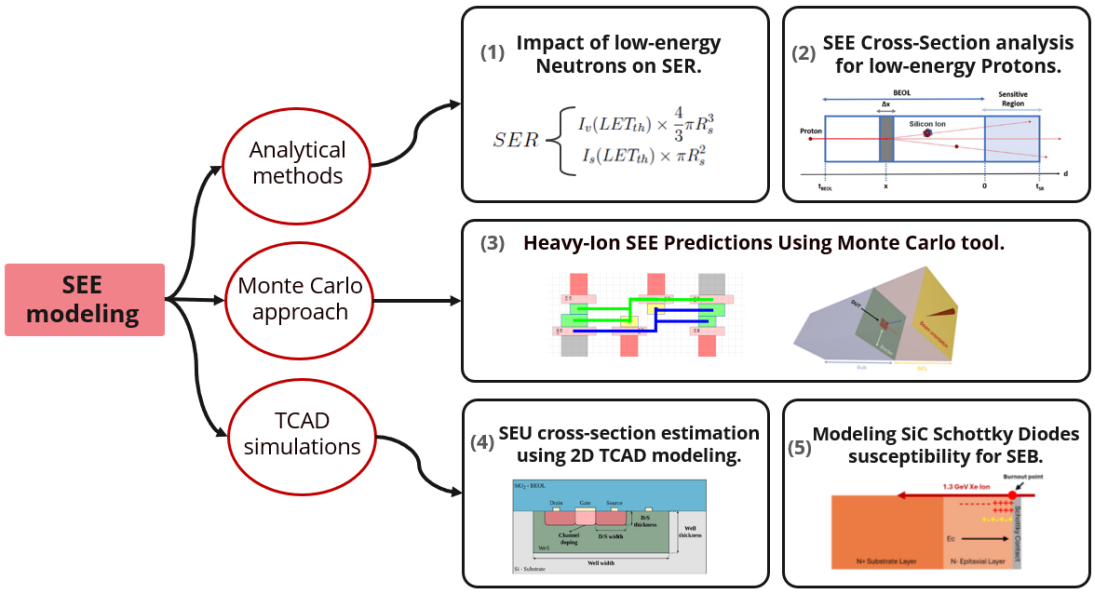

Figure 1.2: Overview of SEE modeling approaches. This work can be divided in three main approaches: Analytical methods, Monte Carlo simulations, and TCAD simulations.

1.2 Thesis Organization

In Chapter 2, the radiation sources and basic mechanisms of particle interaction with matter are described to provide an understanding of the dynamics of radiation environments and the prominent effects observed in electronic components. Chapter 3 derives an analytical method to facilitate the calculation of the SER with a minimum number of input parameters and evaluates the contribution of neutrons in the 1–10 MeV energy range to determine if there is a trend with technology downscaling. Chapter 4 provides a methodology for evaluating SEE induced by low-energy protons, highlighting that the Coulomb elastic process on the nucleus is a major source of SEE for protons within the energy range of 1–10 MeV. Chapter 5 proposes a simplified multi-physics methodology to predict the SEE cross-section, overcoming challenges related to the lack of technological information and simulation complexity. In Chapter 6, an innovative approach for estimating the SEU cross-section using two-dimensional TCAD modeling is introduced. Chapter 7 presents a comprehensive TCAD modeling of the primary mechanism responsible for heavy-ion-induced degradation in SiC devices, demonstrating that the high critical electric field (a key advantage of SiC devices) is the primary factor contributing to their susceptibility. Finally, Chapter 8 presents a summary of the results obtained in this thesis and a discussion on prospective future research in this subject area.

Chapter 2

Radiation effects background

Electronic circuits and systems are continuously exposed to various forms of radiation in space, atmospheric, and terrestrial environments. Assessing the reliability of electronic components operating in these harsh environments is critical to avoid functional failures or catastrophic consequences, especially in high-stakes applications such as space missions or nuclear industries. This chapter lays the groundwork for understanding the sources, dynamics, and radiation effects that influence electronics.

2.1 Radiation Environments

The radiation environment can be broadly categorized into two main sources: natural radiation and man-made radiation. Natural radiation mainly comes from space, including sources like solar activity and galactic cosmic rays, which are pervasive in near-Earth space. Figure 2.1 illustrates these natural radiation sources, which are crucial for understanding the challenges that space environments pose to electronic systems.

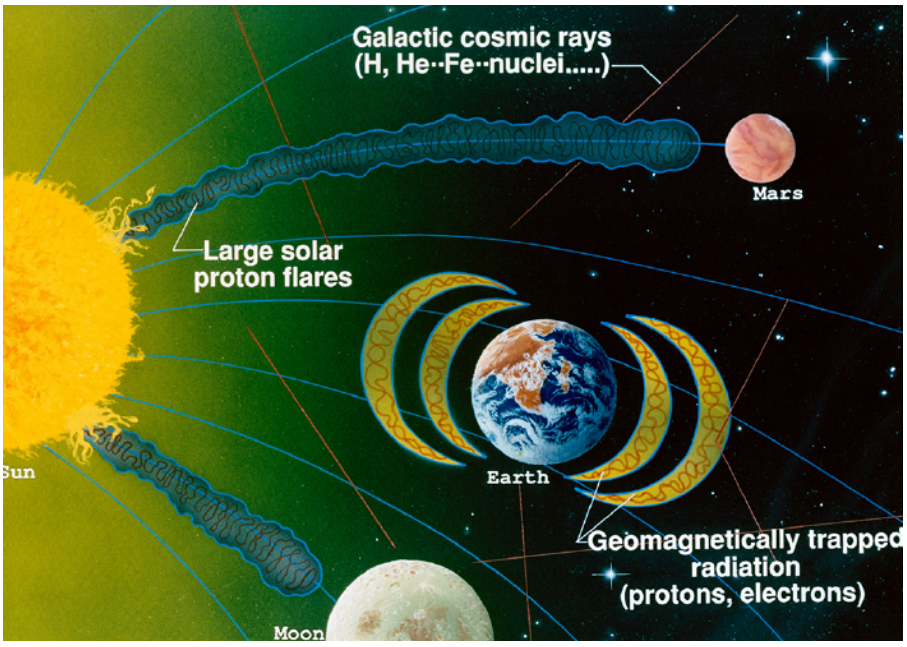

Figure 2.1: Space Radiation Environment [21].

Galactic cosmic rays and solar energetic particles can have significant implications for electronics, especially for long-duration missions and satellites in high-altitude orbits. Meanwhile, man-made radiation is generated by technological activities such as medical radiotherapy, nuclear reactors, high-energy particle accelerators, and semiconductor manufacturing processes. These radiation sources are often used intentionally for specific purposes, but they can also inadvertently expose electronic systems to high radiation levels, particularly in settings like hospitals, industrial facilities, or during the operation of particle accelerators.

2.1.1 Galactic Cosmic Rays

Galactic Cosmic Rays (GCRs) are highly energetic particles that come from outside the solar system, primarily from supernova remnants in the Milky Way. GCRs consist predominantly of protons (87%), alpha particles (12%), and heavier ions (1%) [22]. These particles travel close to the speed of light and permeate interstellar space, frequently bombarding Earth's atmosphere and near-Earth space.

Although Earth's atmosphere and magnetic field offer substantial protection, GCRs still pose a significant threat to spacecraft electronics, particularly for deep space missions and high-altitude aircraft. The GCR flux is especially concerning its cumulative damaging effects on sensitive electronic components. Figure 2.2 illustrates the flux distribution of GCR ions, with "H" representing Hydrogen atom (correlated with protons contribution) and "He" representing Helium (correlated with alpha particles contribution). The other atoms in the figure represent the minor contribution of different heavy ions. Figure 2.3 shows the energy spectrum of GCRs. Notably, the peak flux of protons occurs at an energy of approximately 300 MeV/nucleon. Protons with energies above 100 MeV primarily originate from the Milky Way, while those below this energy are largely sourced from solar activity [23, 24].

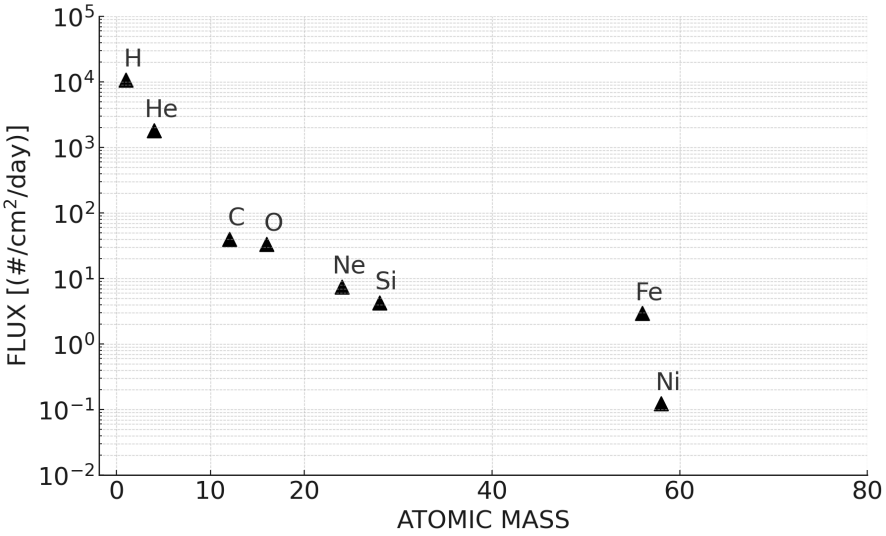

Figure 2.2: Flux of galactic cosmic ray particles [23].

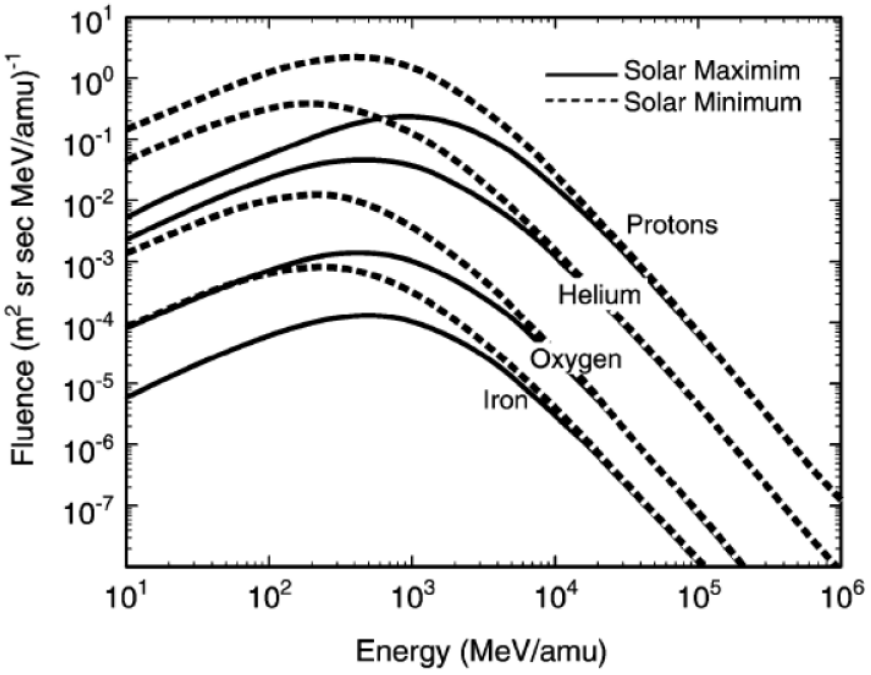

Figure 2.3: Energy spectrum of galactic cosmic ray particles [24].

2.1.2 Solar cosmic rays

Solar Cosmic Rays (SCRs), also known as Solar Energetic Particles (SEPs), are high-energy particles originating from the Sun. SCRs differ from GCRs in several key aspects, including energy levels, origins, and distribution patterns. Whereas GCRs are relatively isotropic and homogeneous, SCRs have a clear directional origin, directly linked to solar activity [25].

SCRs are primarily generated during solar events such as solar flares and coronal mass ejections (CMEs). These events release a large number of high-energy particles that can reach Earth's atmosphere in a short period, ranging from a few hours to a few days. The intensity of SCRs events is measured in terms of particle flux, (typically expressed as $particles/(cm^2.s.sr)$) and measures the number of particles passing through one square centimeter of area per second, per steradian of solid angle. This is essential in space physics to quantify not only the intensity of particle flow but also its directionality, which is particularly relevant for solar particle events impacting Earth. During intense SEP events, proton fluxes can exceed 10,000 $particles/(cm^2.s.sr)$ at energies greater than 10 MeV [26].Solar flares release bursts of energy, while CMEs eject significant amounts of energetic plasma, which accelerates charged particles (mostly protons and alpha particles) into interplanetary space. The frequency and intensity of these events are influenced by the 11-year solar cycle, which alternates between periods of solar maximum (lasting about 7 years) and solar minimum (lasting about 4 years) [27]. CMEs and solar flares are more common during solar maximum, particularly in the declining phase [28]. Figure 2.4 illustrates the current solar activity (cycle 24) and predictions for the following cycle based on sunspot numbers (also known as the Wolf number).

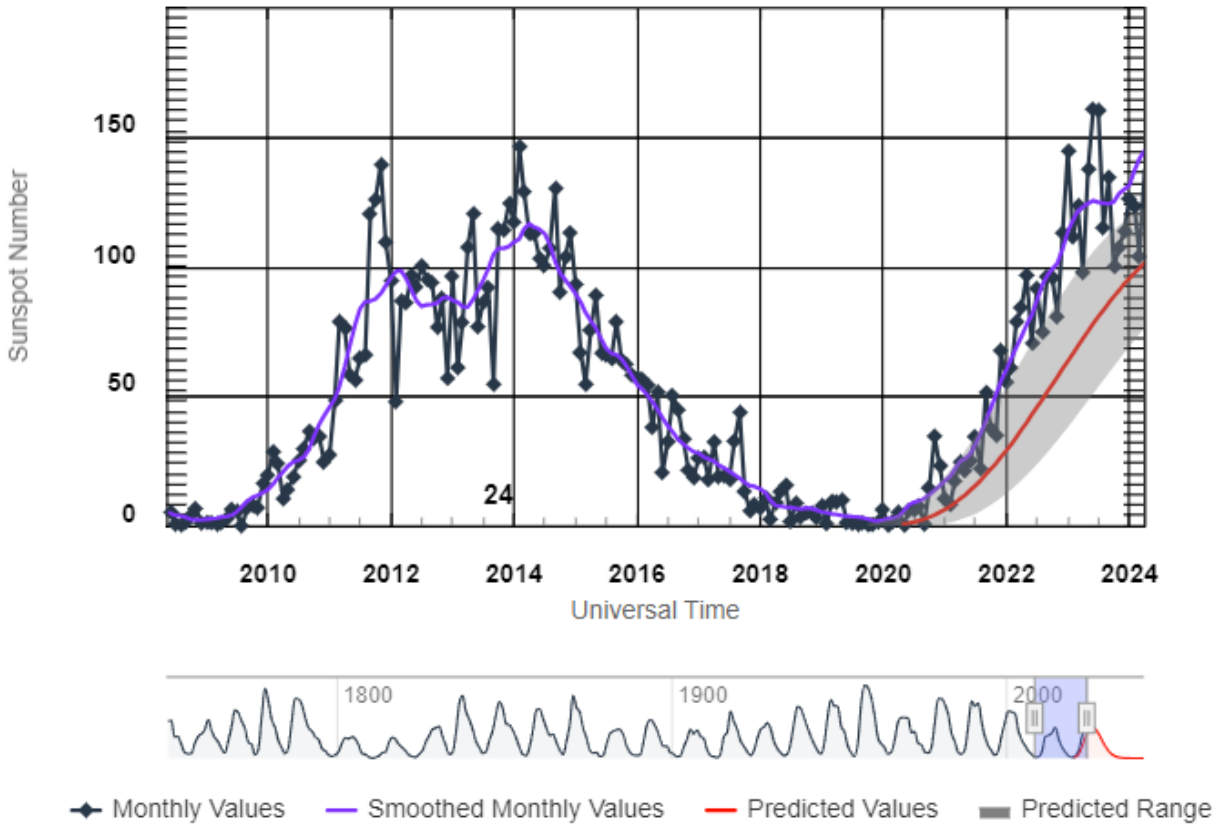

Figure 2.4: Solar Cycle Flux Progression [28].

Earth's magnetic field plays a crucial role in attenuating SCRs, providing partial protection against radiation hazards. However, during periods of heightened solar activity, SCRs still pose a substantial risk to electronics.

2.1.3 Belt trapped particles

The Earth's Radiation Belts, also known as the Van Allen radiation belts, were discovered in 1958 by James Van Allen. These belts are regions around Earth where the magnetic field traps charged particles (electrons and protons) originating from cosmic rays and solar wind. The Van Allen belts are one of the most hazardous areas for spacecraft due to the high levels of radiation that can damage electronic systems. The belts are divided into two main layers: the inner belt and the outer belt, each of which contains particles with distinct characteristics [22]. As can be seen in Figure 2.5, the outer belt is wider than the inner belt, and it is also the most unstable due to the weaker influence of the Earth's magnetosphere [21].

The inner belt lies between 1,000 km and 6,000 km above the Earth's surface and consists mostly of high-energy protons, along with some electrons. Proton energies in this region range from 0.1 to 500 MeV. The inner belt is relatively stable but is particularly hazardous in the South Atlantic Anomaly (SAA), where the belt dips closer to Earth's surface due to the weakened intensity of the magnetic field in this region [22]. This anomaly is illustrated in Figure 2.6 in which the high proton flux is identified at

altitudes as low as 500 km and below. The proton fluxes can reach 10^3 $protons/(cm^2 s)$ at energies over 10 MeV [29]. This intense radiation environment can cause degradation to low Earth orbit (LEO) spacecraft, such as the International Space Station (ISS) and small satellites.

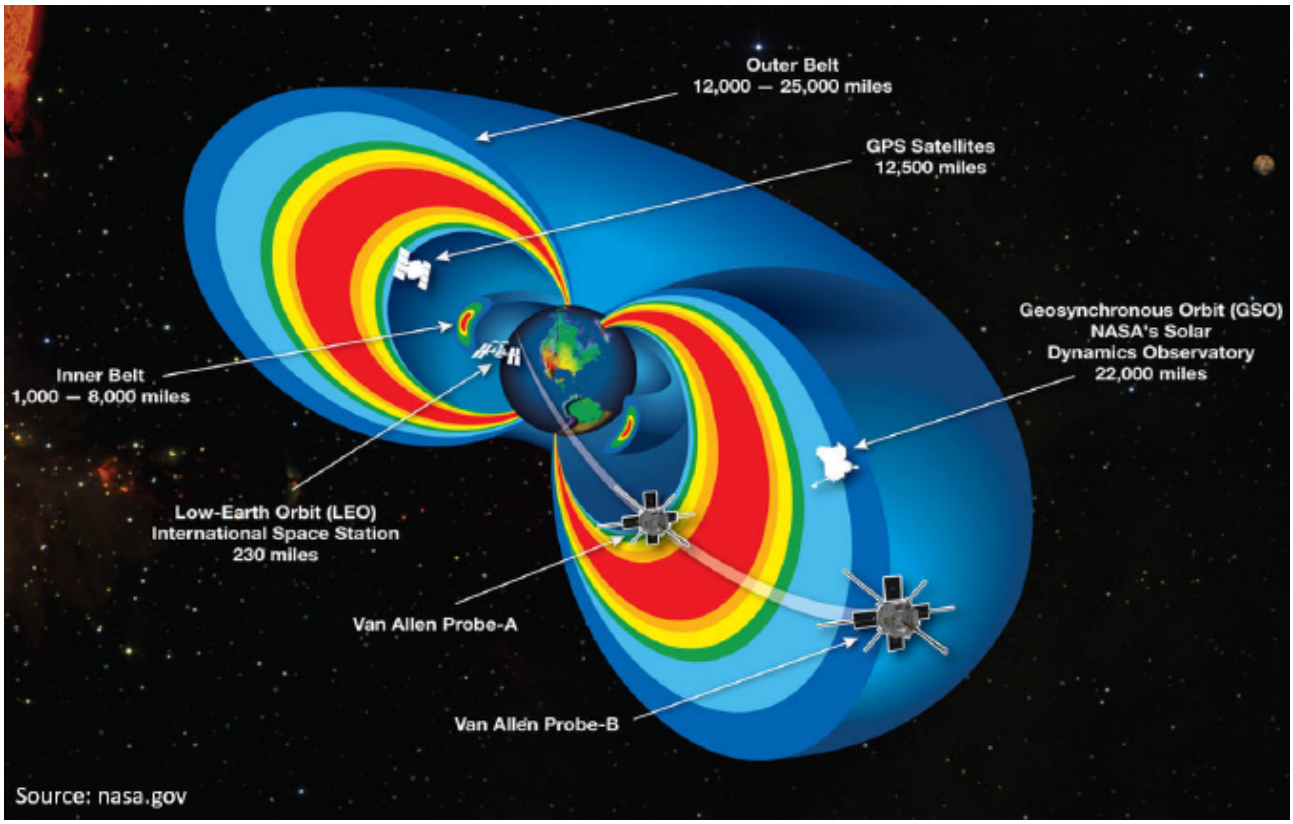

Figure 2.5: Van Allen's Radiation Belts [21].

The outer belt, located between 13,000 km and 60,000 km from Earth, is predominantly composed of electrons with energies ranging from 40 keV to 5 MeV. Because the energy of most trapped electrons in this region is relatively low, their impact is mainly on spacecraft components that are outside or only minimally shielded. Spacecraft with heavy protective layers typically experience negligible effects from the radiation present in the outer belt. The strongest electron flux in the outer belt occurs at altitudes well above those of LEO spacecraft, meaning these satellites are generally not exposed to the radiation hazards associated with the outer belt. In general, the omnidirectional integrated electron fluxes can reach 10^6 $protons/(cm^2 s)$ at energies above 1 MeV [22].

2.1.4 Atmospheric radiation

Cosmic rays and solar particles continuously bombard Earth's atmosphere, colliding with atmospheric atoms and molecules, primarily nitrogen and oxygen. These collisions initiate a cascade of reactions, known as air showers, which produce a diverse array of secondary particles, including protons, electrons, neutrons, muons, and pions [30]. Figure 2.7 illustrates this structure of this air shower.

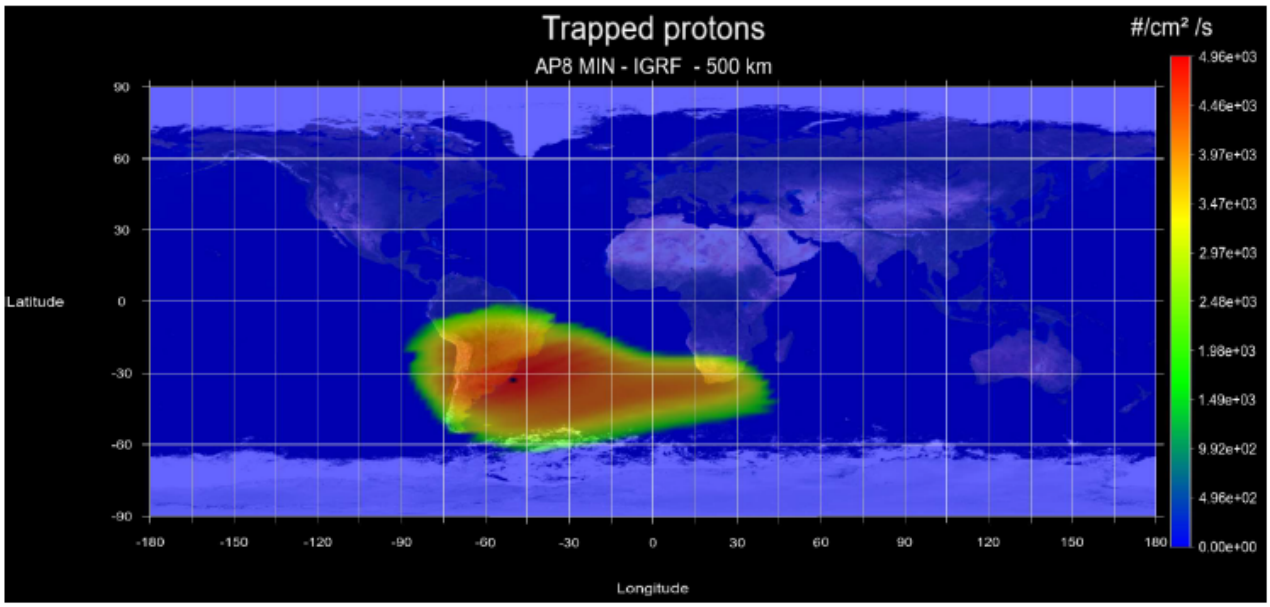

Figure 2.6: Flux intensity map showing the distribution of protons with energies above 10 MeV at an altitude of 500 km. The higher proton flux are concentrated in the South Atlantic Anomaly (SAA) region [29].

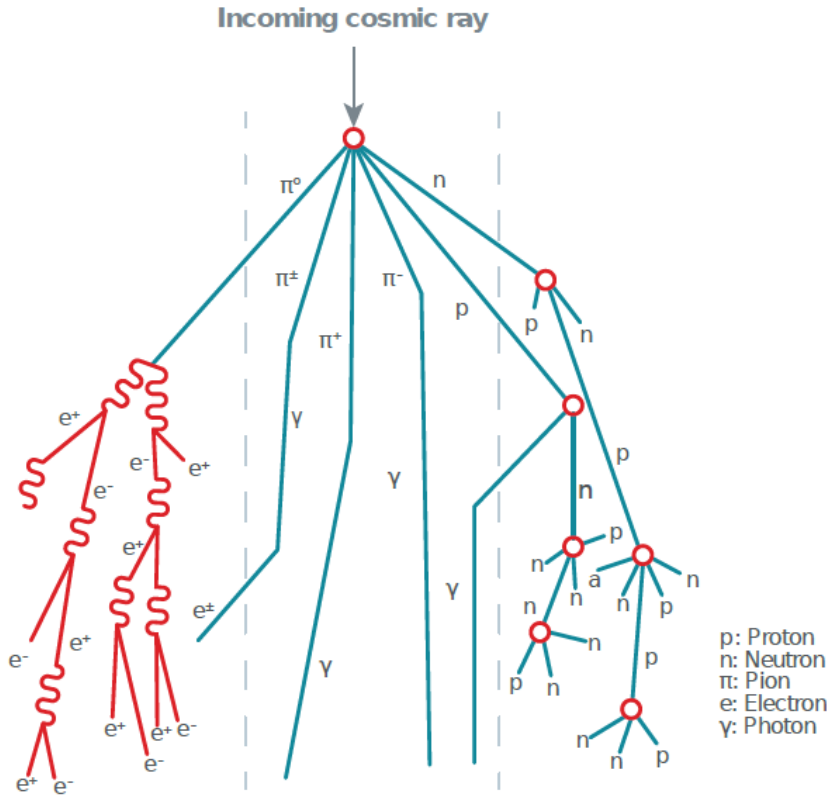

Figure 2.7: Cascade of secondary particles generated by the interaction of cosmic rays with atmosphere [31].

When GCR strikes an atmospheric molecule, it releases a burst of secondary particles that scatter outward, progressively interacting with more atmospheric atoms as

they descend. This phenomenon spreads over a wide area, generating multiple particle types that can penetrate deep into the atmosphere and, in some cases, reach Earth's surface. The distribution and intensity of these secondary particles depend on the energy of the initial cosmic ray and the altitude of the interaction. Generally, lower-energy particles are absorbed higher up in the atmosphere, while higher-energy particles penetrate deeper. Neutrons are the most significant contributors to the radiation effects observed in the atmospheric environment. This occurs due to their abundance and deep-penetrating ability, which allows them to travel significant distances without being deflected. Gamma rays are also abundant, but they are less concerning for electronics in comparison with neutrons due their lower energy transfer efficiency (can be effectively mitigated with shielding). In the other hand, with advancements in technology scaling, muons have also shown an increased capability to induce radiation damage in microelectronics, making them an emerging threat to system reliability [3, 32, 33]. These secondary particles create a complex radiation environment within the atmosphere. Figure 2.8 shows the integrated flux of these particles as a function of altitude.

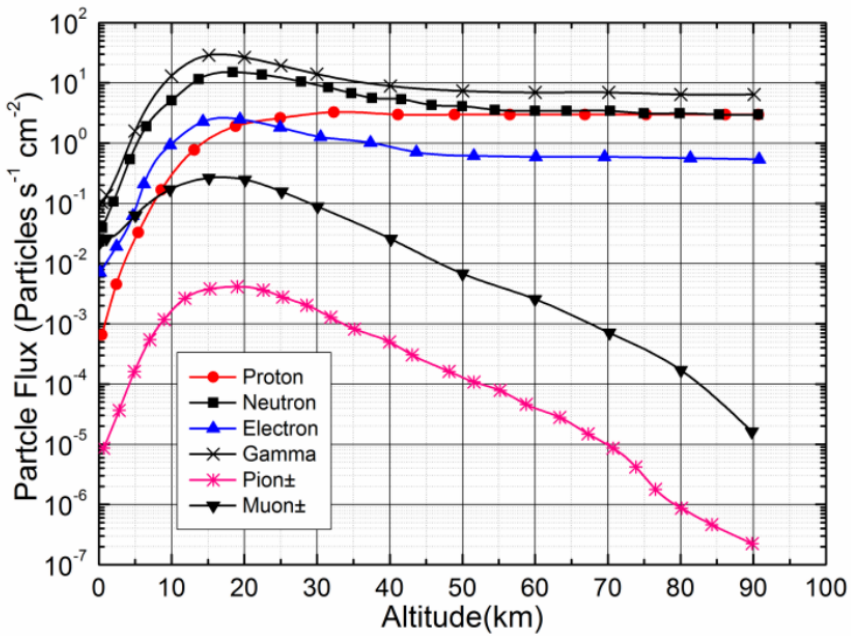

Figure 2.8: Atmospheric particle flux as a function of altitude [34].

The neutron flux increases with altitude until reaching a peak at approximately 20 km [35]. The energy spectrum of neutron radiation field is very wide. Usually the neutrons above 1 MeV are remarkable to contribute the SEE. There are two standard neutron energy spectra for SEE investigations in terrestrial and avionic environments. The Joint Electron Device Engineering Council (JEDEC) [36], which provides a reference neutron energy spectrum for terrestrial environments, and International Electrotechnical Commission (IEC), which address the impact of atmospheric radiation on avionics systems [37]. The total neutron flux of reference spectrum above 10 MeV is $3.6 \times 10^{-3} neutrons/(cm^2 s)$ at sea level in New York City.

2.1.5 Experimental radiation

Experimental radiation environments are artificially generated using specialized devices and equipment in controlled laboratory settings to evaluate the effects of radiation on various materials and systems. These radiation sources typically create a mono-type radiation environment, where conditions can be precisely controlled and repeated over short periods. Such setups are invaluable for understanding radiation effects, studying underlying mechanisms, and advancing experimental techniques and data analysis.

The most commonly used experimental radiation sources include cobalt-60 (^{60}Co) gamma-ray generators, X-ray sources, neutron sources, and linear and circular accelerators. These sources have widespread applications across multiple industries and research fields, including food sterilization, radiotherapy, health physics, materials science, chemistry, nuclear physics, and aerospace equipment testing.

Gamma rays from Co-60 are highly energetic, with photon energies of 1.17 MeV and 1.33 MeV, providing significant penetration power essential for assessing radiation effects on electronic devices. ^{60}Co sources are often used as a standard for total ionizing dose testing, following European Space Components Coordination (ESCC) standards [38]. However, X-ray sources have emerged as an alternative due to their higher dose rates and operational convenience. High-energy X-ray generators, typically exceeding 100 kV, produce photons through electron acceleration and target collisions, offering several advantages: they allow precise collimation for irradiating specific parts, provide faster testing due to higher dose rates, and are more cost-effective and safer to manage compared to radioactive sources. Additionally, X-ray generators enable testing of packaged devices due to their high penetration depths, making them increasingly suitable for modern semiconductor testing needs [39].

Linear accelerators and cyclotrons are used to produce pulsed, high-energy ion beams. These beams can be injected directly into test samples or into high-Z targets for particle irradiation. Both types of accelerators use electric and magnetic fields to accelerate charged particles via Coulomb and Lorentz forces. In a cyclotron, a magnetic field curves the particle's path, allowing for a compact design that saves space while still achieving high acceleration. Cyclotrons can be tuned to select and screen for different ions by adjusting the electric and magnetic fields. Figure 2.9 shows the basic structure of a linear and a cyclotron accelerators.

Cyclotrons, though effective, are limited by the size and cost of the magnetic fields they require, typically capping particle energies at a few hundred MeV. A cyclotron operates with a constant magnetic field strength and a constant frequency. The beam energy is inherently limited by relativistic effects, which disrupt synchronization between the particle orbits and the frequency. As a result, cyclotrons are primarily effective for ion acceleration. One significant advantage of cyclotrons is their ability to generate a continuous train of beam micro-pulses. Cyclotrons are characterized by their large-area magnetic fields, which confine ions from their initial low energy to the output energy. However, to achieve significantly higher energies, synchrotrons are used.

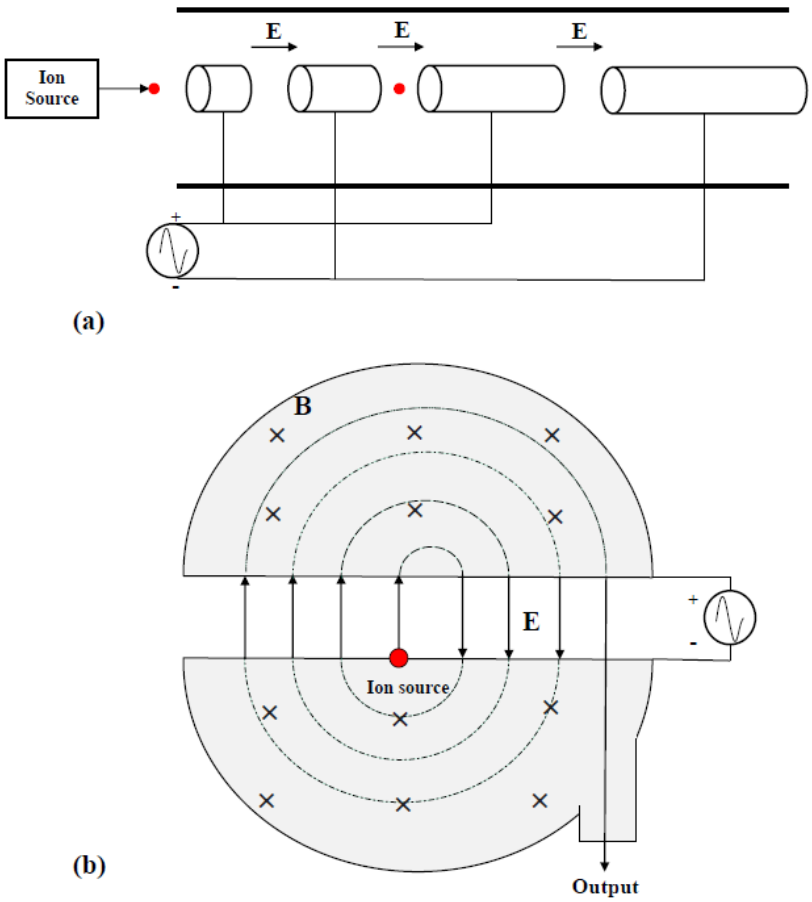

Figure 2.9: Different accelerator setups: (a) Linear structure and (b) cyclotron structure [40].

Synchrotrons are the current standard for particle physics research accelerators. These are cyclic accelerator that incrementally boosts the energy of charged particles with each pass, using precisely tuned electric and magnetic fields. This continuous acceleration pushes particles to relativistic energy levels, making synchrotrons indispensable for high-energy physics research. The most famous example of a synchrotron is the Large Hadron Collider (LHC), operated by CERN. The LHC is a 27 km-long accelerator situated about 100 meters underground. It generates two beams of protons, each with an energy of 7 TeV, which circulate in opposite directions. These beams are then brought to collision points inside large-scale detectors, such as ATLAS and CMS. These detectors, which played a pivotal role in the discovery of the Higgs boson, are designed to capture and analyze the particles produced during collisions [41].

Achieving these extreme energy levels requires several stages of acceleration. The LHC relies on a series of smaller accelerators to progressively increase the energy of particles before injecting them into the main collider. This process begins with a linear accelerator, which initially accelerates particles to relatively low energies. These particles are then transferred sequentially to increasingly larger circular accelerators, such as the Proton Synchrotron (PS) and the Super Proton Synchrotron (SPS), which boost their energy at each stage. This hierarchical system ensures efficient acceleration while maintaining control over the particle beams, preparing them for their final high-energy

collisions in the LHC's massive ring. The current CERN accelerator complex consists of a chain of five accelerators, each providing a successive energy boost before the particles enter the LHC. A graphical representation of the accelerator complex and the main facilities at CERN is shown in Figure 2.10.

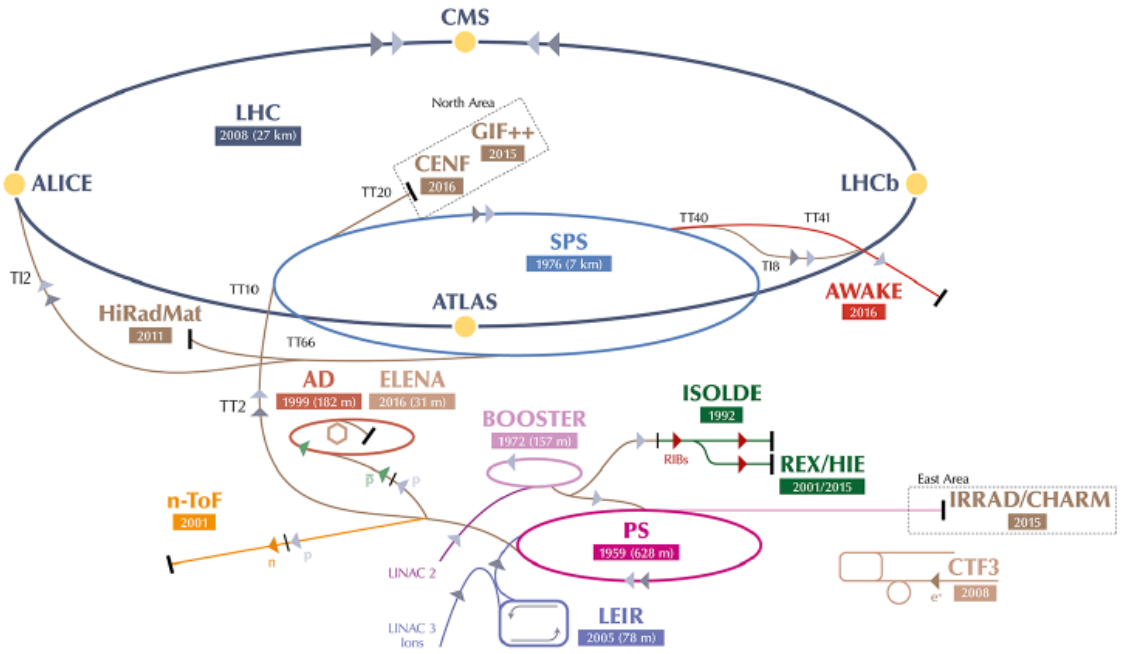

Figure 2.10: CERN accelerator complex: The LHC is the final stage of a chain composed of five accelerators[42].

2.2 Radiation Effects in Electronics

This section provides an introduction to particle interaction physics related to the radiation effects observed in electronic components. Radiation phenomena can cause transient, permanent, or destructive effects in integrated circuits. These radiation effects can be grouped into two main categories: Cumulative Effects and Single Event Effects (SEEs). This thesis focuses specifically on the study of SEEs, particularly the non-destructive effects known as soft errors. Accordingly, the following sections are directed towards understanding these effects.

2.2.1 Energy Deposition

Particle interactions with matter, particularly in the context of Single Event Effects (SEEs), can be broadly divided into two types: (1) interactions induced by charged particles, such as protons and heavy ions, and (2) interactions induced by uncharged particles, such as neutrons.

When charged particles, travel through a material, they lose energy through interactions with the material's electrons and nuclei. This energy loss primarily occurs due to inelastic collisions with atomic electrons, a process known as ionization, where sufficient energy is transferred to eject electrons from the valence band to the conduction band, generating electron-hole pairs. This ionization process is key to the damage caused by radiation in semiconductors and electronic components. The inelastic collisions with atomic electrons are the dominant mechanism of energy loss for charged particles, given their higher probability compared to interactions with atomic nuclei [43].

The energy lost by a particle per unit length as it travels through a material is called stopping power. Stopping power is a quantity that characterizes how a particle loses energy in a medium and is composed of two main components:

- **Electronic stopping power**: the energy lost by the particle due to collisions with atomic electrons of the target material.
- **Nuclear stopping power**: the energy lost by the particle due to collisions with atomic nuclei of the target material.

The electronic stopping power is also known as the Linear Energy Transfer (LET). LET represents the energy deposited by an ionizing particle along its track as it passes through the device. This energy deposition per unit length corresponds to the creation of electron-hole pairs within the device and can be estimated from numerical simulations using software such as the popular Stopping and Range of Ions in Matter (SRIM) tool [44]. The LET can be expressed by the following equation 2.1:

$$LET = -\frac{\Delta E}{\Delta x} \tag{2.1}$$

where ΔE represents the energy loss and Δx is the ionizing path length. It is expressed in $MeV/\mu m$.

In radiation effects studies on electronic components, the charge generated by the ionization mechanism as a particle traverses a device is typically expressed in units of picocoulombs per micrometer. This unit provides a direct measure of the charge deposition within the material. Additionally, a mass LET is often utilized, defined as the ratio of LET to the density (ρ) of the target material. The mass LET provides a more precise characterization of the energy deposition process relative to the material's structure and composition, as shows Equation 2.2

$$LET = -\frac{1}{\rho}\frac{\Delta E}{\Delta x} \tag{2.2}$$

where ρ is the density of the target material. The unit for mass LET is $MeV.cm^2/mg$.

The LET depends on several factors, including the type of particle, its energy, and the target material. For electronic devices, silicon is the primary material, with a density of $\rho_{Si} = 2.32\ g/cm^3$. Figure 2.11 illustrates how LET varies with ion energy

in silicon. As the particle energy increases, LET initially rises, reaching its maximum at the Bragg peak, before decreasing as energy continues to increase beyond this point. Notably, different ion species with varying energy levels can exhibit the same LET value, highlighting the complex relationship between particle properties and energy deposition [43].

When a charged particle deposits energy in a semiconductor, it generates a nearly linear path of electron-hole pairs (E_{hp}). The minimum energy required to create an electron-hole pair in a material can be estimated using the material's band-gap energy (E_g). The relationship is described by the following equation 2.3:

$$E_{ehp} = 2.73E_g + 0.55eV \tag{2.3}$$

For silicon-based devices, where the band-gap energy E_g is 1.11 eV, the ionization energy E_{ehp} is approximately 3.6 eV/ehp. Materials with a higher band-gap energy require more energy to ionize, which is why wide-bandgap semiconductors, such as SiC (silicon carbide) and GaN (gallium nitride), demonstrate superior radiation resistance. Their higher band-gap energies make it more difficult for radiation to generate electron-hole pairs, enhancing their performance in radiation-heavy environments. Figure 2.12 illustrates the direct and indirect ionization of a heavy ion and a neutron, respectively.

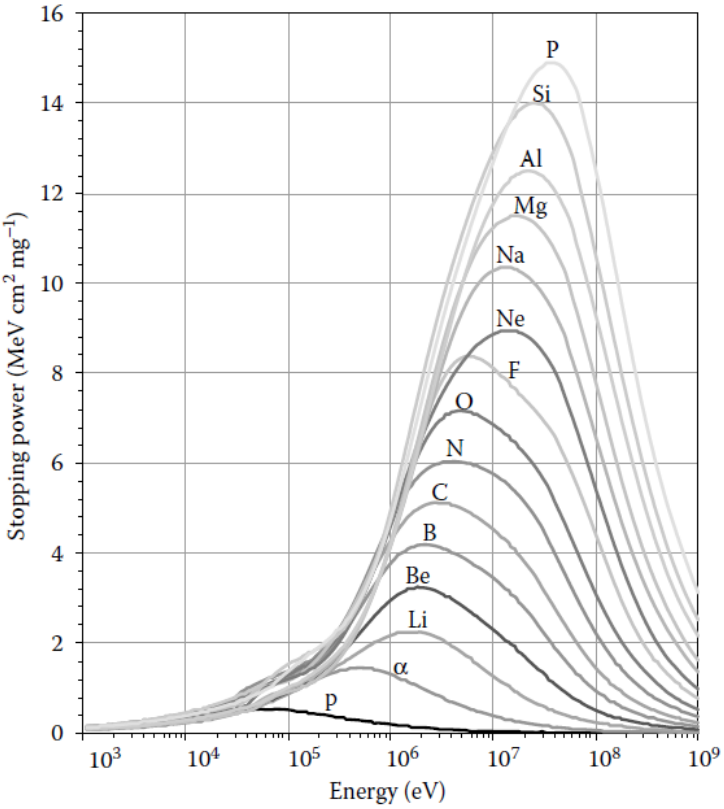

Figure 2.11: Variation of LET as a function of energy for several ions that may result from neutron interactions with silicon [44]. The proton (p) and alpha (α) labels are associated to Hydrogen (H) and Helium (He) ions, respectively.

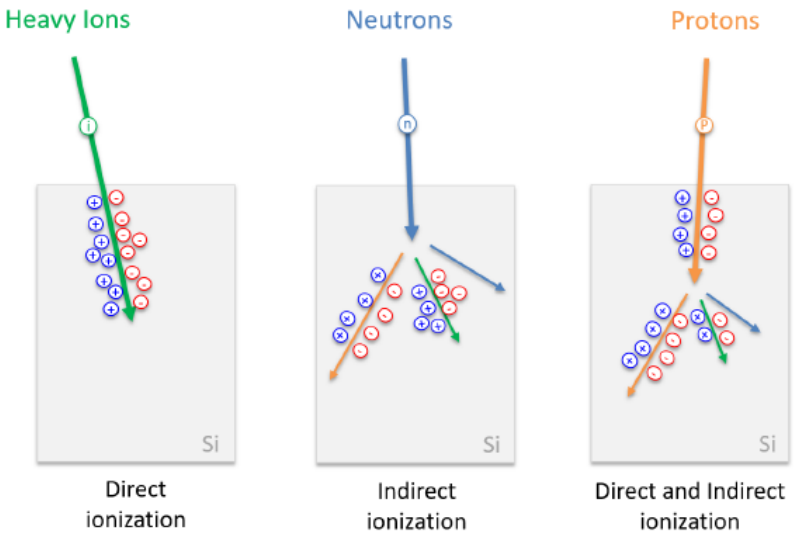

Figure 2.12: Representation of Direct Ionization and Indirect Ionization for heavy ions, neutrons and protons interaction with matter [45].

2.2.2 Charge collection

When a particle strikes a semiconductor device, it deposits energy that releases charge carriers (electrons and holes). These carriers are subsequently transported and collected by the junctions within the device. In the context of SEEs, there are two primary mechanisms that control carrier transport: drift and diffusion. Figure 2.13 depicts these mechanisms.

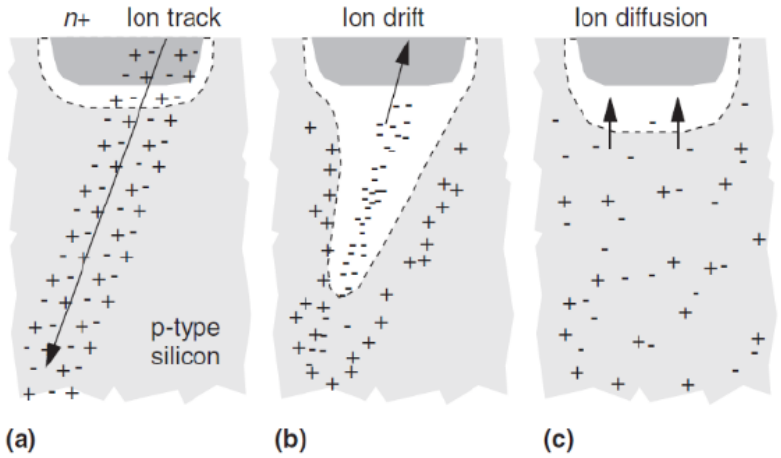

Figure 2.13: Charge collection mechanisms due to an ion strike in a p-n junction: (a) ion track, (b) drift process, and (c) diffusion process. [1].

The drift mechanism is controlled by the electric field present in the p-n junction of sensitive semiconductor devices. When a high-energy particle impacts the sensitive region of the circuit, the produced charge carriers are rapidly collected by the influence of the strong electric field, which is typically present in reverse-biased p-n junctions. This electric field accelerates these carriers, moving them quickly towards the collection electrodes. Drift plays an essential role in sensitive circuits since the rapid collection

of charge can trigger Single Event Upsets (SEUs) or other radiation-induced effects. The presence of a strong electric field makes the drift process extremely fast, ensuring efficient charge collection.

In contrast, diffusion is a transport mechanism driven by carrier concentration gradients. Here, carriers move from regions of high concentration to regions of lower concentration, gradually dispersing over time. Diffusion usually occurs when a particle strike happens in regions beyond the direct influence of the electric field. Compared to drift, diffusion is a slower process and governs the transport of carriers that are farther from the p-n junction's high-field region.

If a particle strikes in or near the p-n junction, the funneling effect can enhance the charge collection process. This effect occurs when the electric field expands deeper into the substrate due to the ion strike, temporarily increasing the size of the depletion region. This expanded depletion region improves the efficiency of charge collection, allowing more carriers to be rapidly swept into the junction. The combination of drift and funneling ensures quick collection of carriers, increasing the likelihood of SEE events in sensitive areas of the device.

The entire charge collection process typically begins with drift and funneling, driven by the electric field and occurring very quickly. Once these fast processes are complete, any remaining carriers that are not immediately collected are transported via diffusion or recombine with other carriers in the material.

The minimum amount of collected charge required to trigger an SEE in a device is known as the critical charge (Q_{crit}). If the charge generated by a particle strike exceeds Q_{crit}, it can lead to an upset or failure in the device's operation. Understanding and find ways to maximize the Q_{crit} is crucial for designing radiation-hardened electronics, especially for environments like space or nuclear facilities, where SEEs are more likely.

2.3 SEE modeling and prediction

The study of Single-Event Effects (SEEs) relies heavily on the use of radiation testing. However, experimental activities are very complex, time-consuming, and costly [46, 47, 48, 49]. Therefore, the modeling and prediction tools offers a complementary alternative to predictive the behavior before the test or understand post-irradiation data. Such modeling tools are designed to accurately simulate the interactions of radiation-induced particles with electronic components. This modeling tools are indispensable, enabling the evaluation of mitigation strategies and aiding engineers in developing more robust systems. In this context, this section explores the main SEE modeling and simulation, encompassing circuit-level, device-level, and alternative modeling techniques.

2.3.1 Circuit level simulation

Circuit-level modeling focuses on the electrical behavior of fundamental electronic components, such as transistors, resistors, capacitors, and diodes. The Simulation Program with Integrated Circuit Emphasis (SPICE) is a widely used tool that solve a set of equations to provide a robust platform for assessing how circuits will behave under various conditions. These equations are based on different types of models developed by the semiconductor industry and the academia. A famous MOSFET model is the Barkely Short-channel IGFET model (BSIM) [50]. However, accurately predicting radiation effects requires careful consideration of material composition and particle-matter interactions, and involves challenges related to simulation methodology and experimental validation [51, 52, 53]. The number of parameters associated with a SPICE model can vary widely based on the complexity and specificity of the component being modeled. A simple transistor can require hundreds of parameters. This complexity increases when we consider a complete circuit. Another complicating factor is the phenomenon of charge sharing, where charges generated by a single particle strike may concurrently affect multiple circuit nodes. This interdependent behavior makes circuit-level radiation modeling particularly challenging.

Traditionally, circuit-level SEE models use a double-exponential current to represent the transient current spike caused by a radiation event. This current source can be injected in a SPICE simulator as an current source, and is typically modeled as:

$$I_{SEE}(t) = \frac{Q_c}{\tau_r - \tau_f}\left(e^{-t/\tau_f} - e^{-t/\tau_r}\right), \tag{2.4}$$

where Q_c represents the total charge, while τ_r and τ_f represent the rise and fall times, respectively. These parameters are tuned to match experimental data, providing a current waveform that mimics the effect of a particle strike.

Besides being technology dependent, these variables are also influenced by the relative distance of the particle hit. However, several estimation approaches have been proposed based on usually known technology parameters [54, 55, 5, 56]. Once these parameters are defined, the radiation-induced current can be injected in the sensitive nodes of the circuit in a transient analysis using SPICE. Figure 2.14 shows the schematic of an inverter considering the injection of the current source for each type of particle. If the particle strikes the N-channel of the device, the current is introduced between the drain and the ground supply. Conversely, if the particle strikes the P-channel, the current is connected between the drain and the power supply.

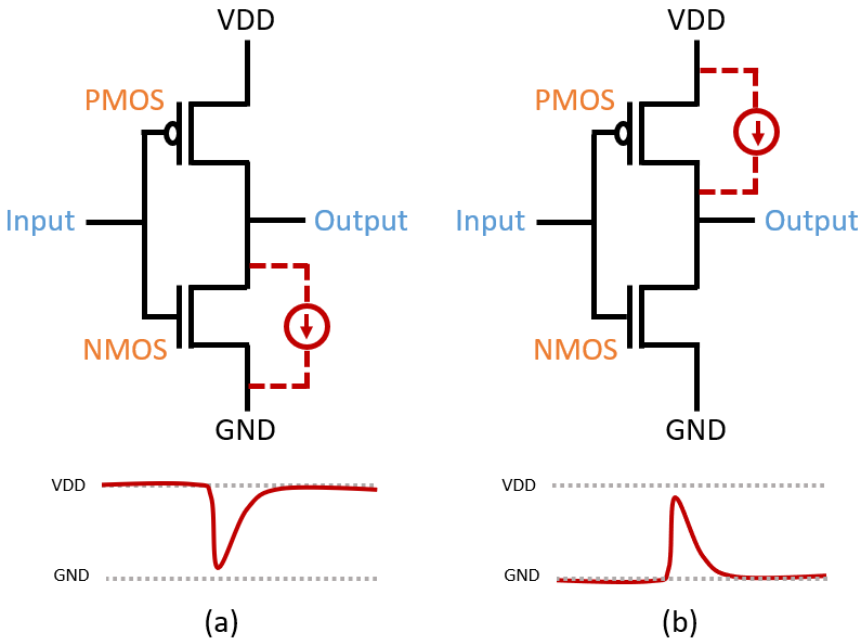

Figure 2.14: Double-exponential current injection: (a) NMOS and (b) PMOS strikes.

2.3.2 Device level simulation

In contrast to circuit-level SEE simulation, which primarily investigates the response of a radiation-induced current spike to a given circuit, device-level simulation focuses on the underlying physical processes governing radiation interactions with the semiconductor material. This includes the interaction of particles with device materials, the generation of carriers, and their subsequent transport within the semiconductor. Such detailed device-level modeling provides a more precise understanding of the response of individual devices.

Device-level simulations generally employ two complementary approaches: Monte Carlo simulations to model particle interactions, and TCAD simulations to understand device physics and electrical responses.

- **Monte-Carlo approach**

  Monte Carlo simulations are one of the most precise methods for studying the interactions between radiation and different materials. The Monte Carlo approach involves simulating individual particles and tracking their interactions with a material, considering phenomena such as electromagnetic interactions, nuclear collisions, and secondary particle creation. This is typically achieved by utilizing theoretical models of nuclear interactions.

  Monte Carlo methods also account for material inhomogeneities by utilizing detailed material properties, such as atomic composition, electron density, mass density, and ionization potential. Software packages such as FLUKA [57] and Geant4 [58] are widely used to simulate particle interactions. However, while Monte Carlo

simulations provide high accuracy for modeling physical interactions and predicting where charge deposition will occur, they generally lack the ability to simulate the electrical behavior of semiconductor devices following a particle strike.

- **TCAD Simulation**

  Technology Computer-Aided Design (TCAD) refers to the use of computer simulations to develop and optimize semiconductor processes and devices. TCAD simulation tools allow for detailed simulations at the semiconductor device level, providing insight into charge generation, recombination, and transport mechanisms. This method is highly advantageous for understanding the specific ways in which radiation-induced charges move through a semiconductor device and how these charges eventually affect the circuit-level behavior.

  TCAD tools, such as Synopsys Sentaurus, SILVACO Athena and Delphea ECORCE, are often used to establish a detailed simulation model of the semiconductor device. This simulation model involves both process modeling and structural modeling, which means the device is simulated from the beginning of fabrication to the final device structure. Through electrical parameter calibration and extensive characterization, these tools offer precise modeling capabilities for SEE analysis.

  TCAD simulations are best suited for simple device structures or small-scale circuit elements, as the computational complexity increases substantially for larger and more complex circuits. Nevertheless, these simulations are indispensable in characterizing radiation-induced single-event transients (SETs), single-event upsets (SEUs) and total ionizing dose (TID), as they provide a level of detail and precision beyond that of circuit-level SPICE models.

2.3.3 Alternative modeling approaches

Most of these simulation methods rely on the information provided in the Process Design Kit (PDK). The PDK encompasses a comprehensive set of files, libraries, and models that describe the process parameters, electrical characteristics, and layout rules for a specific manufacturing process. These parameters form the foundation for simulating electronic circuit behavior, enabling engineers and researchers to predict performance under various conditions with a high degree of accuracy.

However, obtaining these realistic parameters can be challenging, as they are typically confidential and not openly available from manufacturers [59]. As a result, when such parameters are inaccessible, the accuracy of simulation results may be compromised. Additionally, even when models are available, certain types of analysis can be computationally demanding, requiring significant CPU resources and time.

Given the importance of SEE modeling and the obstacles associated with traditional methods, it is crucial to explore alternative modeling approaches that can overcome these limitations. Therefore, this PhD thesis will investigate and develop different SEE

modeling techniques, aiming to provide alternatives and accessible solutions for assessing the radiation sensitivity of electronic devices.

2.4 Conclusion

This chapter establishes a comprehensive foundation for understanding radiation effects in electronic components, with a particular emphasis on the mechanisms underlying Single Event Effects (SEEs). These mechanisms are crucial for modeling and simulating radiation effects at both the circuit and device levels. Modeling and prediction tools play a vital role in complementing irradiation tests. However, the challenges and limitations of traditional simulation methods, especially those dependent on Process Design Kits (PDKs), highlight the necessity of exploring alternative modeling strategies. The subsequent chapters will explore innovative simplified approaches to SEE modeling, aiming to overcome these limitations.

Chapter 3

Impact of low-energy Neutrons on SER

In both aviation and ground-level applications, neutrons present a significant challenge by triggering single event effects (SEEs). The rate of non-destructive SEEs, known as the soft error rate (SER), is influenced by the flux of incident particles and the susceptibility of the target device, which may be characterized by a sensitive volume and a threshold for critical charge or energy [60, 61, 62].

Accurate assessment of the SER is essential to evaluate the robustness of electronic systems across various environments. Tools that estimate the SER, such as those described in [60, 61, 62, 63, 64], play a key role in this process. These tools not only support the planning and analysis of irradiation tests but also aid in the design and development of hardening techniques to improve device reliability. Many of these tools utilize the Monte Carlo method, which effectively captures the diverse interactions that can occur when a neutron interacts with an electronic device. Despite their effectiveness, these methods often demand extensive knowledge of device specifics (which may be confidential) and require considerable computation time.

This analysis aims to develop a simplified analytical method for calculating the SER, minimizing the number of input parameters needed. The analytical burst generation rate (BGR) model, initially introduced by Ziegler and Landford [60] and later refined by Letaw and Normand [61] and Tosaka [62], is based on energy deposition within a sensitive volume. Although effective for larger-scale devices, this model assumes that only secondary ions generated within the sensitive volume contribute to soft errors, leading to a simplification where the SER is directly proportional to the sensitive volume. However, this assumption is no longer accurate for modern technologies, as particles generated outside the sensitive volume can also induce errors. In this analytical approach, the first step is to separate the geometric factors (related to the sensitive volume) from the nuclear physics aspects, treating them independently to increase the flexibility of the calculation.

As electronic technologies scale-down, the minimum neutron energy capable of causing an SEE also decreases, allowing low-energy neutrons, abundant in the atmosphere, to play a more prominent role [36, 37, 65]. This chapter proposes an analytical method to evaluate the contribution of neutrons in the 1–10 MeV energy range to the SER across different technologies, exploring the trends associated with technological miniaturization.

3.1 Neutrons in Earth's atmosphere

Neutrons in the atmosphere are a major cause of SEE occurrences in electronic devices. These neutrons can produce secondary ions that may lead to unexpected currents and potential device failures. The likelihood of an SEE is dependent on the neutron's energy, which makes understanding the neutron spectrum in the atmosphere crucial. The JEDEC [36] and IEC [37] standards provide neutron spectra at ground level and avionic altitudes, respectively (Figure 3.1). The spectra have a similar shape, but neutron flux at avionic altitude is about 300 times higher compared to ground level.

The flux increases as neutron energy decreases, making low-energy neutrons particularly important to consider. Historically, only neutrons above 10 MeV were considered significant for causing failures, but advances in technology have made devices more susceptible to lower-energy particles. As the threshold energy to cause errors decreases, the contribution from the 1–10 MeV energy range may become significant.

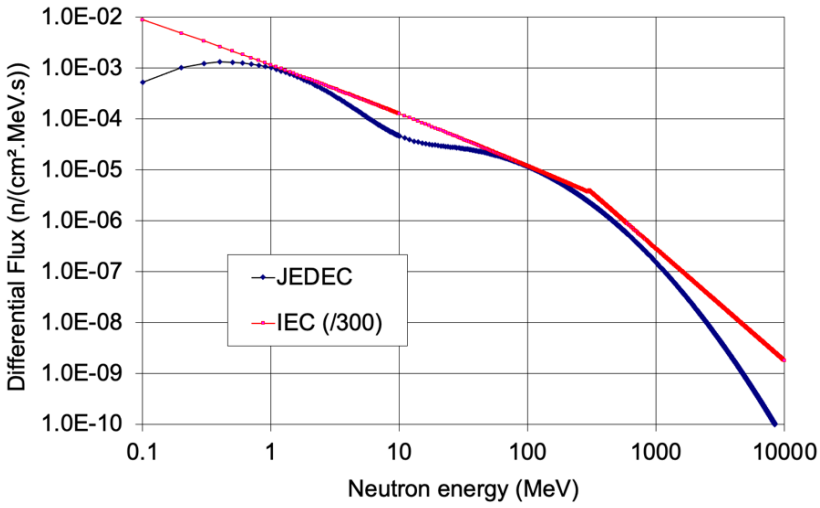

Figure 3.1: Neutron differential flux given by two standards JEDEC [36] (for ground level application) and IEC [37] for avionic applications. For the sake of comparison, IEC flux has been divided per 300.

To investigate the impact of the 1-10 MeV neutron energy range, it is useful to obtain a formula describing the neutron spectrum at ground level. Figure 3.2 plot the flux given by IEC (divided by a factor of 300) and the fitting of the curve with a power law in the 1-10 MeV energy range. In this sense, it is possible describe the differential neutron flux using Equation 3.1:

$$\frac{d\varphi}{dE} = \frac{1.14 \times 10^{-3}}{E^{0.941}} \tag{3.1}$$

where E is expressed in MeV and the differential flux in $/cm^2/MeV/s$.

More generally, the power law fit can be performed on the whole spectra as shown in Figure 3.3. To accurately fit the differential flux, we propose an approximation using Equations 3.2 and 3.3:

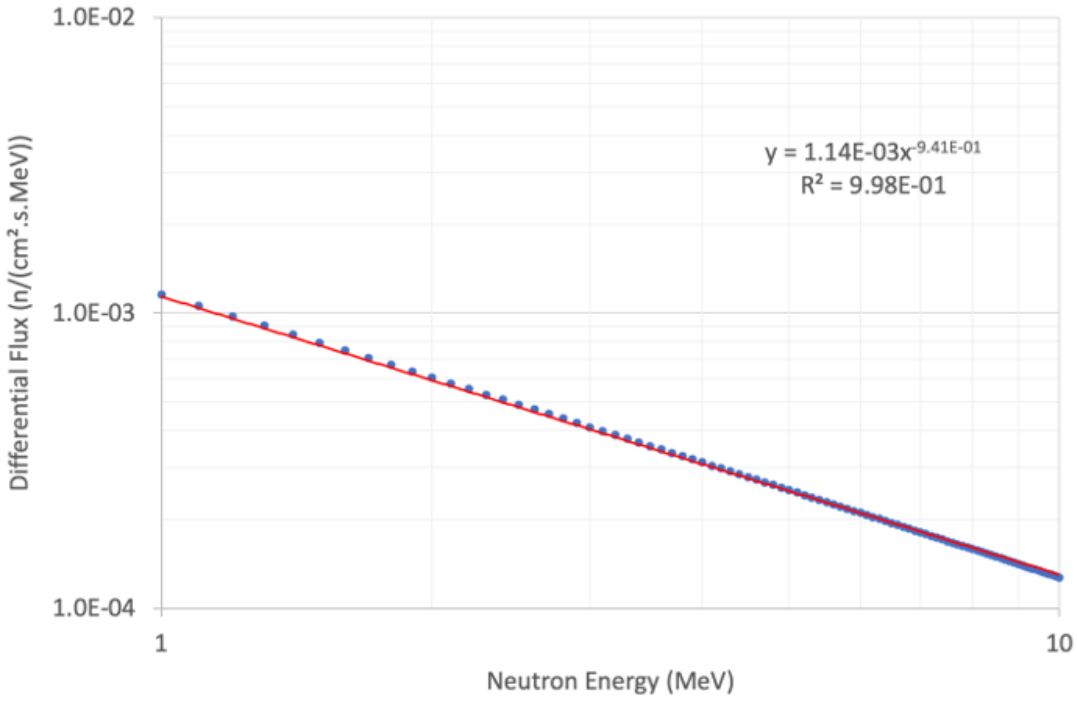

Figure 3.2: IEC spectra divided by 300 in the 1-10 MeV energy range. The red line is a fit of the spectrum with a power law.

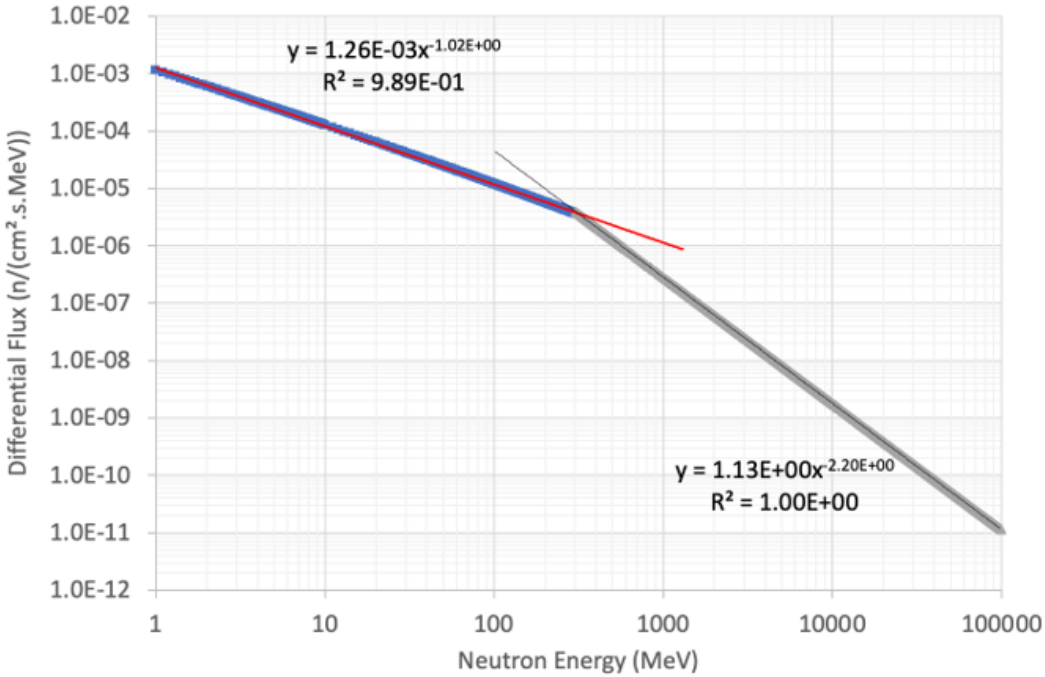

Figure 3.3: IEC spectra divided by 300 in the 1-100 GeV energy range. The red and the black lines are a fit with a power law respectively below and above 300 MeV.

$$\frac{d\varphi}{dE} = \frac{1.26 \times 10^{-3}}{E^{1.02}} \quad for \quad E < 300MeV \tag{3.2}$$

$$\frac{d\varphi}{dE} = \frac{1.13}{E^{2.20}} \quad for \quad E > 300MeV \tag{3.3}$$

3.2 Methodology to Evaluate the Soft Error Rate (SER)

The SER depends on the sensitivity of the device and the flux of particles that can trigger SEEs. Therefore, to estimate the SER we need to know the following:

- The SEE cross-section, $\sigma_{SEE}(E)$, characterizing the device sensitivity, which is known to decrease when neutron energy decreases;
- The neutron energy spectrum, $\frac{d\varphi}{dE}$ (see Section 3.1), which characterizes the radiation environment. Notice that, because neutrons result from multiple collisions of particles in the atmosphere, their distribution can be considered approximately isotropic.

The SER can then be calculated by using the following Equation 3.4:

$$SER = \int_0^\infty \sigma_{SEU}(E) \frac{d\varphi}{dE} dE \tag{3.4}$$

3.2.1 Worst case scenario

The SEU cross-section ($\sigma_{SEU}(E)$) is a parameter that depends on the technology being analyzed. A worst-case analysis can provide an estimation of the SER in such scenario, offering valuable insights. Experimentally, the neutron cross-section begins to increase above 1 MeV and saturates at a few tens of MeV. In the worst-case scenario illustrated in Figure 3.4, it is assumed that the cross-section is zero below 1 MeV and remains constant at a saturation value (σ_{SAT}) above this energy threshold. Following the IEC standard flux [37] divided by 300 to estimate ground-level contributions, the SER is calculated across four neutron energy ranges of interest:

- **1 MeV to 10 MeV:** In this range, the cross-section decreases below 10 MeV as device scaling progresses.
- **10 MeV to 50 MeV:** The cross-section rises toward saturation in this region, although its behavior depends on the specific technology used.
- **50 MeV to 200 MeV:** The cross-section reaches its saturation value in this range.
- **Above 200 MeV:** The cross-section is expected to remain at saturation, but experimental data are unavailable due to the lack of monoenergetic neutron beams.

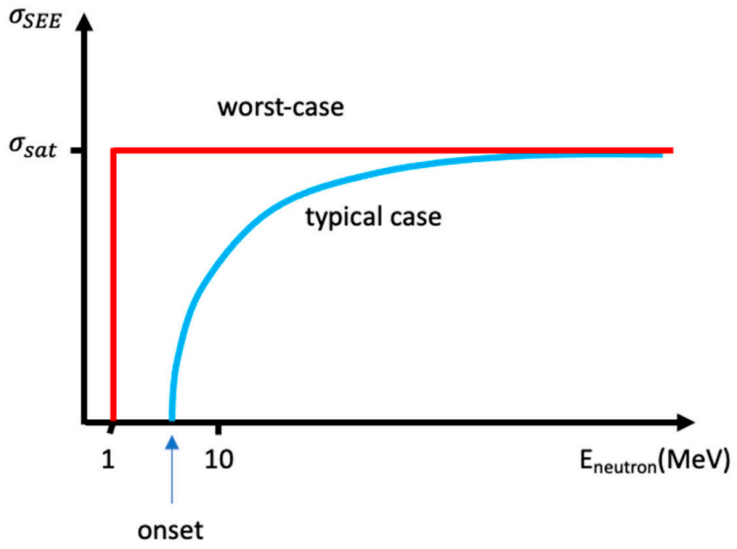

Figure 3.4: Illustration of cross-section versus neutron energy in a typical case (where the onset is between 1 and 10 MeV) and the worst-case scenario yielding the highest SER.

The contributions of these energy ranges to the SER were calculated using Equation 3.4, and the results are presented in Table 3.1. The worst-case analysis reveals that neutrons in the 1–10 MeV range contribute 44% of the total SER at ground level. While the differential flux increases significantly at lower energies (by over an order of magnitude from 10 MeV to 1 MeV), neutrons in this range are not the primary contributors to SER. Furthermore, since the SEE cross-section typically decreases below 10 MeV, this contribution could be much smaller.

Table 3.1: Contribution of four main energy ranges to the SER in the framework of the worst-case analysis, assuming constant SEE cross-sections for neutrons above 1 MeV. Calculations use the IEC standard flux divided by 300 to estimate ground-level contributions.

Energy range	**SER (FIT/Mcell)**	**Contribution to total SER**
1 MeV to 10 MeV	$8.37 \times 10^{15}(\sigma_{sat})$	44%
10 MeV to 50 MeV	$3.94 \times 10^{15}(\sigma_{sat})$	21%
50 MeV to 200 MeV	$2.51 \times 10^{15}(\sigma_{sat})$	13%
200 MeV to 100 GeV	$4.20 \times 10^{15}(\sigma_{sat})$	22%
Total	$19.02 \times 10^{15}(\sigma_{sat})$	100%

Thus, in the worst-case scenario, the 1–10 MeV range accounts for up to 44% of the total SER, making it a relevant contributor that warrants further investigation. To refine the understanding of low-energy neutron contributions, it is essential to incorporate technological parameters and more accurately model neutron interactions with matter.

3.3 Neutron interaction in 1-10 MeV energy range

Since the primary material used in electronic devices is silicon, with ^{28}Si being its dominant isotope, we focus on the nuclear reactions of neutrons with ^{28}Si. These interactions

can result in a variety of nuclear reactions, producing different secondary ions depending on how the silicon nucleus fragments during the collision. The range of possible reactions expands with increasing neutron energy, as higher energies enable more reaction pathways. Identifying the specific ions produced in these nuclear reactions is crucial, as each ion exhibits a unique stopping power, leading to varied effects on the reliability of electronic devices.

At high neutron energies, above several tens of MeV, the variety of ions produced is substantial, requiring specialized and complex computational models to analyze the effects on electronic devices. However, in our targeted energy range of 1 to 10 MeV, the variety of secondary ions is more limited, allowing us to adopt a simplified approach to discern general trends.

Table 3.2 presents the possible products of n+^{28}Si reactions below 10 MeV. As anticipated, the number of available reaction channels is limited; in addition to neutron capture (which is unlikely), there are only five possible reactions: one elastic and four nonelastic. The elastic reaction, which occurs at all energy levels without a threshold, conserves kinetic energy. In contrast, nonelastic reactions do not conserve kinetic energy, as some of the incident energy is used to excite the nucleus or to break nuclear bonds. A specific subset of nonelastic reactions includes inelastic reactions, which leave the target nucleus in an excited state. It's worth noting that "inelastic" is sometimes used interchangeably with "nonelastic", which can be misleading.

Each kind of nuclear reaction occurs with a specific probability which is quantified by the cross-section and depends on the neutron energy. Figure 3.5 shows the experimental cross-sections for the four first open channels, the production of deuterons being negligible. It turns out that the most probable reactions are the elastic and the inelastic ones, meaning that the most frequently produced secondary particle is the ^{28}Si ion. However, the production of ^{25}Mg is associated with the production of α-particle which has a role in the generation of Multiple Cell Upset (MCU). This is also the case concerning ^{28}Al, which is produced together with a proton, known to be able to trigger upsets in very integrated technologies. As a result, we must consider all possible reactions if we want to consider MCUs, but the elastic and inelastic reactions are enough to investigate the single bit upsets (SBU). In this latter case, the cross-section of n+^{28}Si reactions is about 1-10 barns.

Table 3.2: Reaction products as a function of incident energy for low energy neutrons (1-10 MeV) interacting with ^{28}Si [66].

Reactions products	**Reaction kind**	**Threshold energy (MeV)**
$^{29}\mathrm{Si} + \gamma$	Neutron capture	0
$^{28}\mathrm{Si} + n$	Elastic	0
$^{28}\mathrm{Si}^* + n$	Inelastic	1.78
$^{25}\mathrm{Mg} + \alpha$	Nonelastic	2.75
$^{28}\mathrm{Al} + p$	Nonelastic	4.00
$^{27}\mathrm{Al} + d$	Nonelastic	9.70

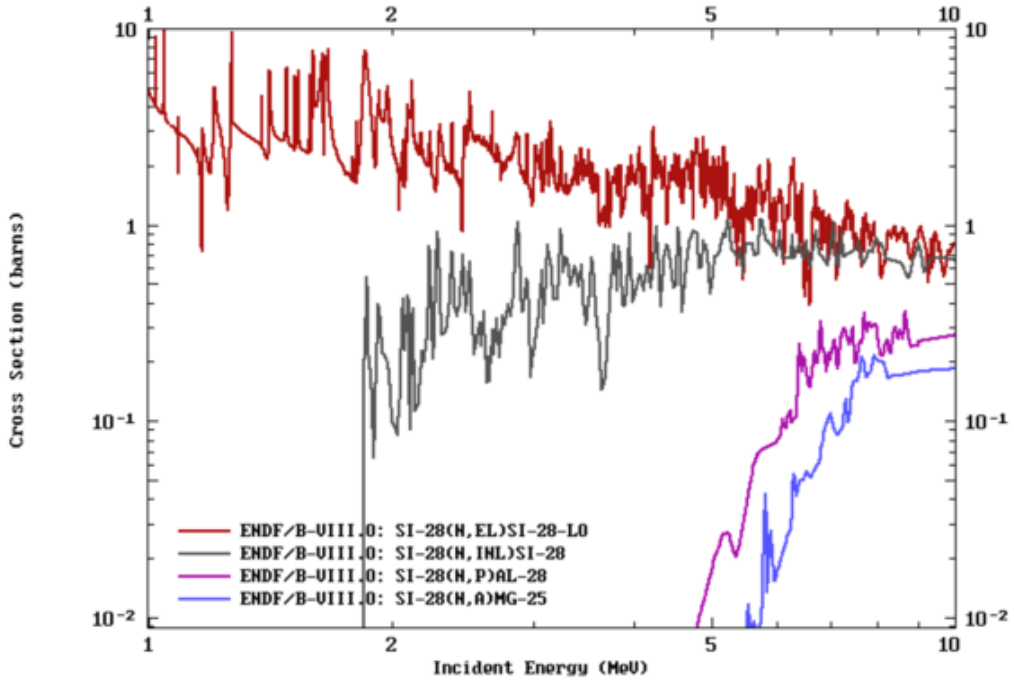

Figure 3.5: Experimental cross-sections for the interaction of neutron with ^{28}Si in the 1-10 MeV energy range [36]. There is no data for neutron absorption.

3.4 Development of a simplified tool to evaluate SER

SER are often computed using Monte Carlo tools, which are powerful but can require a long computation time. This work investigate an analytical approach to determine if it is possible to obtain a simple formula giving the SER as a function of representative parameters of the technology under study.

When a nuclear reaction occurs, some secondary ions are produced, which can trigger a soft error. The present work consider that an ion triggers a soft error if the following conditions are fulfilled:

- The ion must cross through the sensitive region of the device which is characteristic of the device. The boundaries of this sensitive volume are not clearly defined, and, for the sake of simplicity, this work consider that it is a sphere of radius R_S.
- The ion must deposit enough energy inside the sensitive volume. To fulfill that, this work consider that the ion must reach the sensitive volume with an LET higher than the threshold LET characteristic of the device and noted LET_{th}.

3.4.1 Ion generation rate and probability to reach the sensitive volume

The mean free path of neutron being quite long (typically 20 cm in silicon), we can assume that the rate of secondary ions produced in our electronic device is uniform. If we

consider a neutron energy range between E_{n1} and E_{n2}, the production rate $R(A, Z, E_{ion})$ of a secondary ion characterized by A, Z and an energy E_{ion} has an energetic distribution as follows:

$$\frac{dG(E_{n1}, E_{n2}; A, Z, E_{ion})}{dE_{ion}} = \int_{E_{n1}}^{E_{n2}} \frac{d\sigma(E_n; A, Z, E_{ion})}{dE_{ion}} \frac{d\phi(E_n)}{dE_n} dE_n \tag{3.5}$$

where:

- $G(E_{n1}, E_{n2}; A, Z, E_{ion})$ is the generation rate of the ion, given per unit of time and per target silicon nucleus.
- $\frac{d\sigma(E_n;A,Z,E_{ion})}{dE_{ion}}$ is the nuclear differential cross-section to produce an ion A, Z with an energy E_{ion} in the device.
- $\frac{d\phi(E_n)}{dE_n}$ is the differential neutron flux to consider.

Figure 3.6 plots the cumulative distribution of production rate of secondary silicon ions at ground level for the neutron energy range of 1 to 10 MeV and 1 to 200 MeV. These distributions have been computed using the DHORIN code [67] together with equation 3.5

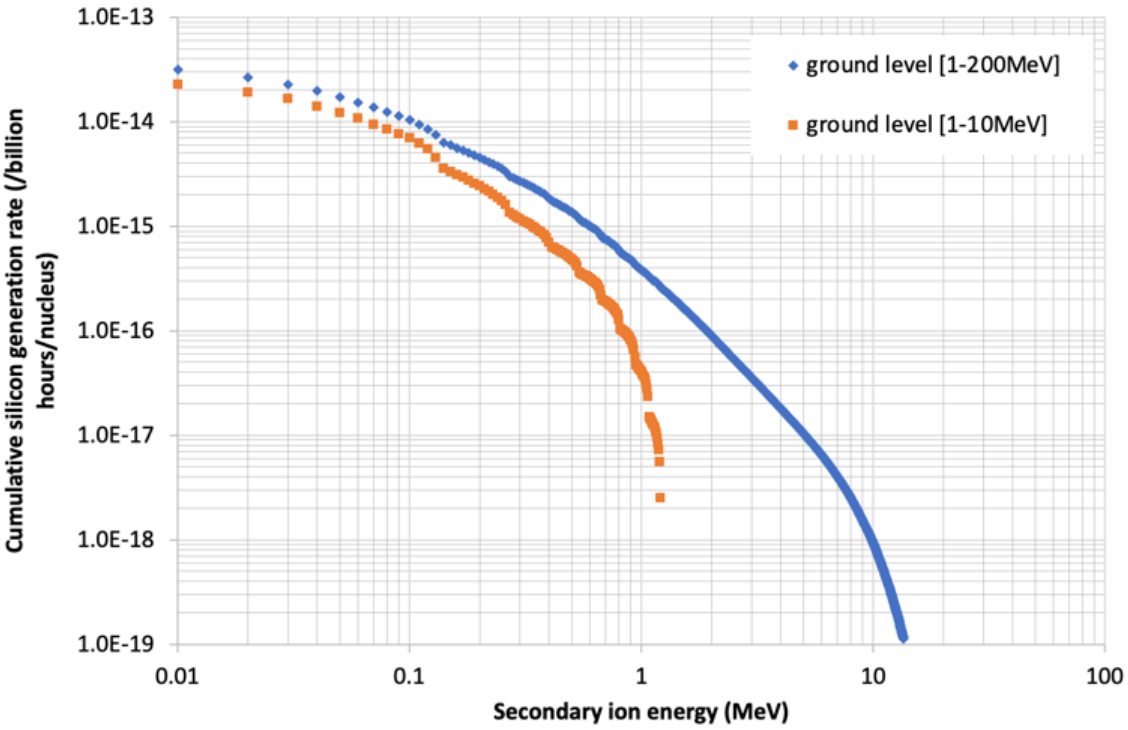

Figure 3.6: cumulative distribution of production rate of silicon at ground level for the neutron energy range of 1-10 MeV and 1-200 MeV.

If a given ion is produced at a distance r of the center of the sensitive volume, its probability $P_{geom}(r)$ to be emitted in the direction of the sensitive volume (whose radius is R_s) can be estimated by a simple geometrical consideration. This is justified by the

fact that, as neutrons are isotropic in atmosphere, secondary ions are too. Therefore, the probability for an ion to be emitted in the direction of the sensitive volume may be estimated by:

$$P_{geom}(r) = 1 \qquad if \qquad r < R_s \tag{3.6}$$

$$P_{geom}(r) \approx \frac{1}{4}(\frac{R_s}{r})^2 \qquad if \qquad r \geq R_s \tag{3.7}$$

3.4.2 Ion range and Threshold LET

The range $R(Z, A, E_{ion})$ of an ion is defined as the distance it can travel before being stopped [68]. Even if an ion is emitted in the direction of the sensitive volume, it will not reach the sensitive volume (SV) if its range is lower than the distance to cover ($\sim r - R_S$). Moreover, it must reach the sensitive volume with a high enough LET ($> LET_{th}$), which means that its energy must be between E_1 and E_2 such as $LET(E_1) = LET(E_2) = LET_{th}$ and $E_1 < E_2$. The ion must thus be generated with an energy greater than E_1 to have a chance to trigger a soft error. This is illustrated in Figure 3.7

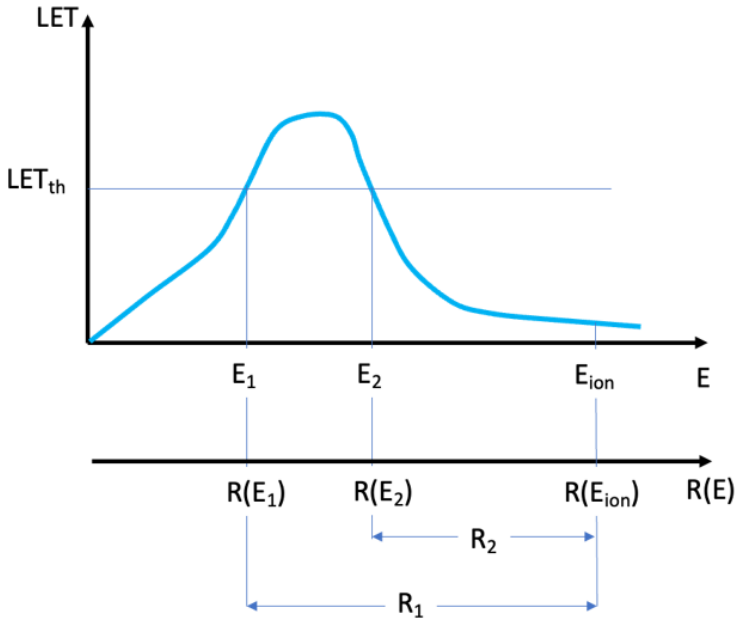

Figure 3.7: Illustration of the relationship between the threshold LET and the range of the particle.

Figure 3.7 shows that if an ion (with an energy E_{ion}) travels a too short distance (i.e. $< R_2$) before entering the SV, its LET will be lower than the threshold LET. Therefore, to trigger an event, it must cover at least the distance R_2. Similarly, if it covers a too long distance (longer than R_1), it will enter the SV with an energy lower than E_1, which corresponds to a LET below the threshold. Consequently, the distance ($\sim r - R_S$) traveled by the ion before reaching the SV must be comprised between R_1

and R_2. In other words, the distance r at which the ion is produced from the center of the sensitive volume must obey:

$$R_{min} \leq r \leq R_{max} \tag{3.8}$$

$$R_{min} = R(E_{ion}) + R_s - R(E_2) \qquad if E_{ion} > E_2 \tag{3.9}$$

$$R_{min} = 0 \qquad otherwise \tag{3.10}$$

$$R_{max} = R(E_{ion}) + R_s - R(E_1) \tag{3.11}$$

3.4.3 Probability to trigger a soft error

The first condition for an ion (A, Z) to be able to trigger a soft error is that its LET at the Bragg peak is higher than the threshold LET of the considered technology. This may be written by:

$$\forall E_{ion}, P_{SEU}(A, Z) = 0 \qquad if \qquad LET_{max}(A, Z) < LET_{th} \tag{3.12}$$

Otherwise, once generated with an energy E_{ion}, the probability that an ion (A, Z) triggers a soft error depends on both the probability of being emitted toward the sensitive volume and the condition on r given by the condition of the Equation 3.8. Therefore:

$$P_{SEU}(A, Z, E_{ion}) = \int_{R_{min}}^{R_{max}} 4\pi N_{Si} P_{geom}(r) r^2 dr \tag{3.13}$$

where N_{Si} is the number of silicon targets per unit of volume ($N_{Si} = 5\text{x}10^{22}\ at/cm^3$).

- If $E_{ion} > E_2$: the ion energy is higher than E_2 and P_{geom} is given by Equation 3.7. Therefore, it simply comes:

$$P_{SEU}(A, Z, E_{ion}) = \pi N_{Si} R_s^2 (R(E_2) - R(E_1)) \tag{3.14}$$

- If $E_{ion} < E_2$: we must distinguish ions that are produced inside and outside the sensitive volume. Using the Equation 3.14 we can reach the Equation 3.15, and solving the calculation leads to the Equation 3.16.

$$P_{SEU}(A, Z, E_{ion}) = \int_{R_{min}}^{R_S} 4\pi N_{Si} P_{geom}(r) r^2 dr + \int_{R_s}^{R_{Max}} 4\pi N_{Si} P_{geom}(r) r^2 dr \tag{3.15}$$

$$P_{SEU}(A, Z, E_{ion}) = \frac{4}{3}\pi N_{Si} R_s^3 + \pi N_{Si} R_s^2 (R(R_{ion}) - R(E_1)) \tag{3.16}$$

It is worth noting that the probability that an ion triggers a soft error is a polynomial of third degree in R_S in which the coefficients only depend on the threshold LET (included in E_1). In fact, the term with the power of 3 corresponds to a quantity linked to the volume of the SV and the term with the power of 2 to the area of the face of the SV.

3.4.4 Soft Error Rate Calculation

Finally, the soft error rate due to an ion (A, Z) generated by an atmospheric neutron in the $[E_{n1}; E_{n2}]$ energy range and for a technology characterized by its sensitive volume radius, R_s, and its threshold LET is given as follows:

$$SER(E_{n1}, E_{n2}; A, Z; R_s, LET_{th}) = \int_{E_1}^{\infty} P_{SEU}(A, Z, E_{ion}) \frac{dG(E_{n1}, E_{n2}; A, Z; E_{ion})}{dE_{ion}} dE_{ion} \tag{3.17}$$

where the integral starts at E_1 since below there is no possibility to trigger a soft error As the probability P_{SEU} has a different expression depending on the value of E_{ion} compared to E_2, we split the integral into two parts:

$$SER(E_{n1}, E_{n2}; A, Z; R_s, LET_{th}) = \int_{E_1}^{E_2} P_{SEU} \frac{dG}{dE_{ion}} dE_{ion} + \int_{E_2}^{\infty} P_{SEU} \frac{dG}{dE_{ion}} dE_{ion} \tag{3.18}$$

Finally, using equations from section 4.4.3 leads to:

$$SER(E_{n1}, E_{n2}; A, Z; R_s, LET_{th}) = I_v(LET_{th}) \times \frac{4}{3}\pi R_s^3 + I_s(LET_{th}) \times \pi R_s^2 \tag{3.19}$$

where I_V (volume term) and I_S (surface term) are two functions that depend only on LET_{th} and are defined by:

$$I_V(LET_{th}) = N_{Si} \int_{E_1}^{E_2} \frac{dG}{dE_{ion}} dE_{ion} \tag{3.20}$$

$$I_S(LET_{th}) = N_{Si} \int_{E_1}^{E_2} (R(E_{ion}) - R(E_1)) \frac{dG}{dE_{ion}} dE_{ion} + \int_{E_2}^{\infty} (R(E_2) - R(E_1)) \frac{dG}{dE_{ion}} dE_{ion} \tag{3.21}$$

The main conclusion from this extensive calculation is that we can now analytically determine the SER within a specified neutron energy range for a particular technology, defined by parameters R_s and LET_{th}. A key advantage of this approach is the separation of geometric considerations (R_s) from nuclear physics factors (I_V and I_S). These two components can be precomputed using specialized nuclear physics tools, allowing the SER to be calculated as a straightforward third-degree polynomial in R_s.

3.5 Main Results and Discussions

Using the DHORIN code, this work calculated the functions I_S and I_V, displayed in Figure 3.8 for the energy range of 1–200 MeV. Here, the I_V function represents nuclear reactions occurring within the sensitive volume, while I_S represents those initiated outside the sensitive volume.

To demonstrate the SER calculation, this work will consider an arbitrary technology examined in [62], which applied an enhanced BGR model. In this study, the sensitive volume was determined to be 4.5 μm^3 (corresponding to a sensitive volume radius of $R_s = 1.02\ \mu m$) and a critical charge of 30 fC (equivalent to a threshold LET of 2.82 $MeV.cm^2/mg$). From Figure 3.8, we find $I_V = 200$ FIT/Mcell/μm^3 and $I_S = 300$ FIT/Mcell/μm^2. Using Equation 3.19, we can compute the SER at ground level.

$$SER = 200 \times \frac{4}{3}\pi R_s^3 + 300 \times \pi R_s^2 = 1880 \quad FIT/Mcell \tag{3.22}$$

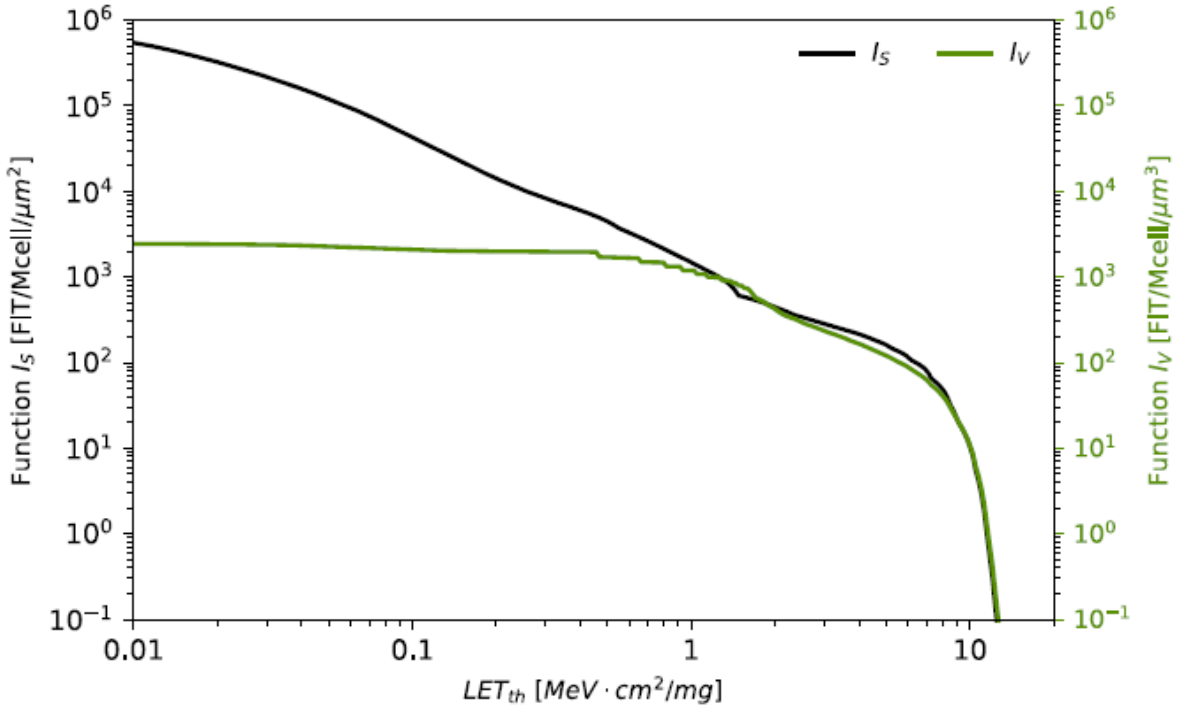

Figure 3.8: I_S and I_V as a function of LET for atmospheric neutrons in the 1 MeV–200 MeV energy range. I_S (left y-axis) is the contribution to the SER to be multiplied by the visible area of the sensitive volume. I_V (right y-axis) is the contribution to the SER to be multiplied by the size of the sensitive volume. This is calculated using DHORIN [67].

This calculated value aligns closely with the value in [62], which reported 1900 FIT/Mcell. However, [62] assessed the SER with a critical charge down to 10 fC, while modern technologies often have critical charges as low as 1 fC or even less. To validate our approach for critical charges below 10 fC, we compared our results with Monte Carlo simulation data from the literature [69], based on technology details from [70]. These

simulations assumed a cubic sensitive volume, for which we converted to an equivalent spherical radius to match our model.

The study involved four technologies, each with a different gate length (250 nm, 130 nm, 90 nm, and 65 nm). For each, the critical charge was known, and the threshold LET was estimated by dividing this charge by the sensitive volume radius (with appropriate unit conversions). Table 3.3 presents the parameters used, the SER obtained via Monte Carlo, and the SER derived from Equations 3.19, 3.20, and 3.21. Figure 5 shows the comparison between the SER values from the two methods. The difference was consistently below 13%, despite the differing modeling approaches and simplifications in our method.

It's noteworthy that our method tends to slightly overestimate the SER compared to the Monte Carlo method, which is acceptable for reliability purposes as it accounts for a worst-case scenario. Additionally, the slight decrease in this difference with technology downscaling is not fully understood and is likely attributable to the approximations in our approach.

Table 3.3: Comparison between the SER (at ground level) obtained by Monte Carlo simulations and the analytical approach developed in this document.

Gate Length (nm)	Sensitive Volume (μm^3)	R_s (μm)	Q_c (fC)	LET_{th} ($\frac{MeV.cm^2}{mg}$)	SER Monte Carlo ($\frac{FIT}{Mbit}$)	I_S ($\frac{FIT}{Mcell.\mu m^{-2}}$)	I_V ($\frac{FIT}{Mcell.\mu m^{-3}}$)	SER Analytical ($\frac{FIT}{Mcell}$)
250	0.245	0.388	8	1.99	237	380	380	272
130	0.025	0.181	2.5	1.34	103	913	913	116
90	0.01	0.134	1.2	0.87	107	1850	1323	117
65	0.0035	0.094	0.8	0.82	56.7	2068	1330	62

3.5.1 Contribution of the 1-10 MeV energy range to the SER

To investigate the contribution of the low-energy neutrons to the total SER at ground level, first we need to calculate I_V and I_S for the energy ranges 1–10 MeV. We investigated the contribution of the 1–10 MeV neutron energy range to the total SER (at ground level).

- **I_V calculation for 1-10 MeV**

  For neutrons within the 1–10 MeV energy range, this work used the DHORIN code to calculate the I_V term associated with the sensitive volume and plotted each secondary ion's contribution relative to the threshold LET. Figure 3.10 shows that the main contributors are recoiling silicon ions, produced through elastic and in-

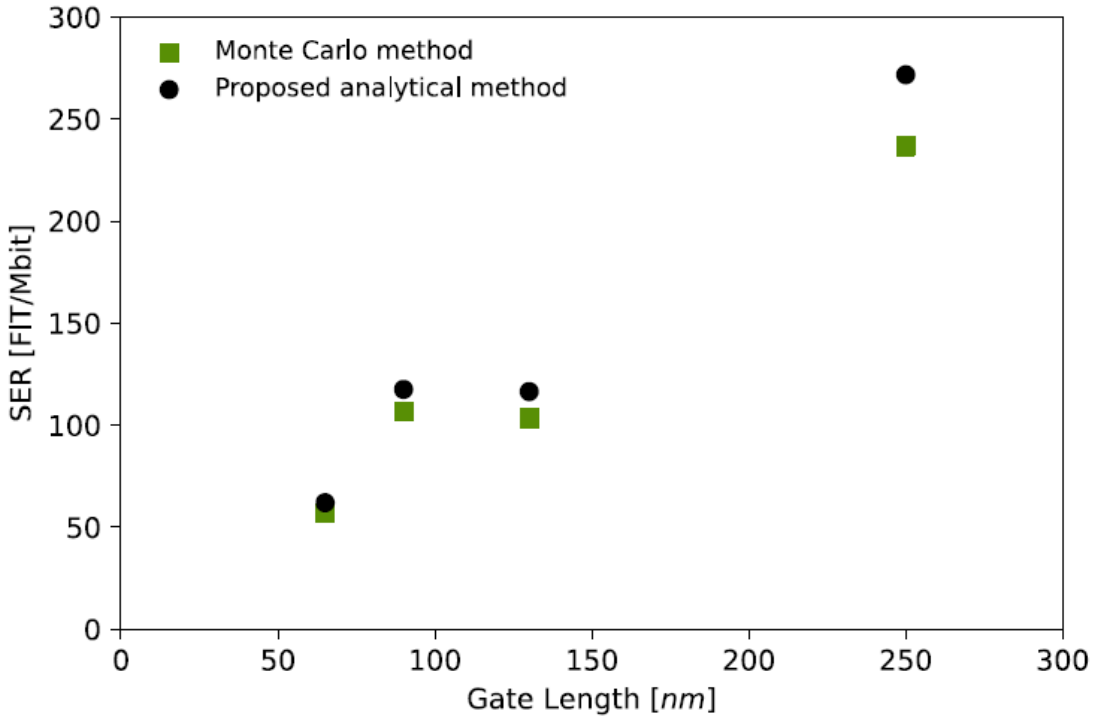

Figure 3.9: Comparison between the SER (at ground level) obtained by Monte Carlo simulations and the analytical approach developed in this document.

elastic reactions, except at very high LET_{th} values, where magnesium ions become dominant.

In modern technologies, where the typical threshold LET falls between 0.1 and 1 $MeV.cm^2/mg$, I_V lies within the range of 600–1100 FIT/Mcell/μm^3. In highly sensitive technologies that respond to direct ionization from protons, the threshold LET is below 0.54 $MeV.cm^2/mg$. For these highly sensitive technologies, I_V no longer depends on LET_{th}, meaning this contribution to the SER is driven purely by the sensitive volume's size. With continued downscaling, this contribution is expected to diminish, eventually becoming negligible. Contributions from light particles, such as protons and alphas, are minimal since they would need to be produced precisely at the Bragg peak within the sensitive volume, a highly improbable occurrence.

- **I_S calculation for 1-10 MeV**

Using the DHORIN code, we can calculate the I_S term associated with the visible surface of the sensitive volume and plot each secondary ion's contribution based on the threshold LET. As shown in Figure 3.11, above 1.45 $MeV.cm^2/mg$, the primary contributors are again recoiling ^{28}Si and ^{25}Mg ions. However, below 1.45 $MeV.cm^2/mg$, lighter particles (protons and alphas) become significant contributors, as they are produced outside the sensitive volume and can still reach it with sufficient LET. This explains the sharp increase in the I_S function be-

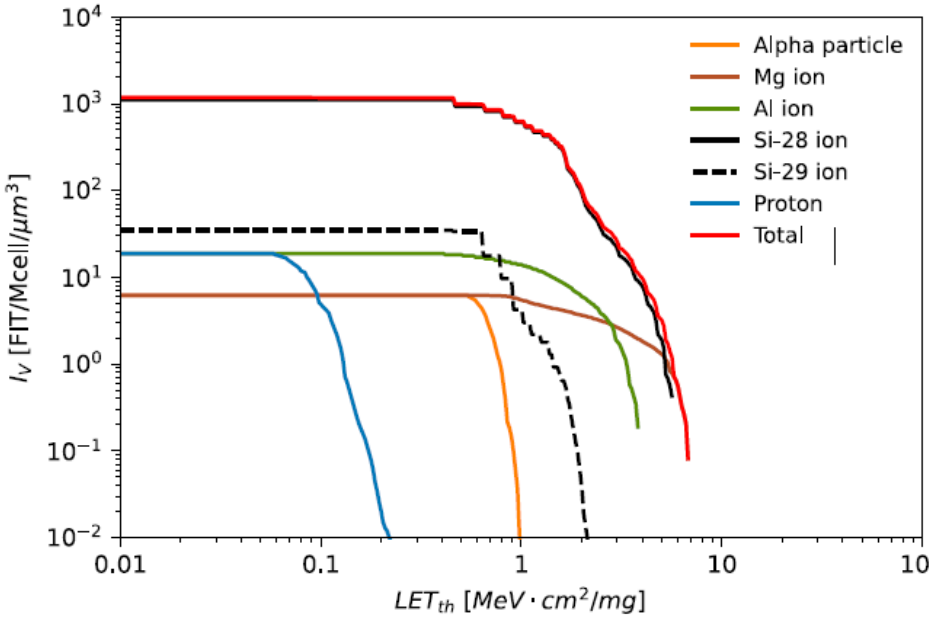

Figure 3.10: I_V calculation as a function of LET threshold for atmospheric neutrons in the 1-10 MeV energy range.

low 1.45 $MeV.cm^2/mg$ (due to alpha contributions) and even further below 0.54 $MeV.cm^2/mg$ (due to proton contributions).

These observations highlight the nuanced role that low-energy particles play in the SER for modern, highly sensitive technologies and emphasize the need to account for both I_V and I_S contributions across various LET thresholds.

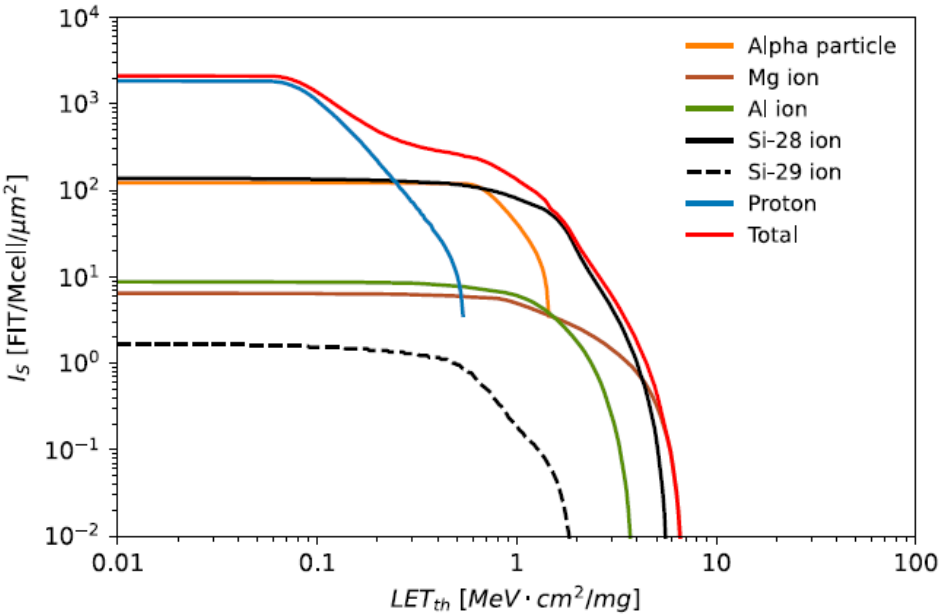

Figure 3.11: I_S calculation as a function of LET threshold for atmospheric neutrons in the 1-10 MeV energy range.

The results are presented in Figure 3.12 For the I_V function, the contribution of the

1–10 MeV energy range increased when the LET_{th} was decreasing (which corresponds to device downscaling). For $LET_{th} < 1.5\ MeV.cm^2/mg$ this contribution was quite constant, showing that there was a limitation of the low-energy range with downscaling. As far as the I_S function is concerned, the contribution of the 1–10 MeV energy range decreased for $LET_{th} < 1.5\ MeV.cm^2/mg$, meaning again that downscaling will not indefinitely increase the contribution of low-energy particles.

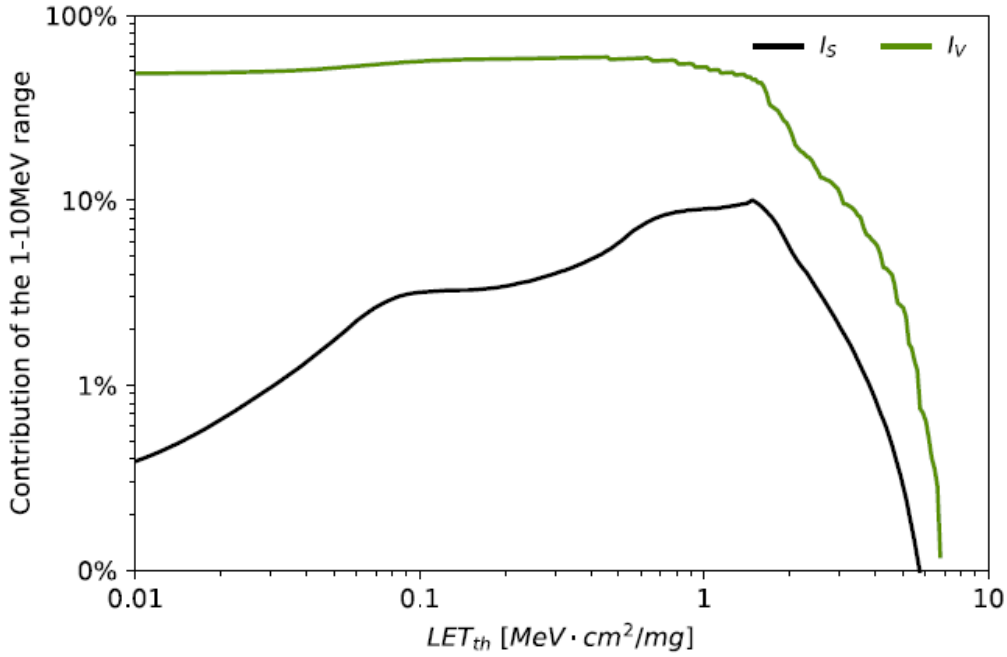

Figure 3.12: Relative contribution of the 1–10 MeV energy range compared to the 1–200 MeV range to the functions I_S and I_V as a function of threshold LET.

3.6 Conclusions

In this chapter, an analytical model has been proposed to investigate the SER contribution of low-energy neutrons (1–10 MeV). To develop an efficient method, this work separated the nuclear physics considerations (device sensitivity and nuclear reactions) from geometric factors (sensitive volume). Typically, an SEE is assumed to occur when an ion penetrates the sensitive volume with sufficient energy. Here, this assumption was slightly modified, positing that SEE occurrence is equivalent to reaching the sensitive volume with a high enough LET (LET_{th}).

The probability of an ion reaching the sensitive volume was computed analytically, while the nuclear physics component was calculated using the DHORIN code, yielding two primary functions: $I_V(LET_{th})$, which reflects nuclear reactions within the sensitive volume, and $I_S(LET_{th})$, representing reactions occurring outside it. These results demonstrated strong agreement with Monte Carlo simulations from the literature. The evaluations of the 1–10 MeV and 1–200 MeV ranges indicate that with continued device downscaling, the contribution of the lowest energy range is unlikely to increase signifi-

cantly. Therefore, a sharp rise in the SER from low-energy atmospheric neutrons is not expected, even with increased sensitivity as indicated by decreasing LET_{th}.

While this method focuses on atmospheric low-energy neutrons, it can be adapted to other environments, such as accelerators. In these cases, knowing the neutron spectra and calculating the ion generation rate using a tool like DHORIN allows for the straightforward computation of $I_V(LET_{th})$ and $I_S(LET_{th})$, enabling evaluation of the specified energy range's contribution to the total SER.

Chapter 4

SEE cross-section analysis for low-energy Protons

As discussed in Chapter 3, the downscaling of electronic devices has substantially increased their sensitivity to low-energy particles like neutrons and protons [7, 66, 4]. These particles, both classified as hadrons, can induce single event effects (SEE) by generating secondary ions that ionize the silicon within the device. These secondary ions result from nuclear reactions initiated by strong force interactions (hadronic process) [71]. Due to similarities in how neutrons and protons interact with electronics, devices are generally considered equally sensitive to both particle types, at least for energies above a few tens of MeV [72]. However, protons can also induce recoil ions via Coulomb interactions and direct ionization [73, 74].

Memory devices are highly susceptible to SEEs, particularly Single Event Upsets (SEUs). The susceptibility of memory devices to radiation effects, especially in relation to proton irradiation, has been widely researched [75, 76, 77]. Analysis has identified two primary mechanisms driving SEU sensitivity: direct ionization from low-energy protons (around 1 MeV) [78, 77] and nonelastic nuclear reactions from higher-energy protons (>10 MeV) [79, 80]. Recent studies have also highlighted the considerable role of Coulomb elastic scattering within the 1 to 10 MeV energy range [73, 74, 75, 76]. Due to the infinite range of Coulomb interactions, the likelihood of elastic recoil is particularly high. In [73], equations were developed to calculate the SEE cross-section associated with silicon recoils resulting from elastic scattering. However, this approach can be complex for users without specialized knowledge in physics, electronics, and particle-matter interactions. The study in [76] examined more complex devices and configurations to understand proton irradiation mechanisms, using Monte Carlo simulations to model proton interactions. Nevertheless, this approach is limited due low-energy recoil ions (as will be discussed in Section 5.3). Direct Monte Carlo simulations requiring prolonged calculation times to accurately capture the high-energy tail of the spectrum.

In this chapter, we explore the mechanisms underlying the elastic process and extend the analysis by presenting a methodology to evaluate electronic sensitivity to low-energy protons. The goals here is to establish a straightforward method for calculating and predicting the SEE cross-section for low-energy protons.

4.1 Nuclear-matter interaction background

To develop a method for calculating the SEE cross-section, it is essential to first understand the interactions that occur between particles and matter. When a proton or neutron collides with an atomic nucleus, three possible processes may take place:

- **Capture process:** in this process, the incoming proton or neutron is captured by the target nucleus, resulting in the emission of gamma radiation to de-excite the newly formed nucleus. Due its weak effect, this process will not be further discussed here.
- **Elastic process:** In an elastic interaction, the incident proton or neutron scatters off the target nucleus, causing the target nucleus to recoil as energy and momentum are transferred. Figure 4.1 illustrates the elastic mechanism. The elastic scattering process involves the interaction of a nucleon with a target nucleus without any change in the system's internal energy, *i.e.*, the conservation of total kinetic energy. During this recoil, the ion generated can potentially trigger SEE [81, 43].
- **Nonelastic process:** In nonelastic interactions, the incoming nucleon may excite or fragment the target nucleus. This process often leads to the generation of secondary particles, including ions that can trigger failures in electronic devices. Figure 4.2 illustrates the nonelastic mechanism [43].

Unlike neutrons, protons are charged particles and can interact directly with matter via the Coulomb force [73, 76]. This introduces two specific types of Coulomb interactions:

- **Coulomb interaction with the electrons:** this interaction occurs when the primary proton interacts with the electrons in the medium, transferring energy and ionizing the medium directly. This ionization process can lead to SEE in electronic devices [43, 82].
- **Coulomb interaction with the nuclei:** in this elastic process, protons interact with the nuclei in the medium through the Coulomb force, causing the impacted nucleus to recoil. This recoil can result in secondary ionization, contributing to the overall SEE rate in electronic devices. The total elastic interaction in proton–nucleus collisions thus combines two components: the strong force interaction and the Coulomb interaction [83].

Proton interaction processes share many similarities with those of neutrons. To differentiate their effects, it's important to understand each process's contributions and examine the reaction products generated when both particles interact with matter. Each reaction type has a specific threshold energy, which is the minimum energy needed to produce secondary particles. Table 4.1 lists possible neutron and proton reactions below 10 MeV, illustrating the distinct reaction pathways for each particle.

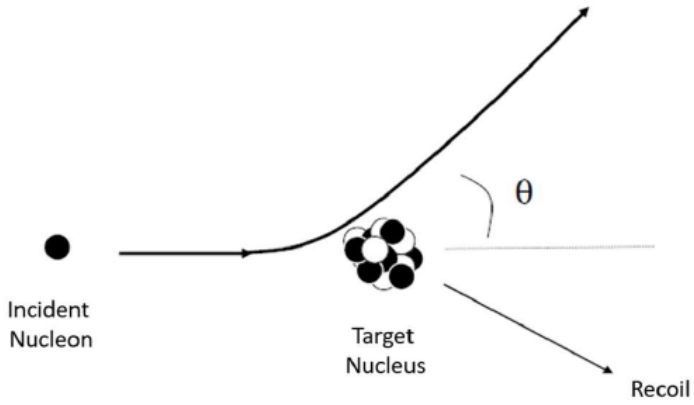

Figure 4.1: Elastic reaction leading to the deflection of the incident nucleon and the recoil of the target nucleus. The recoil ion may be responsible for an SEE.

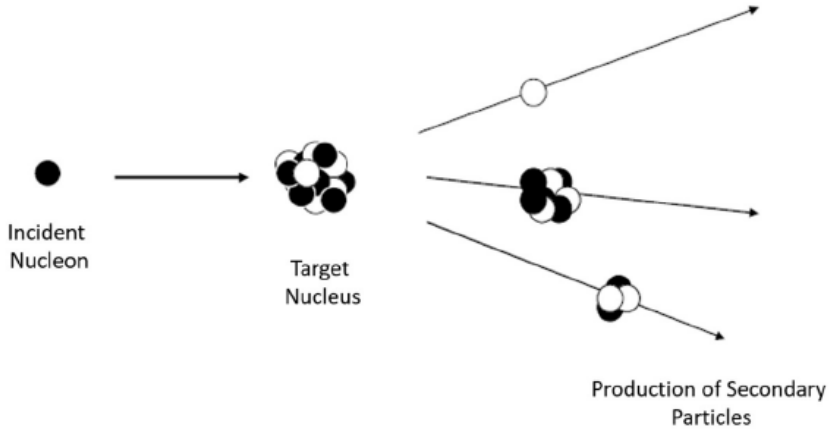

Figure 4.2: Nonelastic reaction leading to the production of secondary particles. The secondaries may ionize the matter and trigger SEE.

Table 4.1: Reaction products as a function of incident energy for neutrons and protons in ^{28}Si below 10 MeV.

Incident Particle	**Reactions products**	**Reaction kind**	**Threshold energy (MeV)**
Neutron	$^{29}\mathrm{Si} + \gamma$	Neutron capture	0
	$^{28}\mathrm{Si} + n$	Elastic	0
	$^{28}\mathrm{Si}^* + n$	Inelastic	1.78
	$^{25}\mathrm{Mg} + \alpha$	Nonelastic	2.75
	$^{28}\mathrm{Al} + p$	Nonelastic	4.00
	$^{27}\mathrm{Al} + d$	Nonelastic	9.70
Protons	$^{29}\mathrm{Si} + \gamma$	Neutron capture	0
	$^{28}\mathrm{Si} + \rho$	Elastic	0
	$^{25}\mathrm{Al}^* + \alpha$	Nonelastic	7.99

Based on Table 4.1, below 10 MeV, neutrons have four possible nonelastic reactions, while protons only have one. This is due to the charge of protons, which makes it more challenging to enter the nucleus and generate secondary ions. Looking at the only

product generated by the proton, the aluminum production, it is insignificant for SEE contribution. This is shown in Figure 4.3, in which we plotted the reaction cross-section from the International Atomic Energy Agency (IAEA) database [84].

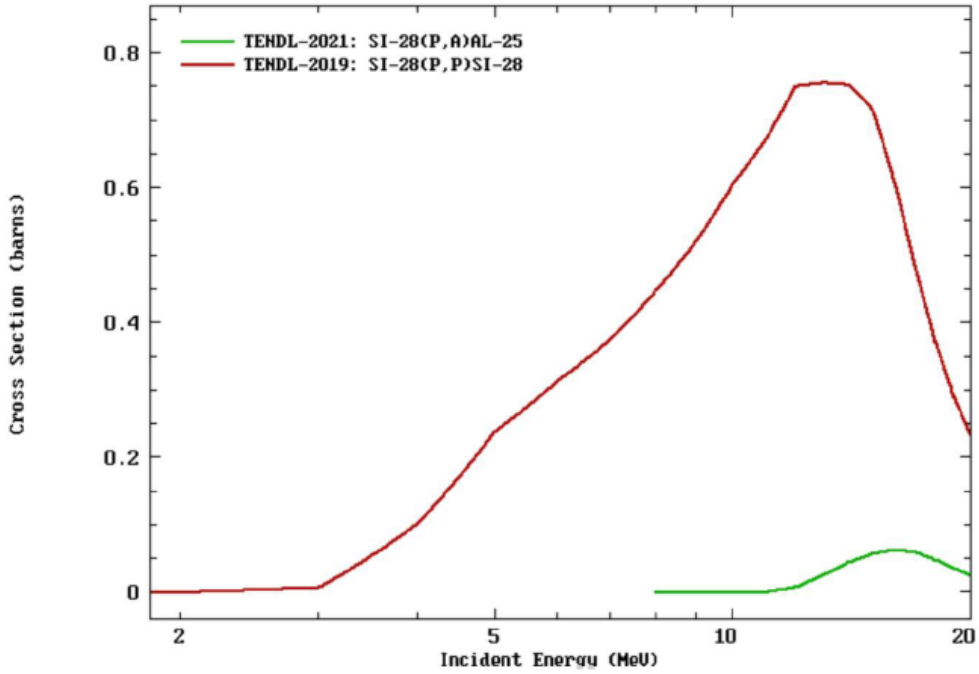

Figure 4.3: Nuclear cross-sections for p + ^{28}Si interaction. Data from IAEA data [84].

Finally, for protons below 10 MeV, the main process at play is the elastic reaction [73], which can be due to the strong force (hadronic process) and, at the same time, to the Coulomb force.

4.2 Approach to calculate SEE cross-section

As discussed in the previous section, the elastic reaction is critical for understanding low-energy proton interactions. The next step is to develop a methodology for calculating the proton SEE cross-section, $\sigma_p(E_p)$. One approach is to use experimental data on heavy-ion cross-sections, $\sigma_{HI}(LET)$, as a foundation [85]. To determine $\sigma_p(E_p)$, we express it as follows:

$$\sigma_p(E_p) = \int_0^{LET_{max}} \frac{dP(E_{th})}{dLET} \sigma_{HI}(LET) dLET \tag{4.1}$$

In Equation 4.1, $\frac{dP(E_{th})}{dLET}$ represents the LET distribution of the recoiling ions and secondary products generated during nucleon transport within the material. The parameter LET_{max} is the highest ion LET produced by proton interactions at a given energy (E_p). To calculate the LET distribution, we first derive the cumulative probability $P(E_{th})$ of a proton crossing a target material of thickness δx, given the number

of atoms per unit volume (N) and the nuclear cross-section (σ_{prod}). This probability is represented by Equation 4.2.

$$P = 1 - e^{-N\sigma_{prod}\delta x} \tag{4.2}$$

where N is $5 \times 10^{22} atoms/cm^3$ for silicon.

To further develop this method, it is necessary to examine the nuclear elastic cross-section in Si. It is important here to distinguish between the SEE cross-section, which measures the sensitive area of the device impacted by the particle interaction, and the nuclear cross-section, which reflects the probability of a particle producing a nuclear reaction.

4.2.1 Nuclear Elastic cross-section Analysis

To explore the nuclear elastic cross-section, σ_{prod}, for energies below 10 MeV, this work simulated neutron and proton interactions with a silicon nucleus using the DHORIN code [67]. DHORIN employs a spherical optical model and calculates angular differential cross-sections using the ECIS code [86]. Through relativistic kinematics, DHORIN computes the differential cross-section as a function of the silicon recoil's kinetic energy. Figures 4.4 and 4.5 display the results for protons at 5 MeV and 10 MeV, respectively, along with neutron interactions at the same energies for comparison.

For energies above 100 keV, neutron and proton cross-sections exhibit similar shapes and magnitudes. However, below 100 keV, there is a significant increase in the proton cross-section due to the Coulomb interaction, which does not affect neutrons. At very low energies, the differential cross-section for protons becomes several orders of magnitude greater than for neutrons, driven by the Coulomb force.

To estimate the proton SEE cross-section, it is essential to determine a threshold energy (E_{th}) beyond which a recoil ion can trigger a fault in the device. For protons and silicon ions, this threshold energy is expected to be similar. In devices sensitive to direct proton ionization, a reasonable approximation for E_{th} is around 50 keV, which corresponds to the proton energy near the Bragg peak (LET is maximized). In this context, recoil ions can trigger faults if their energy exceeds E_{th}. Figure 4.6 presents elastic cross-section results for various threshold energies as a function of incident proton energy, while Table 4.2 provides typical E_{th} values for different technologies.

This analysis demonstrates that low-energy proton interactions significantly impact energy deposition in silicon through both direct ionization and elastic reactions. However, this initial approach does not consider that recoils are not always generated within the device's sensitive volume (i.e., the silicon substrate layer) and may lose energy before reaching it, such as in the back-end of line (BEOL) layers. Consequently, the differential cross-section varies along the particle track and must be adjusted accordingly for accurate SEE predictions.

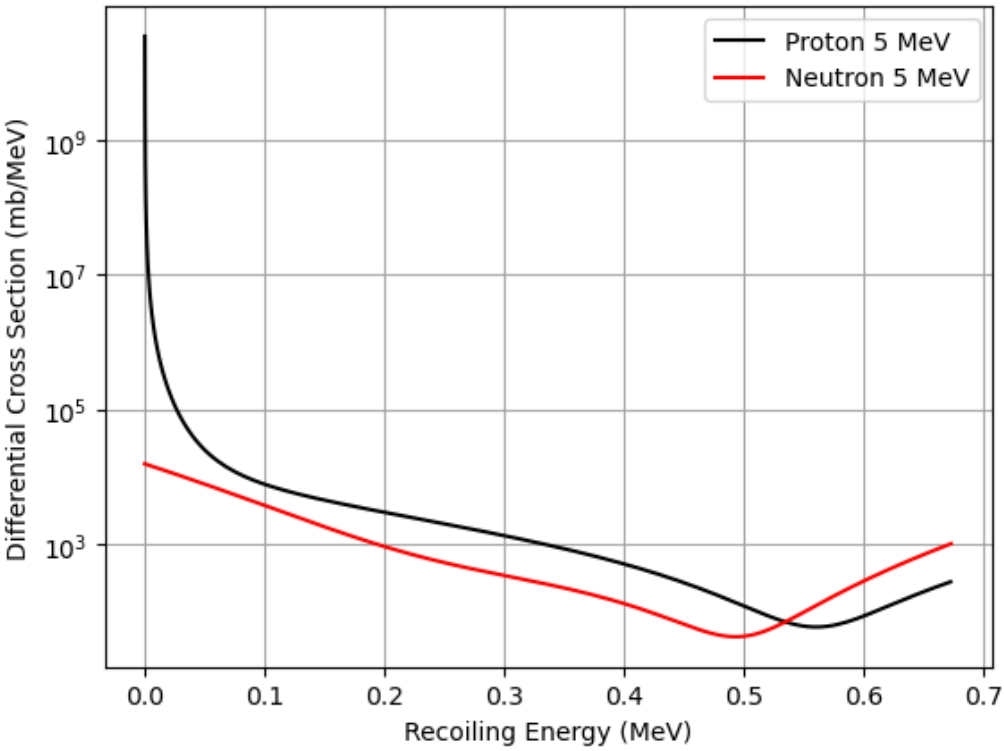

Figure 4.4: Differential cross-section for incident neutrons and protons at 5 MeV and as a function of recoiling energy.

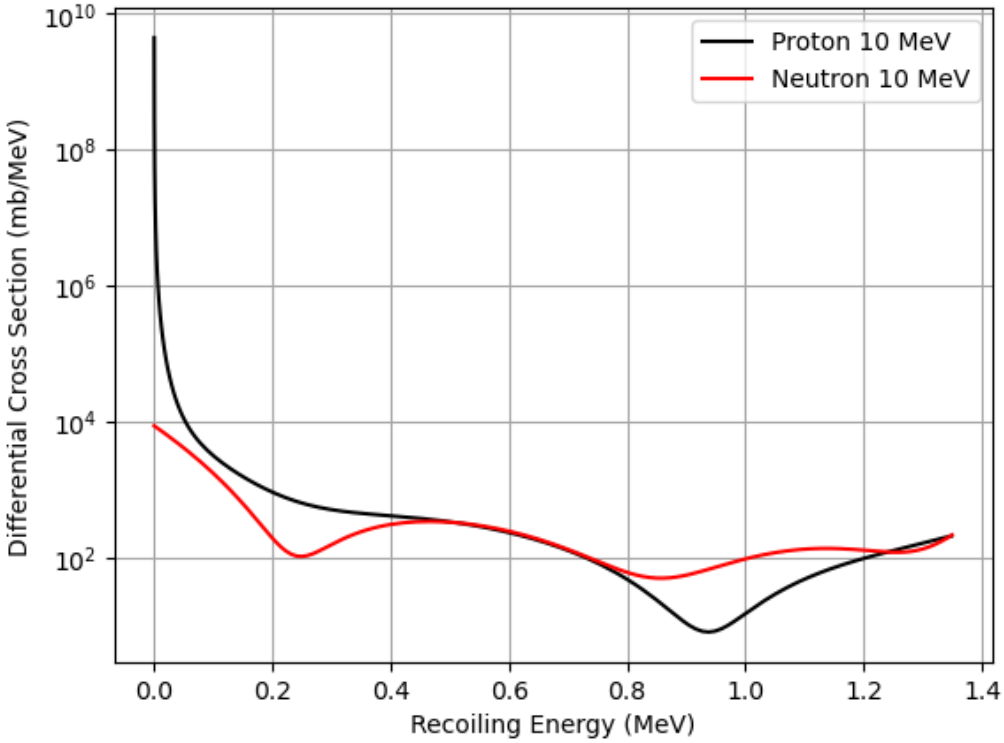

Figure 4.5: Differential cross-section for incident neutrons and protons at 10 MeV and as a function of recoiling energy.

Table 4.2: Typical critical charge (Qc), LET_{th}, and E_{th} for different technologies.

Gate length (nm)	**Qc (fC)**	**LET**$_{th}$ $(MeV.cm^2/mg)$	E$_{th}$ (keV)
250	8	1.99	180
130	2.5	1.34	56
90	1.2	0.87	27
65	0.8	0.82	18

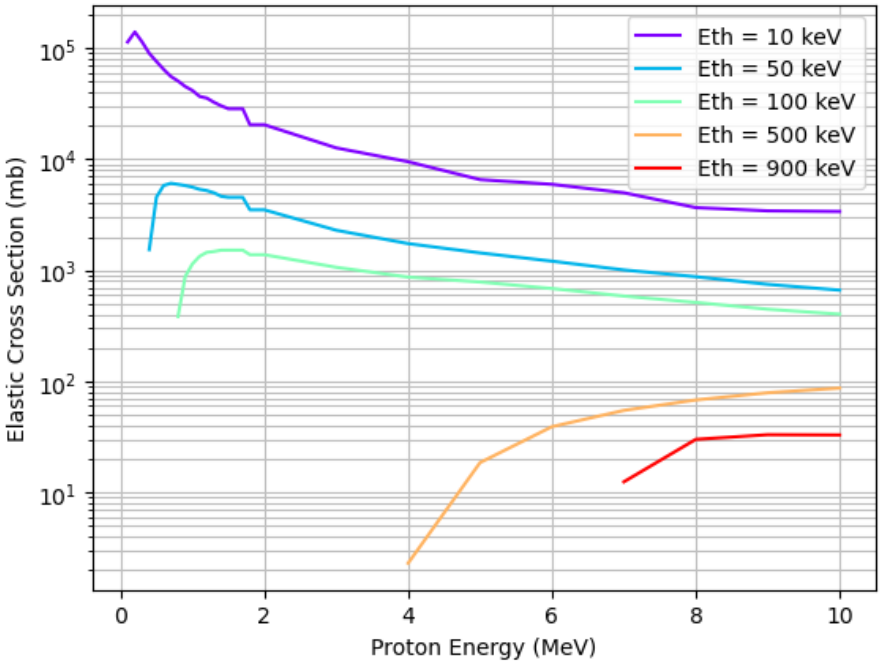

Figure 4.6: Elastic cross-section as a function of proton energy for different threshold energies.

4.2.2 Typical Ion Recoiling Ranges

To better understand the effects of track length, Table 4.3 summarizes typical ranges for proton and silicon ions in silicon. The first row lists the incident proton energies considered. The second row provides the proton ranges in silicon, calculated using the SRIM code [44]. The third row lists the maximum kinetic energy a silicon recoil ion can have, based on differential cross-section data from DHORIN. The last two rows, also from SRIM, show the maximum LET and range associated with this recoil, determined by calculating the differential cross-section and relating energy to the nucleon scattering angle (180° being the maximum achievable angle).

Table 4.3: Typical recoiling ranges of ions in silicon.

Proton energy (MeV)	1	5	10
Proton range in Si (μm)	16	200	700
Maximum recoiling energy of Si (MeV)	0.13	0.68	1.30
Maximum LET of the recoil in Si $(MeV.cm^2/mg)$	2.8	4.1	6.2
Maximum range of recoiling Si in Si (μm)	0.18	2.70	3.50

The key insight here is that recoiling ions must originate within a narrow BEOL layer to reach the sensitive region effectively. For instance, at 10 MeV, a recoiling silicon ion can have up to 1.3 MeV in energy, necessitating its generation within 3.5 μm of the sensitive region to reach it. As the proton range in silicon at low energy (a few MeV) is comparable to the BEOL thickness, it becomes necessary to account for the energy lost by the primary proton before the elastic collision that produces the recoiling silicon ion capable of causing an SEE.

4.2.3 Energy loss modeling

To model this energy loss, we simulate a structure with two silicon layers: one representing the BEOL and the other representing the sensitive region within the silicon bulk. Although the actual BEOL comprises various materials, its precise composition is generally proprietary; hence, a simplified silicon-based model is used here. The sensitive region is typically modeled as being 1–2 μm thick, corresponding to the charge diffusion during ionization.

When a silicon ion recoils inside this sensitive region, its initial LET can be estimated based on its recoil energy. However, if the recoil occurs outside the sensitive region, we must consider energy loss before it enters, meaning the effective LET will differ from the initial LET. Figure 4.7 illustrates how a silicon recoil ion generated at a distance x from the sensitive region loses energy as it traverses the intervening material.

The objective here is to model the LET distribution of secondary ions reaching the sensitive region. Although a Monte Carlo approach would suit this type of calculation, it would mostly capture low-energy recoils due to the low-energy divergence seen in Figures 4.4 and 4.5. To avoid excessive computation time, this work propose an analytical approach, calculating the nuclear cross-section for producing ions capable of reaching the sensitive region at each position within the structure. By using SRIM, it is possible estimate the probability of creating such ions in small layers at each depth. To run this analysis, three input parameters are necessary: the incident proton energy (E_p), BEOL layer thickness (t_{BEOL}), and sensitive region thickness (t_{SR}).

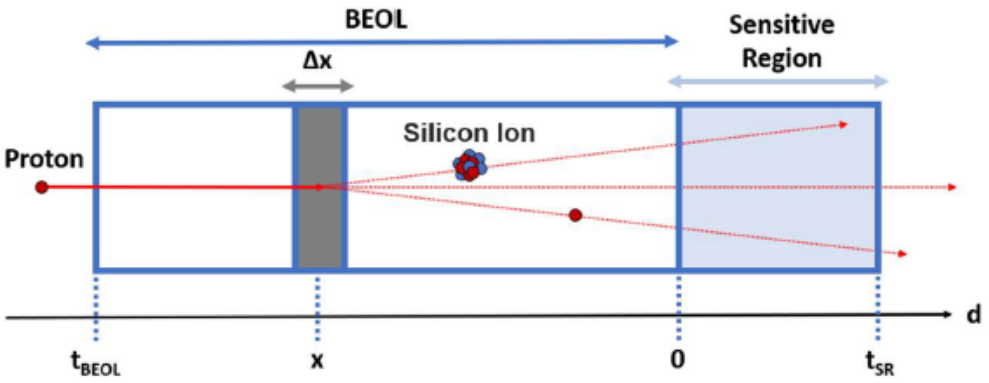

Figure 4.7: Illustration of an elastic collision in the BEOL. The recoiling silicon loses energy along its track and can reach the sensitive region with different LET.

From this methodology, we derive range functions for protons and silicon ions in silicon. Let $R_p(E_p)$ denote the proton range function and $R_{Si}(E_{Si})$ the silicon ion range function, both dependent on particle energy and readily obtainable with SRIM [44]. We also require the inverse functions R_p^{-1} and R_{Si}^{-1}, which yield particle energy from a known range. Using these functions, we can determine proton energy at any point along the d-axis by:

$$E_p(x) = R_p^{-1}(R_p(E_p(t_{BEOL})) - (t_{BEOL} - x)) \tag{4.3}$$

Now, for an ion produced at the position (x) with an energy $E_{Si}(x)$ to reach the sensitive region with an energy greater than the energy threshold (E_{th}), we need to have:

$$E_{Si}(x; LET_{th}) = R_{Si}^{-1}((R_{Si}((E_{th}(LET_{th})) + x) \tag{4.4}$$

For different values of LET_{th}, we calculate E_{th} based on the maximum LET of a silicon recoil. Next, we calculate the cross-section (σ_{prod}) to generate an ion at position x with sufficient energy to reach the sensitive region. This cross-section is obtained by integrating the recoil distribution at $E_p(x)$ between $E_{Si}(x; LET_{th1})$ and $E_{Si}(x; LET_{th2})$. The probability that such an ion is created in the δx layer is given by Equation 4.2.

By integrating over all x values, we can determine the initial probability. For thin layers, most protons pass through the silicon and enter the sensitive region with energy calculated by Equation 4.3, which adds to the initial probability to yield the cumulative probability. The LET distribution then includes these primary protons as the direct ionization peak.

4.2.4 Cumulative probability calculation

In this moment, the proposed approach enables us to determine the cumulative probability of ions reaching the sensitive region. This probability represents the likelihood of an ion arriving at the sensitive region with an LET exceeding a specified value. Figure 4.8 shows these distributions for incident protons with energies from 1 to 10 MeV. For LET values above 2 $MeV.cm^2/mg$, the probability of triggering an SEE increases with proton energy. Below 2 $MeV.cm^2/mg$, however, lower-energy protons become the dominant contributors to the cumulative probability. At very low LET values (below 0.2 $MeV.cm^2/mg$), the direct ionization peak is the primary contributor, with a probability 3–4 orders of magnitude higher.

This finding is significant, as it is often assumed that higher sensitivity (i.e., lower LET threshold) reduces recoil probability, leaving direct ionization as the main concern. Here, we clearly see that as incident energy decreases, the probability of low-LET recoiling ions increases. Using these results, we can finally apply Equation 4.1 to calculate the SEE cross-section.

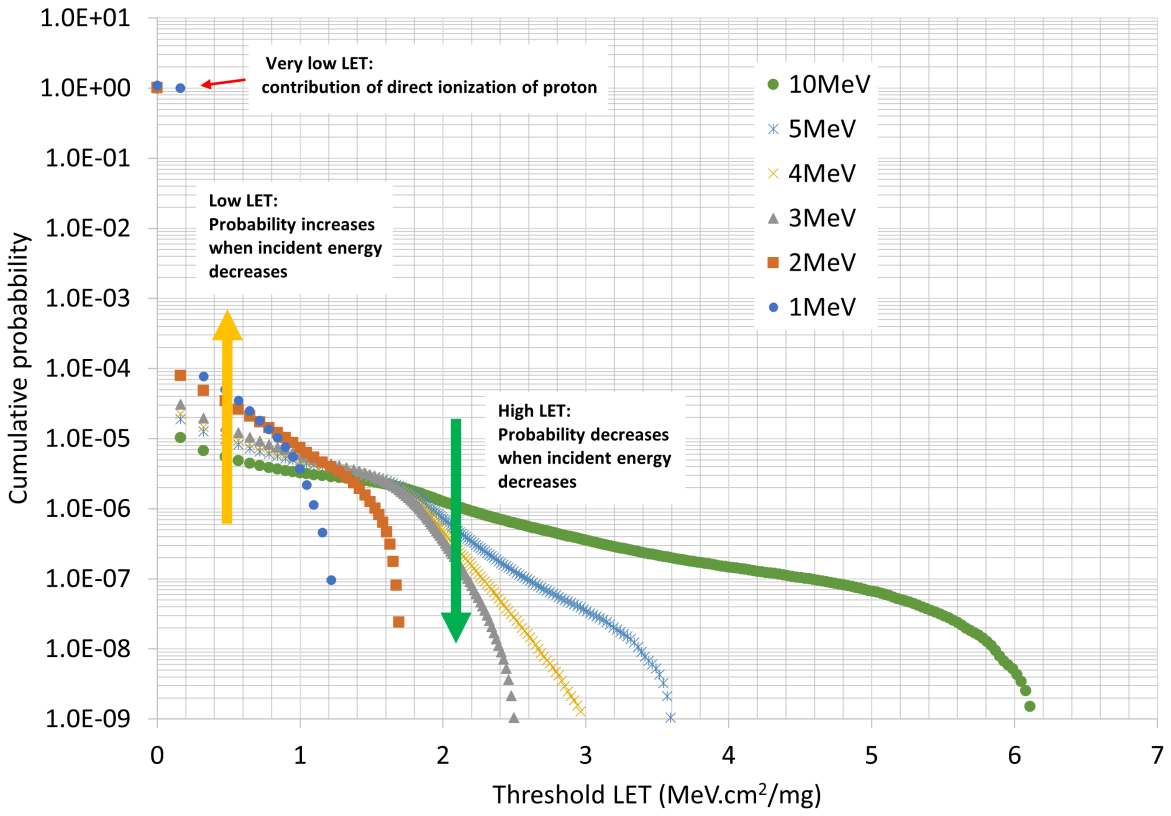

Figure 4.8: Cumulative probability to obtain a silicon recoil with a LET $> LET_{th}$ for different proton energies. In this example, the BEOL thickness is 10 μm. The sensitive region layer is 1 μm.

4.3 Results and discussion

To validate the proposed method, the SEU cross-section results for 90 nm, 65 nm, and 40 nm SRAMs were used as a reference [87, 88]. The $\sigma_{HI}(LET)$ was fitted using a power law, which serves as an alternative to the Weibull shape [89]. Figures 4.9(a), 4.10(a), and 4.11(a) show this power law in comparison to the experimental $\sigma_{HI}(LET)$ results. The results are plotted in Figures 4.9(b), 4.10(b), and 4.11(b) alongside the experimental SEU cross-section.

For the 90 nm node, the input parameters are a BEOL thickness of 10 μm, a sensitive region thickness of 2 μm, and a heavy-ion LET_{th} of 0.5 $MeV.cm^2/mg$. For the 65 nm node, we used a BEOL thickness of 15 μm, a sensitive region thickness of 2 μm, and a heavy-ion LET_{th} of 0.4 $MeV.cm^2/mg$. For the 40 nm node, the BEOL is 6 μm thick, with a sensitive region thickness of 1 μm and a heavy-ion LET_{th} of 0.2 $MeV.cm^2/mg$. BEOL thickness was approximated by considering the energy loss of the proton in silicon, making it possible to estimate the energy at which the direct ionization peak occurs.

The results show consistent alignment with the experimental data, though they do not perfectly match. Despite this, the SEU cross-section evaluation is robust. The simulation requires only four input parameters, and although some simplifications were necessary (such as approximations of dimensions and structural composition for each technology node), the results demonstrate substantial consistency with experimental data. Notably, we observe a direct ionization peak around 1 MeV and a significant cross-section between 1 and 10 MeV. Again, below 10 MeV, we have a major contribution of elastic scattering. The results could be improved if we would have had more data about the technology, in particular:

- Greater information on BEOL thickness;
- More details about the BEOL composition;
- Additional experimental heavy-ion data, especially between 0.2 to 0.8 $MeV.cm^2/mg$.

In calculating the SEE cross-section, there are several crucial considerations:

- Differential cross-section Calculation: This work utilized the DHORIN code, but other tools may be suitable as long as Coulomb scattering is accounted for.
- Primary Proton Energy Loss: Accounting for the primary proton's energy loss is essential as it dictates the secondary ion energy distribution.
- Secondary Ion Path Length: It is vital to consider the distance secondary ions travel before reaching the sensitive region.
- Appropriate cross-section Model: Avoid using a simple step-function model for SEE cross-section calculations, as it could lead to significant inaccuracies.

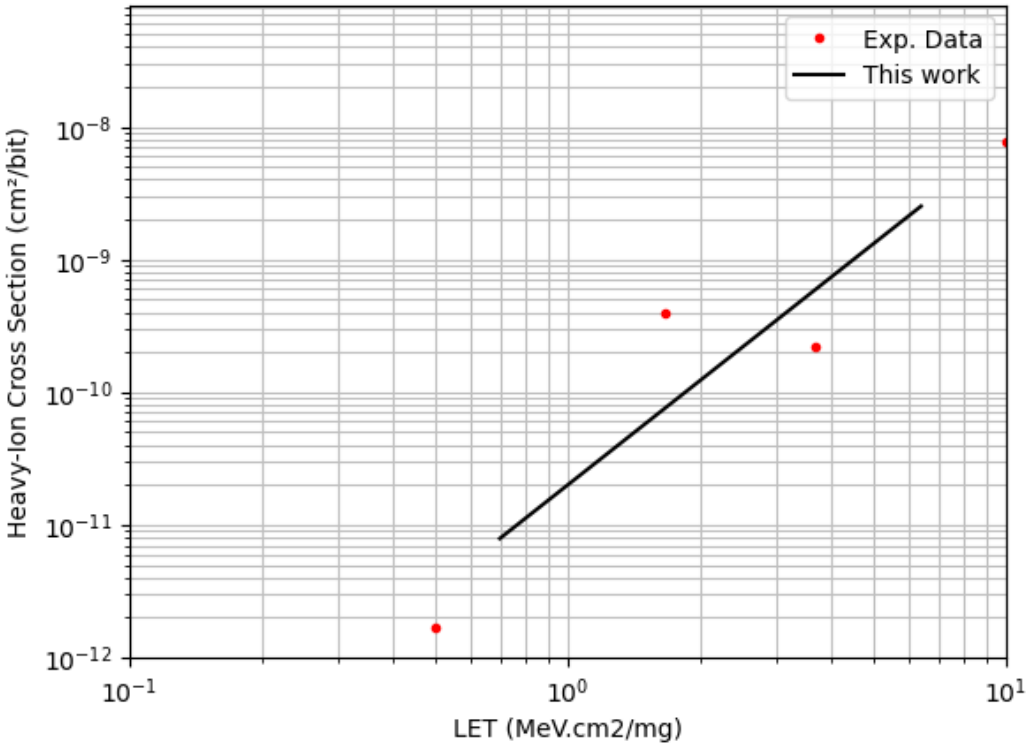

(a)

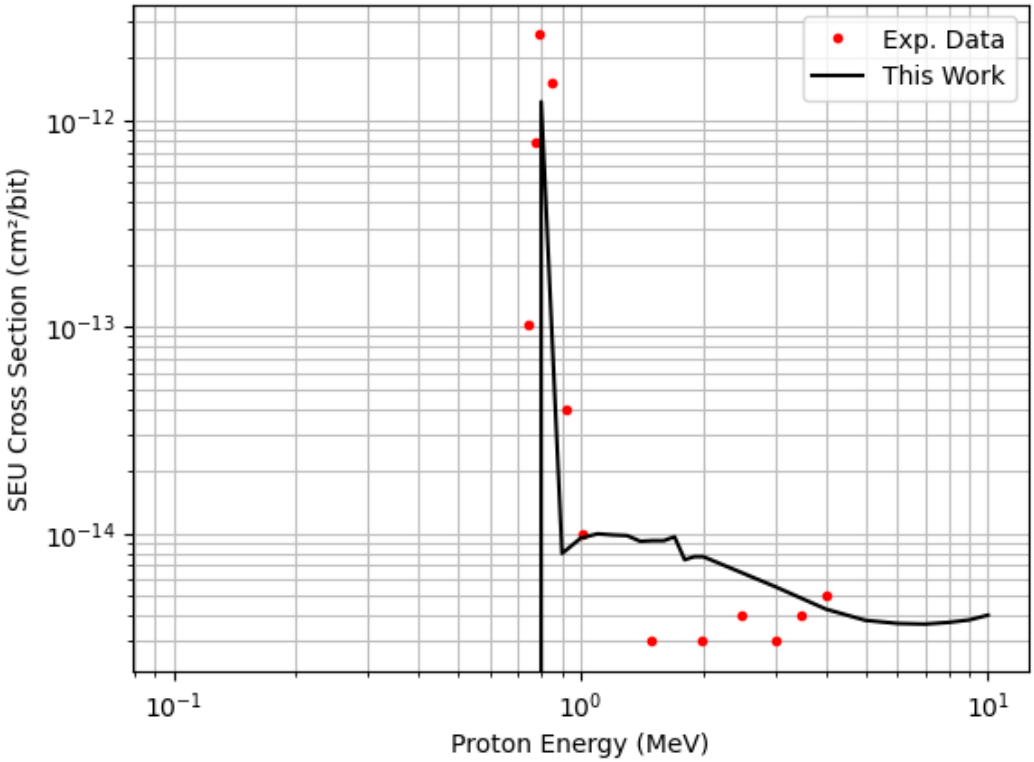

(b)

Figure 4.9: 90 nm SRAM results: (a) Heavy-ion cross-section fitted with a power law and (b) SEU cross-section calculation. Experimental data taken from [88].

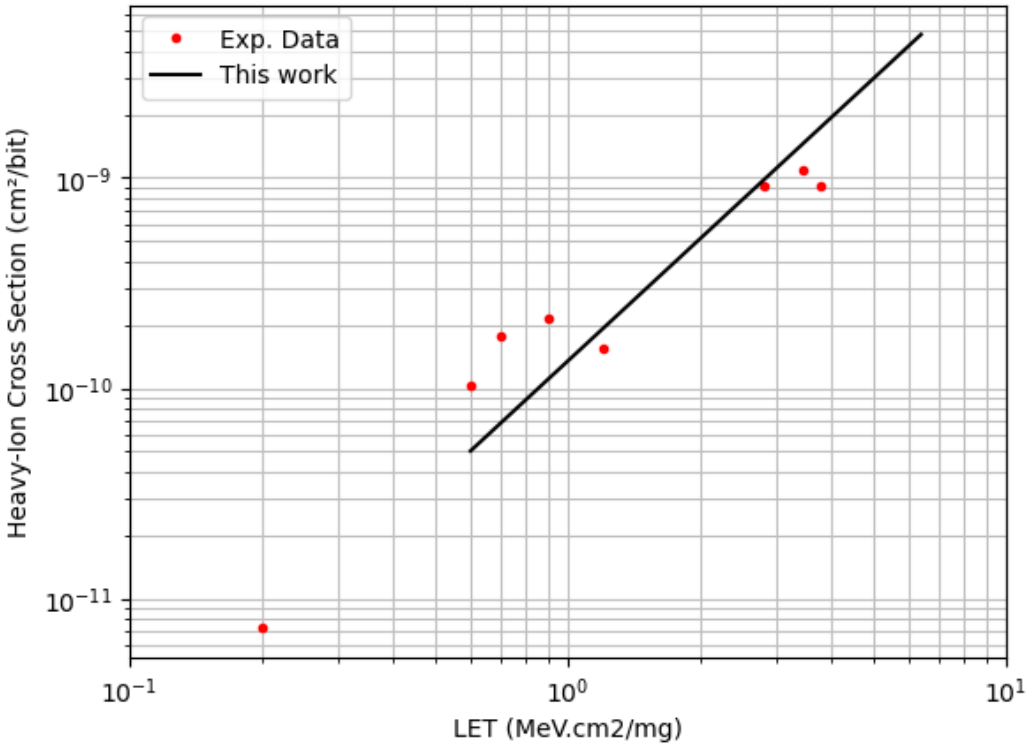

(a)

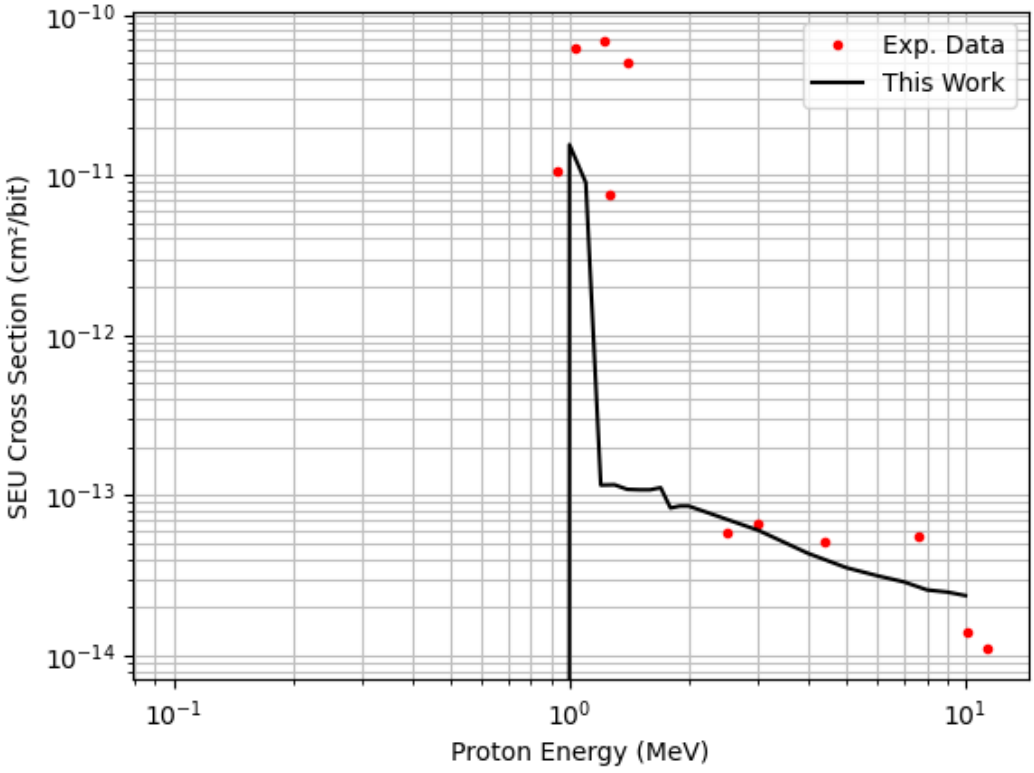

(b)

Figure 4.10: 65 nm SRAM results: (a) Heavy-ion cross-section fitted with a power law and (b) SEU cross-section calculation. Experimental data taken from [87].

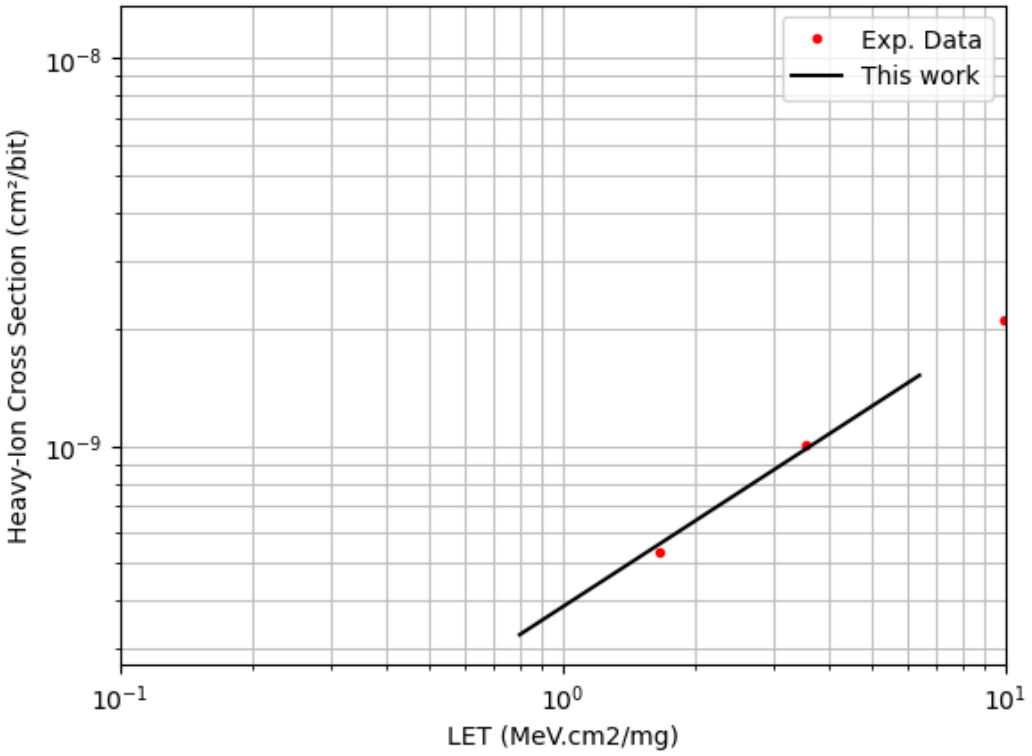

(a)

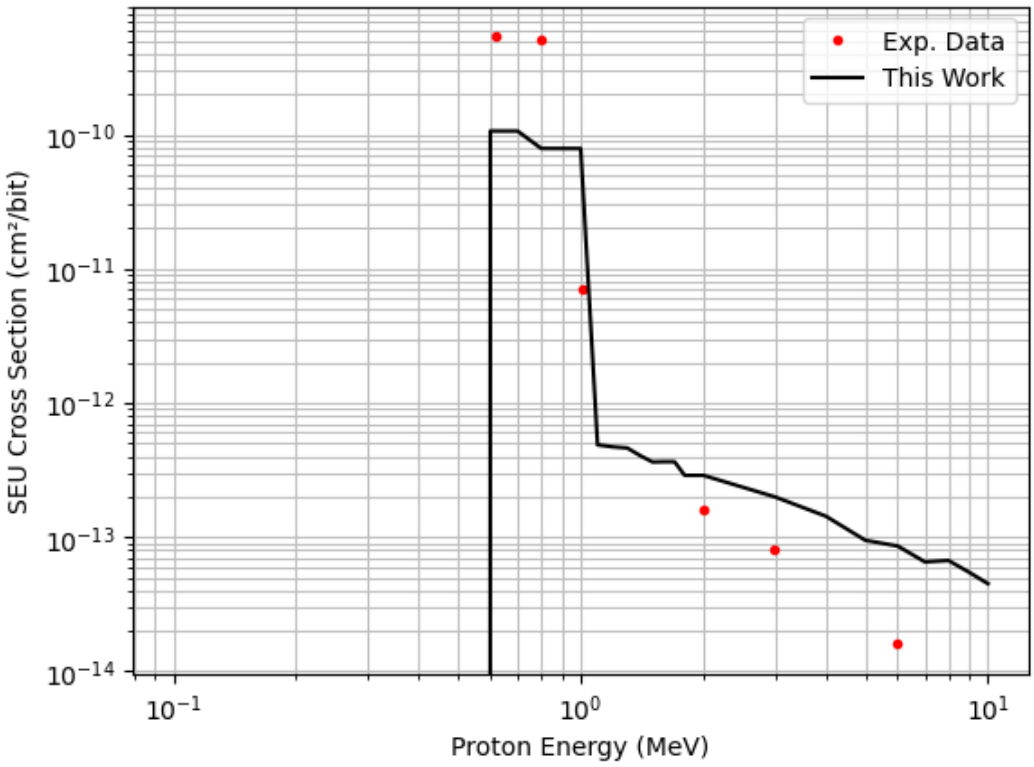

(b)

Figure 4.11: 40 nm SRAM results: (a) Heavy-ion cross-section fitted with a power law and (b) SEU cross-section calculation. Experimental data taken from [88].

4.4 Conclusions

This chapter highlights the importance of Coulomb elastic interactions on nuclei as a major source of SEE for protons in the 1–10 MeV energy range. A specific optical model to calculate the differential cross-section of proton interactions with a silicon nucleus was applied. Due to the divergence in the proton cross-section, a peak occurs that significantly impacts the LET distribution of ions reaching the sensitive region.

Using the proposed modeling approach with only four input parameters (BEOL layer thickness, sensitive region thickness, technology LET_{th}, and heavy-ion cross-section data), the SEE cross-section for incident protons was successfully computed. This approach avoids the extensive computational time required for direct Monte Carlo simulations. Results showed good agreement with experimental data in both shape and magnitude across various technological nodes. Divergences from experimental data are primarily due the simplifications, including approximations of dimensions and structural composition specific to each technology node. Nevertheless, the alignment provides valuable insights into the mechanisms that trigger SEEs.

For accurate SEE cross-section calculations for protons, the importance of accounting for Coulomb scattering must be emphasized, which can lead to significant recoil events, especially at low energies where the BEOL thickness cannot be ignored relative to the proton range. Primary proton energy loss is a critical factor, as it influences the energy distribution of secondary ions. Furthermore, using a simple step function for SEE cross-section calculations is insufficient. To obtain consistent results a power or Weibull fit based on heavy-ion experimental data is recommended. Results may vary depending on the availability of heavy-ion data, underscoring the importance of extensive experimental data for robust predictions.

Chapter 5

Heavy-Ions SEE predictions using Monte Carlo tool

Predictive and post-irradiation modeling is essential for understanding radiation effects of circuit and transistor levels. Monte Carlo (MC) simulations, such as SPENVIS [90], FLUKA [57], and G4SEE [51], are commonly used for this purpose. While FLUKA is a general-purpose MC tool, G4SEE focuses on SEE analysis, and SPENVIS addresses spacecraft dose calculation. Additionally, TIARA [91], MRED [92], and MUSCA SEP3 [47] are proprietary frameworks for SEE analysis. These tools typically rely on parameters from the technology's Process Design Kit (PDK), which includes essential information on process parameters, electrical characteristics, and layout rules. However, accessing these parameters is often challenging [59], and limited or unavailable data can lead to unreliable simulation results and longer computation times.

Given the importance of electrical models in assessing radiation sensitivity and the unavailability of such models from manufacturers, alternative modeling approaches are essential. This chapter introduces a simplified Monte Carlo methodology for SEE cross-section prediction that addresses the limitations of traditional models. This method, integrated into the PredicSEE tool developed at the University of Montpellier, offers a novel approach for calculating SEE cross-sections without extensive technological data and complex simulations. The methodology was validated against experimental data, identifying both its strengths and limitations.

5.1 Circuit modeling

Circuit modeling is crucial for assessing the performance and reliability of electronic systems before fabrication. In SEE analysis, circuit models help understand radiation-induced effects on electronics, supporting robust designs, shielding strategies, and evaluations of particle interactions for environments such as aerospace and accelerators [93, 94]. However, circuit modeling can be complex, as many physics-based SEE models extend CPU time due to their intricate representations of radiation interactions. While valuable, circuit-level modeling alone is often insufficient for comprehensive SEE analysis, necessitating complementary approaches.

5.1.1 Electrical model

An electrical model represents the behavior of a circuit, commonly through analytical or SPICE-based models. SPICE is a foundational tool in circuit modeling, representing component behaviors to analyze circuit performance under varied conditions. Predicting radiation effects, however, requires considerations of material properties and particle interactions [51, 52, 53]. While SPICE models can include hundreds of parameters, simplified approaches can often approximate behavior with limited inputs.

In this proposed approach, the transistor behavior is represented by simplified expressions for the drain-to-source current (I_{DS}) as a function of drain-to-source voltage (V_{DS}) and gate-to-source voltage (V_{GS}), approximating transistors with a current source [95]. To calculate the I_{DS}, we applied the simplest first-order model for the MOSFET transistor, which gives three major regions of operation: subthreshold, triode, and saturation. In this model the current through an OFF state transistor is 0. When the transistor turns ON, the gate attracts carriers to create the channel. The carriers drift from source to drain at a rate proportional to the electric field between these regions. The I_{DS} is a function of the gate capacitance (C_{Ox}), channel width (W), carrier mobility (μ_n for electrons and μ_p for holes), threshold voltage (V_{th}), channel length modulation (λ), and supply voltage (V_{dd}). The parameters at the base of these equations are known, at least in terms of their average values, for each technology node, as shown in Table 5.1. The C_{Ox} can be deduced from the oxide thickness (T_{ox}). For carrier mobility, normally, theoretical values based on the doping concentration of the technology are used. Considering the above parameters, the I_{DS} can be approximated by the following analytical expressions 5.1, 5.2, and 5.3 [95].

- Subthreshold if $V_{GS} < V_{th}$

$$I_{DS}(V_{GS}, V_{DS}) = 0 \tag{5.1}$$

- Triode if $V_{GS} \geq V_{th}$ and $V_{DS} < V_{GS} - V_{th}$

$$I_{DS}(V_{GS}, V_{DS}) = \mu C_{Ox}(\frac{W}{L})(1 + \lambda V_{DS})(V_{GS} - V_{th} - \frac{V_{DS}}{2})V_{DS} \tag{5.2}$$

- Saturation if $V_{GS} \geq V_{th}$ and $V_{DS} \geq V_{GS} - V_{th}$

$$I_{DS}(V_{GS}, V_{DS}) = \frac{\mu C_{Ox}}{2}(\frac{W}{L})(1 + \lambda V_{DS})(V_{GS} - V_{th})^2 \tag{5.3}$$

The advantages of the involved parameters are the number of inputs to be provided and the fact that we know their orders of magnitude for each technology node, as shown in Table 5.1. These parameters represent the minimum required to start our proposed methodology. The exact values of these parameters may not be precisely known for specific devices, but we will show that it is sufficient to feed our simulation tool with just the order of magnitude of the exact values.

Table 5.1: Simplified model; basic parameters for different technologies [95].

Node (nm)	Qcrit (fC)	Tox (nm)	W/L (nm/nm)	Vth (V)	Vdd (V)
90	1.2	2.0	180/90	0.40	1.0
65	0.8	1.8	120/65	0.42	1.2
45	0.6	1.8	90/45	0.46	1.0
32	0.4	1.6	64/32	0.63	1.0

5.1.2 SEE triggering model

SEE modeling is complex due to the intricate nature of radiation interactions with electronics, including ionization physics, charge collection processes, and particle–matter interactions [53]. The Monte Carlo (MC) approach is widely utilized for SEE analysis, where detailed characteristics of each incident particle are tracked, and specific criteria are applied to assess single- or multi-event fault occurrences. A common MC method is the rectangular parallelepiped (RPP) model [53, 77, 96], which defines the sensitive volume of the circuit as a simple box-like structure. Only radiation interactions within this volume that exceed the device's critical energy are considered, making the RPP approach a useful approximation. However, this simplified geometry may not capture the complex structure of certain devices accurately.

A more physics-based approach is the diffusion–collection model, which estimates the transient current shape generated in the drain of a sensitive transistor. This model considers two main charge transport mechanisms: drift and diffusion [52, 97]. Drift describes the movement of charge carriers under the influence of the electric field produced by the gate voltage, while diffusion results from carrier concentration gradients in the semiconductor, where carriers move from regions of high concentration to low concentration.

In the diffusion–collection model, spherical diffusion is assumed, as depicted in Figure 5.1a, which illustrates carriers reaching the OFF-state drain at a specific time and distance from the ion generation site. The model divides the ion track into segments, dl, each associated with an average LET (Linear Energy Transfer) value, as shown in Figure 5.1b. The density of electron–hole pairs reaching a specific area of the sensitive surface for each segment can then be calculated as follows:

$$n(t) = \int\int\int LET(l) \frac{e^{-\frac{r^2}{4Dt}}}{(4\pi Dt)^{\frac{3}{2}}} dxdydl \tag{5.4}$$

where D is the ambipolar diffusion constant.

Subsequently, due to the charge collection, a parasitic current will appear in the drain. The drain current, $I_d(t)$, can then be approximated as follows:

$$I_d(t) = \int\int_{drain} qn(t)vdS \tag{5.5}$$

where q is the elementary charge constant, v is the average velocity of the collected carriers, and dS is the drain surface element

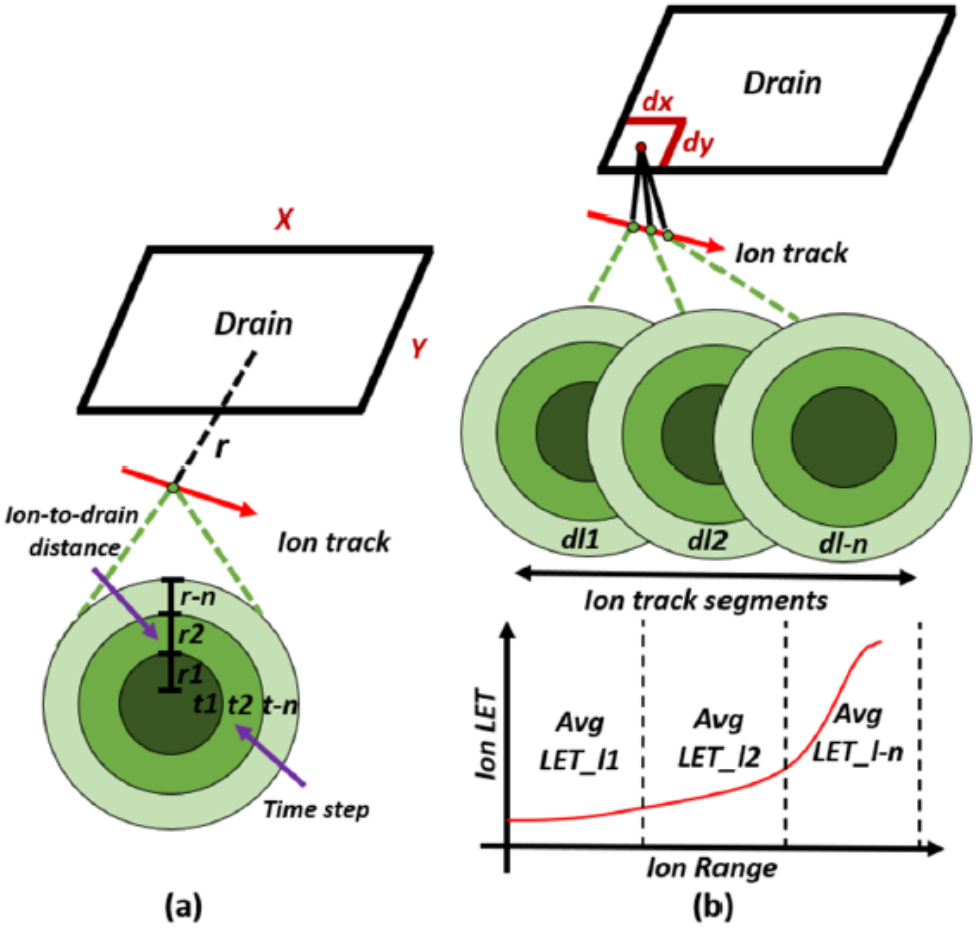

Figure 5.1: The diffusion–collection model: (a) the carriers arriving to the OFF-state drain at a given time t, and a given distance r, of the ion generation point; (b) segmentation of the ion track and the drain surface [97].

For ion tracks that pass through the sensitive region, a specific LET value is defined as the threshold required to trigger a fault. This threshold criterion has been validated in Correas et al. [52].

After calculating the transient current using Equations 5.4 and 5.5, this current can either be used directly in SPICE simulations or assessed via a criterion such as the $I_{MAX} - T_{MAX}$ criterion [52, 94, 97]. In the first approach, each particle interaction necessitates a new SPICE simulation, which can be computationally intensive due to the high number of particles in the MC pool. The $I_{MAX} - T_{MAX}$ criterion offers a more efficient alternative by focusing on the maximum transient current (I_{MAX}) and the time to reach this peak current (T_{MAX}), with these values typically determined through SPICE or TCAD simulations prior to the MC analysis [95]. Consequently, these approaches may not be satisfactory when a realistic PDK model is not available.

5.2 The proposed methodology

To address this limitation, we propose a method that differs from previous works [53, 95] by fitting the parameters in Equations 5.1, 5.2, and 5.3 using basic SPICE simulations. This allows us to obtain transistor characteristics in a simplified but realistic manner, without requiring direct access to proprietary PDK data. Our approach employs the Predictive Technology Model (PTM) [50] to separately characterize NMOS and PMOS transistors. The PTM provides a bridge between process/material development and circuit simulation through a compact device model designed to assess new technologies' potential and limitations in early design phases. Developed at Berkeley University, the PTM includes empirical values fitted from literature data and is based on standard formats such as BSIM4 [50].

In this approach, we perform basic SPICE simulations to generate I_{DS} vs. V_{DS} curves for various V_{GS} values. Using these curves as a reference, we can approximate the parameters in Equations 5.1, 5.2, and 5.3, bringing the behavior of the simplified transistor models closer to those provided by full SPICE models. This approach substantially reduces simulation time because subsequent analyses rely on the analytical equations of the simplified model. The SPICE simulations are only conducted initially to determine the parameters of the simplified model. Figure 5.2 shows an example of I_{DS} vs. V_{DS} curves generated using this simplified methodology for a 65 nm NMOS transistor.

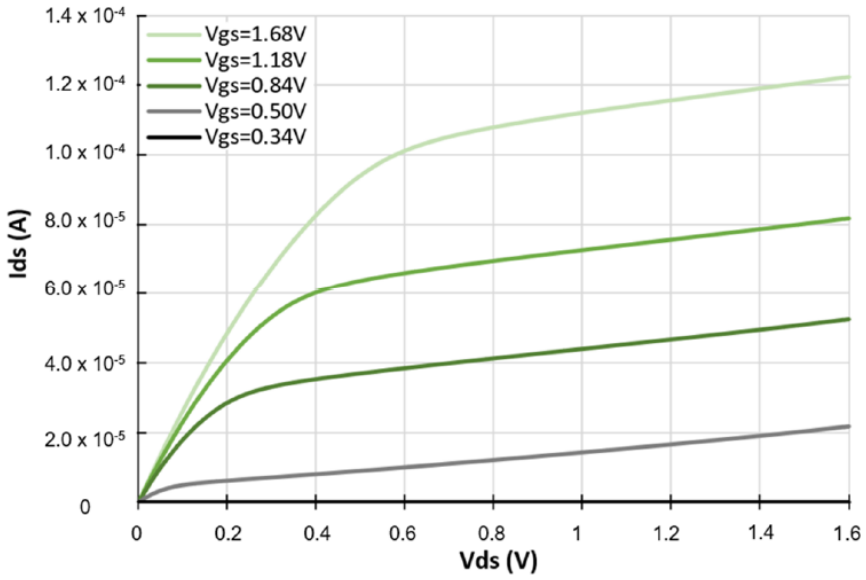

Figure 5.2: Example of the I_{DS} vs V_{DS} curves for different V_{GS} values of simplified NMOS transistor with the W/L = 1.

Using a 6T SRAM cell as example, the voltage variation at nodes Q and Q_b can be expressed as a function of six currents calculated via the diffusion-collection model: $I_{Q_{n1}}(t)$, $I_{Q_{n3}}(t)$, $I_{Q_{p1}}(t)$, $I_{Qb_{n2}}(t)$, $I_{Qb_{n4}}(t)$, and $I_{Qb_{p2}}(t)$. Additionally, six currents corresponding to transistor responses are estimated using the simplified transistor model: $I_{n1}(V_{GS}, V_{DS})$, $I_{n2}(V_{GS}, V_{DS})$, $I_{n3}(V_{GS}, V_{DS})$, $I_{n4}(V_{GS}, V_{DS})$, $I_{p1}(V_{GS}, V_{DS})$, and $I_{p2}(V_{GS},$

V_{DS}). The polarity of these currents is determined by the stored value in the cell. Equations 5.6 and 5.7 calculate the voltage for each node Q and Q_b, as illustrated in Figure 5.3, which shows the 6T SRAM cell schematic with node and transistor labels.

In contrast to previous approaches in literature [53, 95], this method accounts for all six transistors in the SRAM cell rather than just the four transistors in the two-inverter loop, improving simulation accuracy. Additionally, this approach incorporates the cell layout, enhancing the accuracy further. Equations 5.6 and 5.7 represent the voltage at nodes Q and Q_b, with input current polarity determined by the stored cell value:

$$C_N \frac{d(V_Q)}{dt} = I_{d_{n1}}(t) + I_{d_{n3}}(t) + I_{d_{p1}}(t) + I_{n1}(V_{GS}, V_{DS}) + I_{n3}(V_{GS}, V_{DS}) + I_{p1}(V_{GS}, V_{DS}) \tag{5.6}$$

$$C_N \frac{d(V_{Qb})}{dt} = I_{d_{n2}}(t) + I_{d_{n4}}(t) + I_{d_{p2}}(t) + I_{n2}(V_{GS}, V_{DS}) + I_{n4}(V_{GS}, V_{DS}) + I_{p2}(V_{GS}, V_{DS}) \tag{5.7}$$

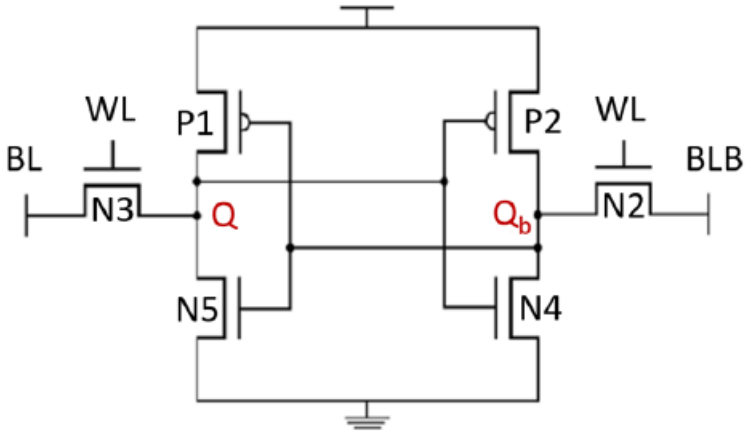

Figure 5.3: Standard 6T SRAM electrical diagram.

Solving these equations yields the transient voltage generated by the particle-induced current and determines the circuit's post-event state. This methodology is implemented in the PredicSEE tool, developed at the University of Montpellier. PredicSEE improves upon the previous tool, MC-Oracle [53], by offering a user-friendly interface and dynamically adjusting depletion layer thickness based on node potential. PredicSEE's Monte Carlo simulations inject particles randomly across the device area, with simulations ending once a stopping criterion (Monte Carlo accuracy or particle fluence) is met [98].

To reduce CPU dependency, PredicSEE incorporates the DHORIN database [67]. DHORIN pre-calculates a range of particle-matter interactions for protons and neutrons in the energy range of 1-200 MeV. For ions, primary and secondary ion transport and ionization are managed via SRIM [44] or Geant4 database. PredicSEE simulates the ionization effects of ions, neutrons, and protons using the diffusion-collection model,

which streamlines the carrier collection and transport processes following particle interactions. Figure 5.4 illustrates a flowchart of the PredicSEE code, detailing its workflow.

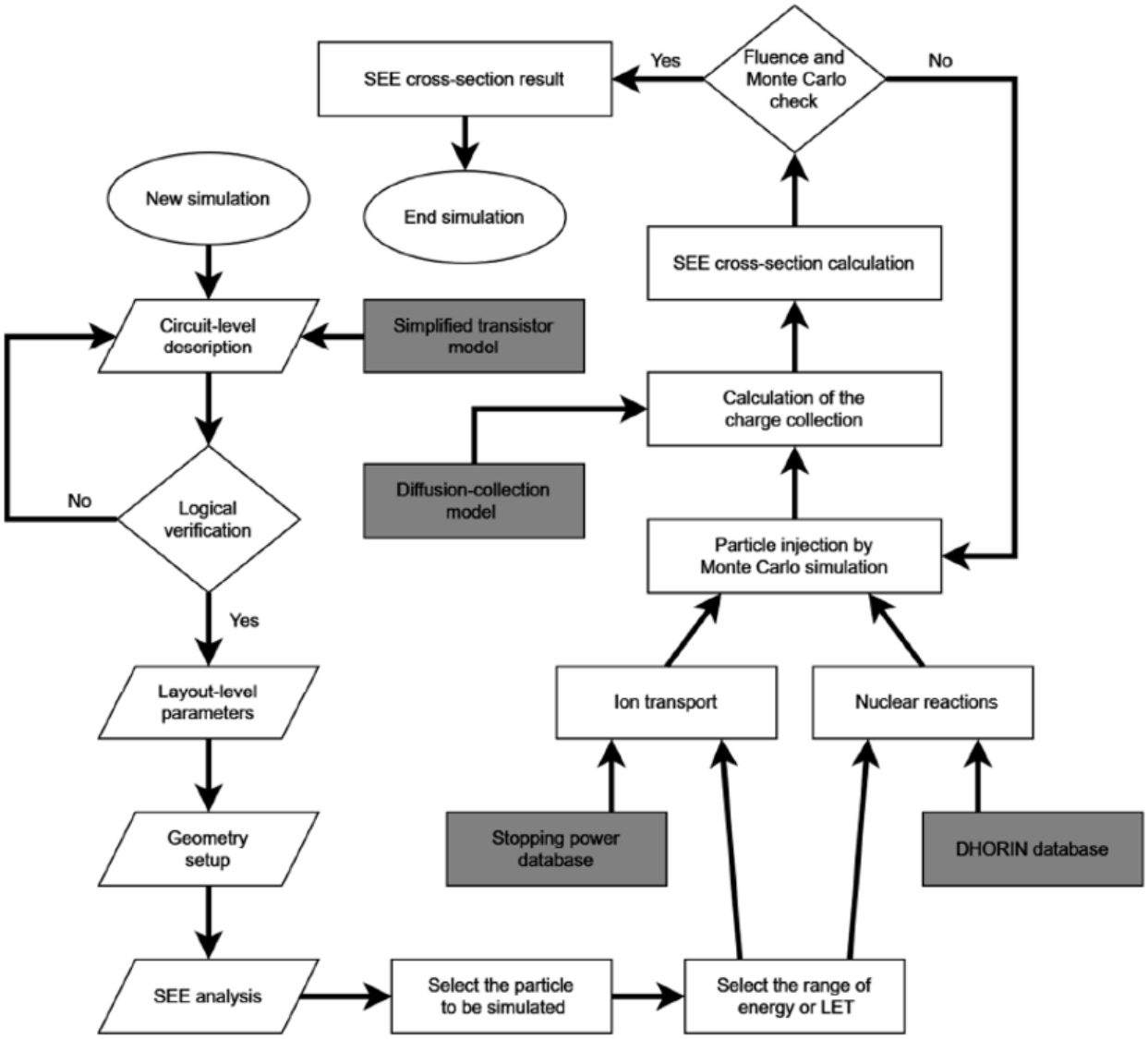

Figure 5.4: Simplified flowchart of PredicSEE code.

5.3 Simulation Setup

To validate this methodology, the 6T SRAM cell was evaluated across four technology nodes: 90 nm, 65 nm, 45 nm, and 32 nm planar-bulk CMOS. The analysis includes evaluating the heavy-ion cross-section, with the ion beam positioned perpendicular to the chip at a normal angle of 90°. Monte Carlo (MC) simulations were performed with a 95% confidence margin, and the results are compared to experimental data.

5.3.1 Circuit-level description

The initial simulation step is to describe the circuit schematic using PredicSEE. This involves defining transistors, wire connections, voltage sources, signals, and nodes capacitance. After describing the circuit, we specify the technology node through the Predictive Technology Model (PTM) reference. A SPICE model is generated to create a simplified transistor model, and we define the transistors' width (W) and length (L) ratios.

To choose these parameters effectively, it is essential to understand the 6T SRAM cell's operation. Cell access during write/read operations is controlled by the wordline (WL) signal. The access transistors ($N3$ and $N4$ in Figure 5.3) manage connections between the bitlines (BL and BLB) and the internal cell nodes (Q and Qb). Two PMOS transistors ($P1$ and $P2$) and two NMOS transistors ($N1$ and $N2$) form the feedback inverters.

Sizing the transistors in the cell is key to successful read and write operations. To optimize the read operation, the cell ratio (CR) is defined as $CR = (W_{N1}/L_{N1})/(W_{N3}/L_{N3})$, and for the write, the pull-up ratio (PR) is defined as $PR = (W_{P1}/L_{P1})/(W_{N3}/L_{N3})$ [99]. In this work, the design choices are $CR = 1.5$ and $PR = 1.0$. The minimum W/L used for each technology follows an approximate ratio of 2. This size and ratio are a standard choice to keep the cell area small, achieve good static and dynamic noise margins, and minimize the access times [99, 100]. However, it is essential to note that different values can be used depending on the cell design requirements. The others common technology parameters have already been presented in the Table 5.1. After describing the circuit, the tool performs a logical characterization to confirm that there are no implementation problems, such as impossible outputs or circuit shortcuts.

5.3.2 Layout-level parameters

The next phase involves defining layout parameters. PredicSEE generates a 2D geometry for each transistor, and the user arranges them according to layout rules of the specified technology node. Different layouts exist for 6T SRAM cells, each affecting factors like compatibility with address decoders, metal layers required, cell stability, bitline capacitance, and access times [99, 100]. Figure 5.5 shows three commonly referenced layouts [99, 101, 102].

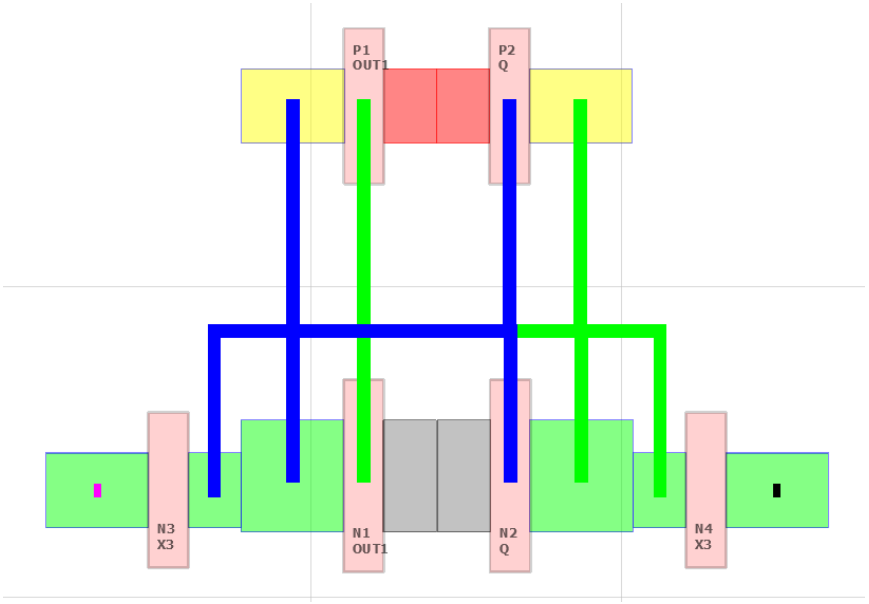

(a)

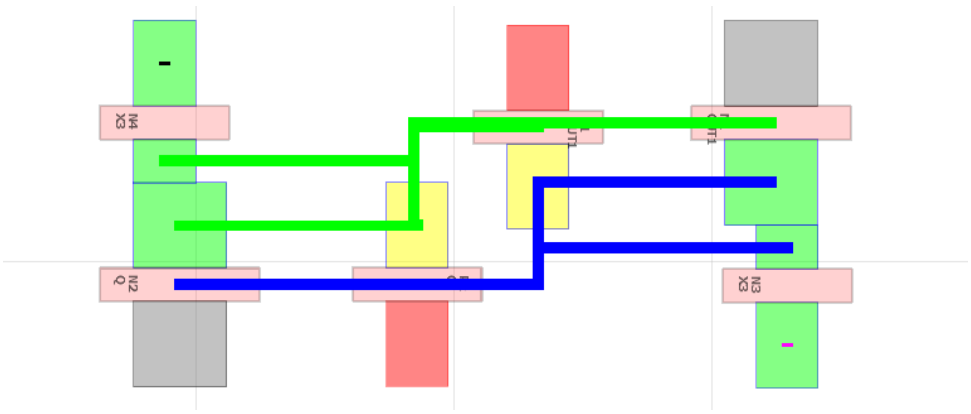

(b)

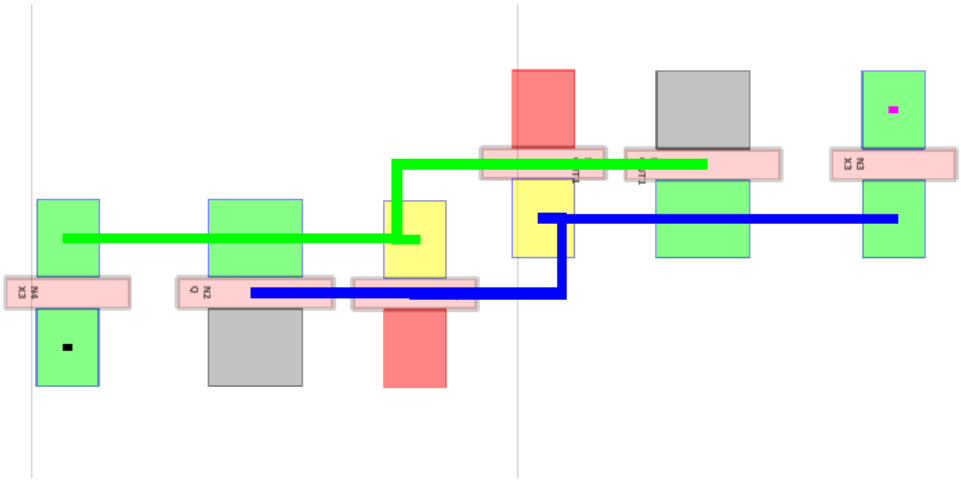

(c)

Figure 5.5: Three different layout designs that can be applied to 6T SRAM cell: (a) “tall” design [101]; (b) “thin” design [99]; (c) “ultra-thin" design [102].

The layout (a) is compact, widely used until the 90 nm generation, and is compatible with 65 nm design rules [101]. In layout (b) the diffusion areas work vertically, while the polysilicon tracks are strictly horizontal. The cell is longer and "thin", which reduces the critical capacitance related to the bitlines [99]. In layout (c) the cell is "ultra-thin", with lower bitline capacitance, reducing the metal layers' complexity, reducing the mismatch with the decoders, and adapting scaling/lithographic restrictions [102]. Due to limited information on commercial SRAM layouts, layout (b) was chosen as the reference. The layout rules adopted were collected in the literature [101, 103, 104, 105]. An additional essential input is the doping values for N+/P+ regions and N/P wells, as doping profiles strongly influence SEE sensitivity. The doping profile in this work was set approximately based on PTM values [50].

Another key parameter is the drain area, required by the diffusion-collection model. While precise measurements are often unavailable, we can estimate this area by assuming that the channel width corresponds to the drain width. Drawing rules generally specify that the drain length is approximately 2.5 times the channel length [95].

5.3.3 SEE analysis

The SEE analysis process involves two main stages: defining the geometry setup and setting the particle injection parameters.

The geometry setup modeling the device's structure for accurately simulating nuclear and ionizing interactions along the path of an incident particle. Given that the exact composition of the back-end-of-line (BEOL) is often unknown, we can use a simplified material composition with the following layers: An 8 μm silicon dioxide (SiO_2) layer, A 20 μm bulk silicon (Si) layer, and A 3 μm border region surrounding the device under test (DUT). Figure 5.6 illustrates a 3D visualization of the simulation setup, showing the material layers, DUT location, and particle beam angle.

For the particle injection, simulations were conducted using heavy-ion data from the Texas A&M Cyclotron Facility (TAMU) 15 MeV/u database and the RADiation Effects Facility (RADEF) 16.3 MeV/u database. The fluence was set to 1×10^{13} $ions/cm^2$ to accommodate low-LET ions in the analysis. For this lower LET range, a higher number of particle injections was required to ensure sufficient observable events. At high LET levels, however, the fluence does not reach this value since the simulation converges to Monte Carlo accuracy sooner.

During the simulations, selected particles are injected randomly within the total area, which includes both the layout area and the surrounding borders. The Monte Carlo process injects particles until either the fluence or accuracy criterion is met. For this study, only a single cell's surface was simulated, rather than a full SRAM array.

Upon completing the simulation, PredicSEE generates the SEE cross-section and provide a Weibul fit. This approach provides a precise and practical means of estimating the SEE cross-section across a range of LET values.

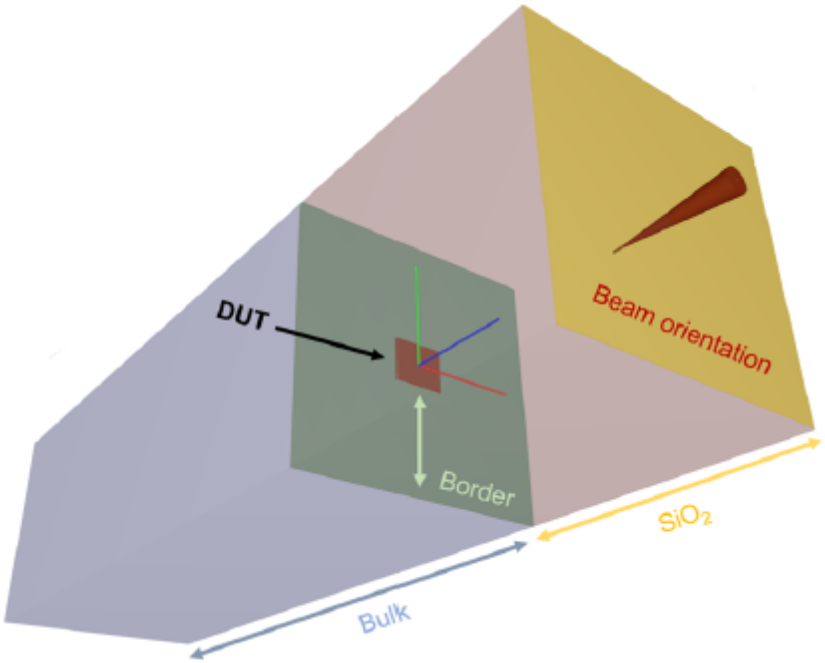

Figure 5.6: PredicSEE view of the simplified 3D structure used in the simulations. The BEOL is modeled with SiO_2.

5.4 Experimental data vs. simulation results

In this section, the SEU cross-section results are compared with the experimental data obtained in the literature [101, 106, 107, 108]. It is important to note that no fitting of the results was performed. The simulation setup are following the same characteristics of the experimental irradiation, using the same incidence angle and supply voltage. The simulation of one SRAM cell across 12 different LET values (using the TAMU heavy-ion cocktail of 15 MeV/u) took approximately 40 hours on a conventional laptop. Ions with LET values below 10 $MeV.cm^2/mg$ required more computation time due to lower event occurrences, while ions with LET values above this range required about 20 hours, as the simulation converged more rapidly to the desired Monte Carlo accuracy. By contrast, full SPICE modeling approaches often require several days of computation time [47, 94, 53], which can limit the analysis of complex circuit designs and design parameter variations.

Figure 5.7 shows the results for the 90 nm 6T SRAM. Despite lacking complete technology-specific transistor data, the simulation results aligned well with experimental data, showing an overall discrepancy of 20%. However, in the saturation region of the cross-section curve, the simulation underestimates the values by about 50%. This discrepancy is acceptable given the simplifications made in the modeling. The difference in the saturation region may stem from estimated layout structures, which could lack the precise dimensions of the 90 nm technology used in [106]. Experimental evidence indicates that SEU cross-sections are sensitive to specific circuit design features [109], a factor that could contribute to the observed discrepancies. This behavior is discussed further in Section 5.4.

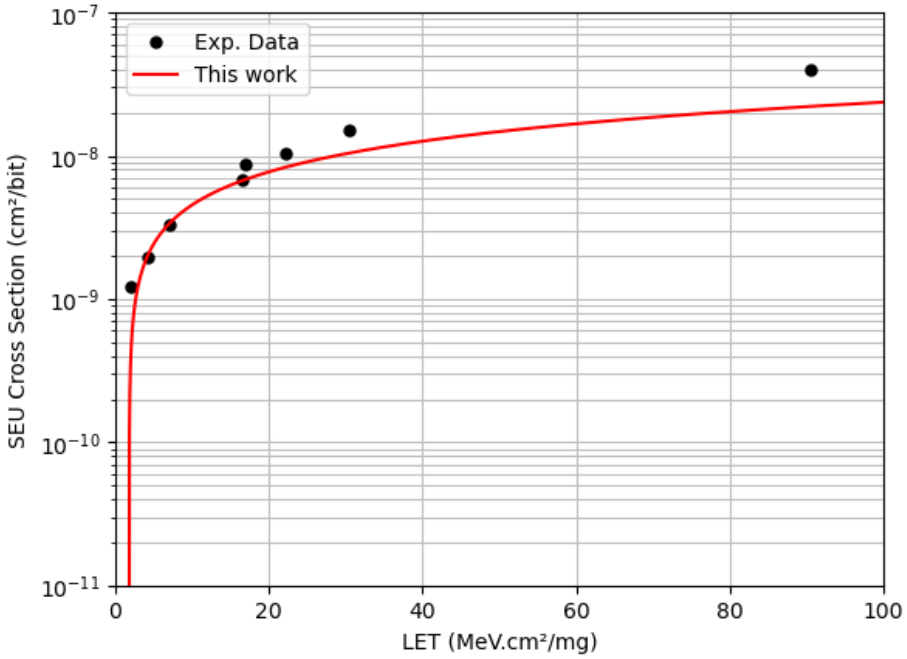

Figure 5.7: Heavy-ion SEU cross-section for 90 nm SRAM. Experimental data taken from [106].

For the 65 nm SRAM, the simulation results show better agreement with experimental data, with discrepancies under 15%, even in the saturation region, as seen in Figure 5.8. The largest discrepancies occur near the threshold LET region, where the simulation did not show upsets for LET values below 1.3 $MeV \cdot cm^2/mg$. This underestimation may result from approximations in the SiO_2 thickness in the BEOL layer and the doping profile, both of which were set with order-of-magnitude precision. These parameters influence LET accuracy in lower ranges, where fewer events are expected.

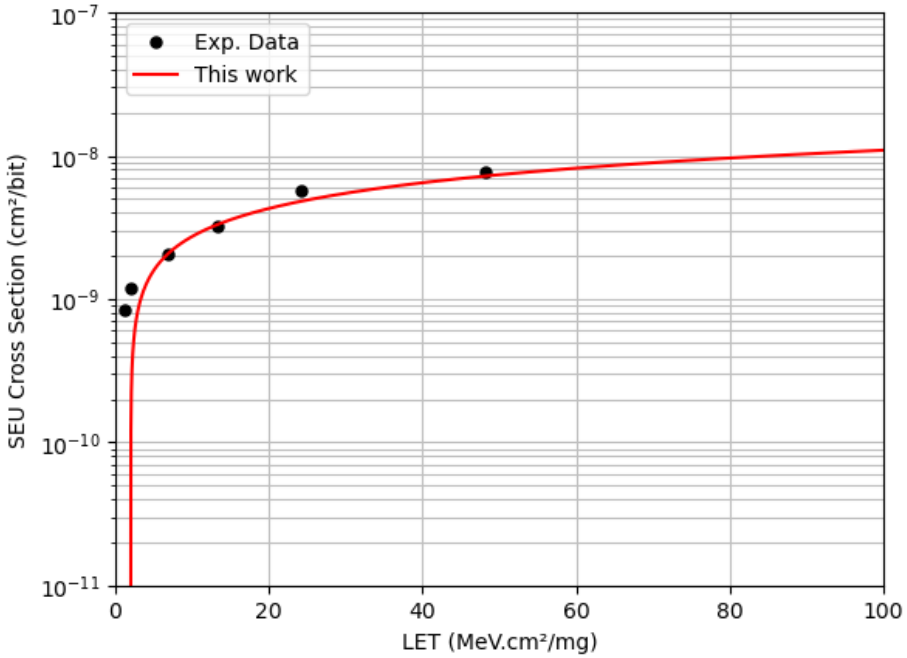

Figure 5.8: Heavy-ion SEU cross-section for 65 nm SRAM. Experimental data taken from [101].

For the 45 nm SRAM, simulation results show an even closer match to experimental data, with an average discrepancy of 10%, as shown in Figure 5.9. Minor overestimations occur at two data points near the LET_{TH} range, which can be attributed to similar factors affecting the 65 nm node, such as BEOL thickness and doping profile approximations. Improved parameter estimations at the 45 nm node helped enhance simulation accuracy.

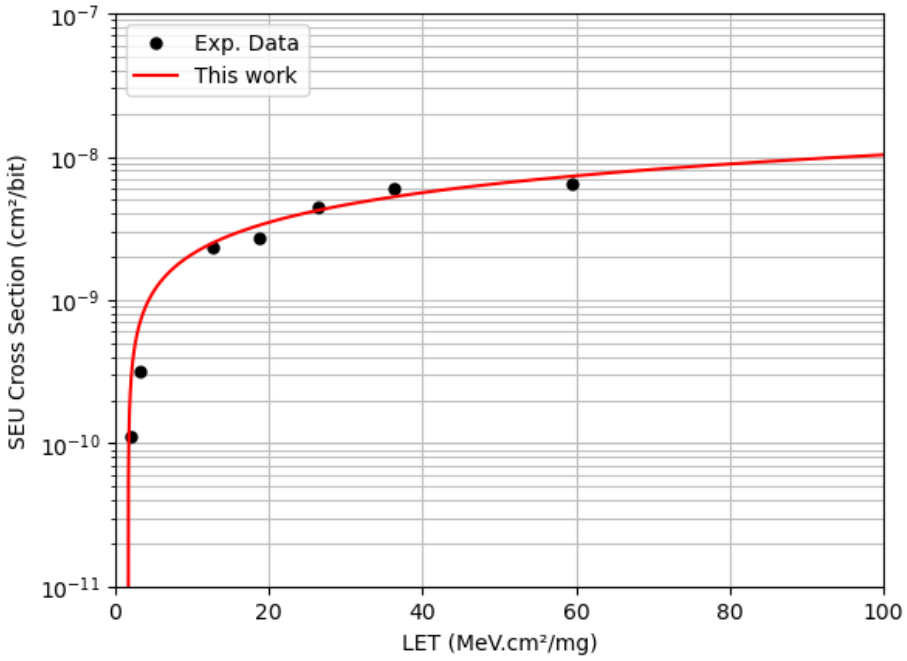

Figure 5.9: Heavy-ion SEU cross-section for 45 nm SRAM. Experimental data taken from [107].

A similar trend is observed for the 32 nm SRAM, where simulation accuracy decreases as particle LET decreases, as seen in Figure 5.10. While simulation results are of the same order of magnitude as the experimental reference data, the match is less precise. In the LET range of 1–20 $MeV \cdot cm^2/mg$, simulation results exhibit an average discrepancy factor of 3x. However, only a 10% difference was observed in the saturation region. For this node, circuit and layout information in the literature is sparse, and most available cross-section data is in arbitrary units, complicating direct comparisons.

To assess the model's robustness across different supply voltages, we gradually reduced the supply voltage from the nominal value of 1.2 V (see Table 5.1) to sub-threshold levels. For this analysis, we focused on the 6T SRAM cell at the 65 nm technology node, leveraging available experimental data for comparison. Figure 5.11 illustrates the SEU cross-section across five different voltage levels obtained from both simulation and experimental data.

The simplified model performed well in predicting the SEU cross-section at medium to high LET values, as long as the supply voltage remained above the transistor threshold (0.42 V, as indicated in Table 5.1). However, the simulation's accuracy decreased slightly near the threshold LET (LET_{th}) region. This deviation can be attributed to uncertainties in BEOL thickness and doping profile, as these parameters influence LET at lower levels, where fewer faults occur, affecting the accuracy of the LET_{th} calculation.

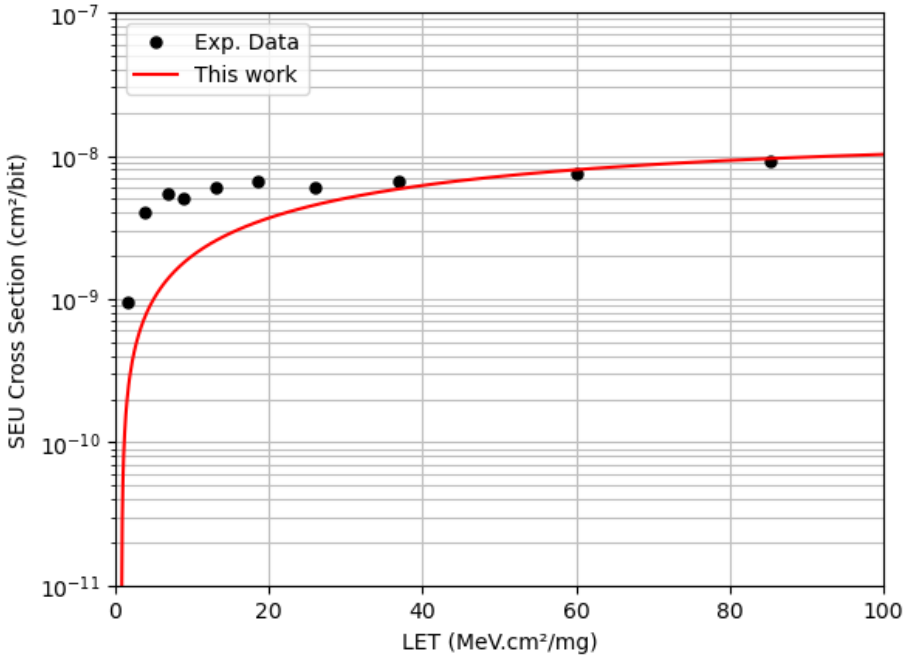

Figure 5.10: Heavy-ion SEU cross-section for 32 nm SRAM. Experimental data taken from [108].

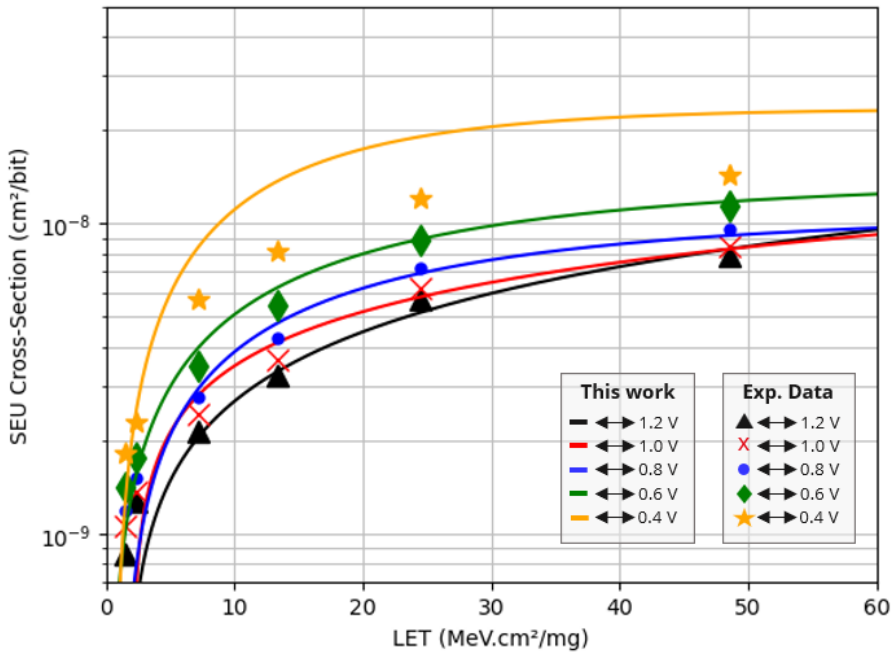

Figure 5.11: Heavy-ion SEU cross-section for 65nm SRAM considering the voltage scaling situation. Experimental data taken from [101].

A significant discrepancy emerged at sub-threshold voltage (0.4 V), where simulations tended to overestimate SEU cross-section compared to experimental data. This behavior suggests a limitation in the model's handling of sub-threshold regions, where transistor operation deviates from ideal conditions. Addressing this discrepancy will require further investigation into the model's performance at sub-threshold levels.

5.5 Impact of the input parameters

The proposed methodology has shown strong accuracy in predicting SEU behavior at medium-high LET levels above the transistor threshold voltage, demonstrating good alignment with experimental data. This section evaluates the effect of input parameter variations on the SEU cross-section, noting that our simplified model does not rely on parameter fitting. Instead, it uses approximate values derived from literature to predict cross-sections within an order of magnitude, even without full device-specific data. As device characteristics vary by manufacturer and application, it is essential to examine how different input parameters influence simulation results. Figure 5.12 compares the SEU cross-section for a 65 nm bulk CMOS 6T SRAM cell using the standard input parameters (the "golden" simulation) with variations in specific parameters.

- Cell ratio: in SRAM cells, the cell ratio (CR) generally varies from 1.0 to 2.5 in bulk CMOS technology, depending on the application [99]. Figure 5.12 compares results for the standard CR of 1.5 and an adjusted CR of 2.0. Increasing the CR led to a corresponding rise in the SEU cross-section. However, the variation remained within reasonable bounds, allowing users to safely estimate SEU cross-sections across typical CR values if precise data is unavailable.

- Layout variations: different layout configurations in SRAM cells can also impact SEU cross-section values. Figure 5.12 shows a comparison between the "Tall" layout used in the standard simulation and a "Thin" layout (see Figure 5.4), as well as a simulation where transistors are arbitrarily spaced without adhering to layout rules. While variations between layout approaches remain within acceptable margins, this is primarily valid for Single-Event Upsets (SEUs). For Multi-Cell Upsets (MCUs), layout configuration and neighboring cell proximity can affect the SEU cross-section due to potential charge-sharing effects between cells. Arbitrarily spaced transistors, however, yield substantially different SEU cross-sections, underscoring the importance of following a consistent layout structure for accurate SEU predictions.

- BEOL thickness: the BEOL thickness primarily influences SEU results at lower LET levels. When ions penetrate the BEOL, they lose energy, which affects event occurrence rates and statistical accuracy. Figure 5.12 compares simulations using the standard BEOL thickness of 8 μm and a reduced BEOL thickness of 3 μm. Minimal variation was observed for most of the curve, although simulations with a thinner BEOL required higher fluence levels to achieve Monte Carlo accuracy. This result indicates that minor BEOL thickness adjustments have a negligible impact on heavy-ion SEU cross-section, as small changes minimally affect ion energy, particularly at moderate to high energies.

- Doping profile: the doping profile of the N/P wells can vary significantly across manufacturers and lacks straightforward means of acquisition. For this study, we used approximate doping values based on predictive models and literature data. Figure 5.12 compares simulations with N-P WELL doping at 10^{18} atoms/cm^3 to

those with a reduced doping level of 10^{17} atoms/cm^3. Doping profile adjustments showed a substantial impact on SEU cross-section, highlighting that doping is the most critical input parameter for SEU sensitivity. End users should pay particular attention to accurate doping values whenever possible.

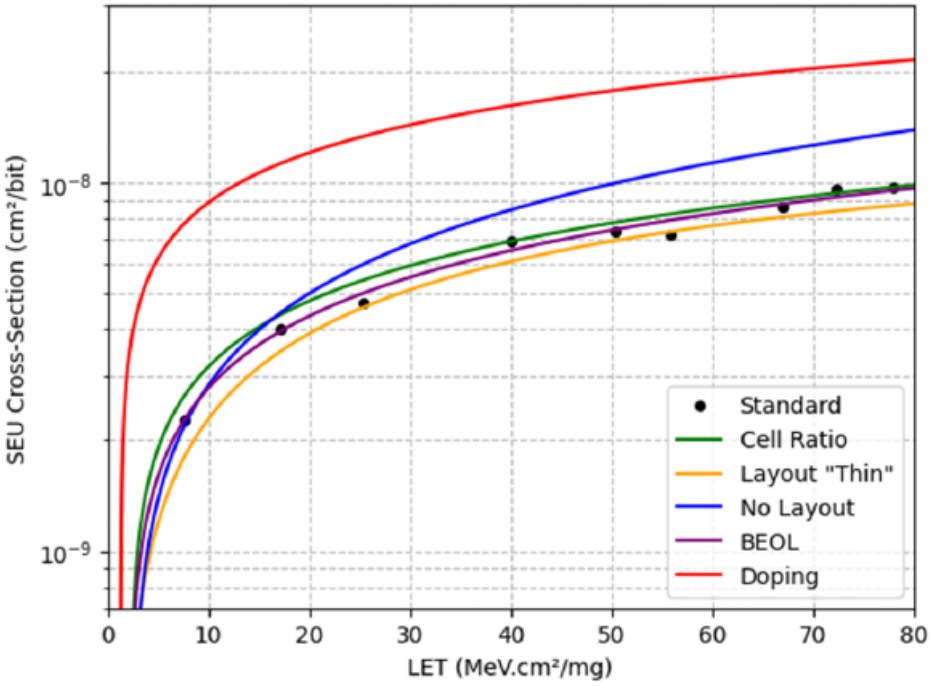

Figure 5.12: Heavy-ion SEU cross-section for 65 nm SRAM with variation in different input parameters. The standard plot is the golden result using the following input parameters: CR = 1.5, Layout = "Tall", BEOL = 8 μm, and Doping = $10^{18} atoms/cm^3$. For the other curves, we would only see one of the parameters and observe the simulation response. The cell ratio curve applies an CR = 2.0. The layout curve uses the "Thin" layout approach. The no layout curve does not follow a layout structure, just spacing the transistors for each other. The BEOL curve applies BEOL thickness of 3 μm. The doping curve uses the N-P WELL = $10^{17} atoms/cm^3$.

This parameter analysis confirms that while the proposed model provides reliable SEU predictions with approximate data, precise doping profiles are crucial for accurate SEU cross-section estimation. Minor variations in cell ratio, layout, and BEOL thickness have moderate to minimal impacts, allowing flexibility when exact data is unavailable.

5.6 Conclusions

This work presented a multi-physics framework that combines simplified electrical modeling with the diffusion-collection model and Monte Carlo simulations to calculate SEE cross-sections for heavy-ion-induced SEUs, utilizing the PredicSEE tool. The standard 6T SRAM cell served as the Device Under Test (DUT) for SEU evaluations across 90 nm, 65 nm, 45 nm, and 32 nm bulk CMOS technologies. The proposed approach demonstrated strong alignment between simulation results and experimental irradiation data, achieving this without simulation fitting or access to proprietary Process Design Kit

(PDK) data. The methodology successfully analyzed different technology nodes, voltage scaling, and a broad LET range for impinging particles, confirming its effectiveness in calculating SEU cross-sections for heavy-ion irradiation. Additionally, an assessment of input parameters provided insight into critical factors for end users to consider.

Most of the divergences found in the results can be improved by improving input data quality in the following fields: 1) The predictive SPICE models used to extract basic information from the technologies due to the general lack of actual industrial data; 2) The sizing of the SRAM cell transistors was standardized in a fixed ratio for the simulations, but it can vary a lot in commercial cells depending on the design requirements; 3) The design rules and doping profile used in the simulations in relation to the tested commercial cells, as there may be differences depending on manufacturers. It is important to note that the presented methodology is restricted to static analysis. To evaluate more complex circuits, it is necessary to consider different input vectors to obtain a more realistic SEE cross-section behavior.

This work evaluated bulk-planar CMOS technology, but the same methodology could be also applied to other technologies, such as Fully-Depleted Silicon On Insulator (FD-SOI) or Fin Field-Effect Transistor (FinFET). For this purpose, the challenge would be developing a charge-collection model compatible with these device structures.

Chapter 6

SEU cross-section estimation using 2D TCAD modeling

As discussed throughout this thesis, characterizing Single Event Upsets (SEUs) is essential for SRAMs used in radiation-prone environments, such as aerospace and safety-critical applications [110]. Typically, SEU cross-section, which represents the susceptible area of the Device Under Test (DUT), is determined experimentally by exposing the die to a high-energy particle beam. However, this experimental approach is complex, costly, and often infeasible for simulating specific radiation environments in ground-based facilities [111].

As outlined in Chapters 2 and 5, SEUs are widely simulated using Monte Carlo tools, which are highly effective for circuit-level analysis. At the device level, SEUs are also modeled extensively using Technology Computer-Aided Design (TCAD) tools [111, 112, 113]. TCAD simulations are employed to modeling the behavior of the semiconductor-based electronic components and their response to radiation, discretizing and solving different models. This involves solving Poisson's equation, which determines the electrostatic potential distribution in the device, and the continuity equations, which compute the spatial and temporal distributions of electrons and holes. By breaking the simulation domain into smaller finite elements, providing numerical solutions to these equations, enabling the analysis of carrier transport, electrical behavior, and physical phenomena within semiconductor structures. Despite the precision offered by TCAD, these simulations are highly complex due to the in-depth understanding needed of device structure and underlying physics. TCAD simulations frequently require 3D modeling, which increases the complexity and computational load, making them impractical for large circuit-level analysis.

Consequently, SPICE simulations are often combined with TCAD through a mixed-modeling approach. This hybrid technique accelerates the simulation process by using TCAD to model only the critical parts of the circuit, while the rest of the circuit is represented at a higher level of abstraction in SPICE. Both TCAD and SPICE modeling rely heavily on the Process Design Kit (PDK) for accurate simulation parameters, yet these detailed technological datasets are not always accessible.

In this context, this chapter proposes a methodology for estimating the SEU cross-section that overcomes the constraints associated with limited technological data and the high complexity of TCAD simulations. Using a standard 6T SRAM cell as the DUT, this method focuses on heavy-ion irradiation for 65 nm and 45 nm planar-bulk CMOS

technology. The primary objective is to deliver a practical 2D TCAD approach for estimating SEU cross-sections using only fundamental technological information commonly found in the literature.

Furthermore, this work provides an in-depth analysis of the parameters that most significantly affect 2D TCAD modeling, alongside strategies for estimating unknown values when technological information is sparse. The proposed methodology's accuracy is validated by comparing simulation results with actual experimental data, ensuring a robust and practical alternative for SEU cross-section estimation in the absence of detailed PDKs.

6.1 Proposed modeling

While SEU cross-section modeling often requires three-dimensional considerations, a 2D approach can simplify simulations, significantly reducing complexity and computation time. This study applies a mixed-modeling approach using the ECORCE TCAD tool [114]. ECORCE simplifies the modeling process by providing a user-friendly Graphical User Interface (GUI) for configuring all aspects of the simulation, including geometry setup, physical model selection, bias and irradiation conditions, and results analysis. To enhance accuracy and minimize calculation time, ECORCE dynamically adjusts the mesh at each simulation step. This feature ensures precise ion track descriptions and simulations, regardless of the impact point within the device. Notably, ECORCE does not assume a constant LET along the ion track. Instead, it uses the full LET profile, including the brag peak that provides a realistic representation of energy deposition.

For SPICE-based modeling inside of ECORCE, this work utilizes the open-access Predictive Technology Model (PTM) [50], which facilitates a streamlined transition from process and material characteristics to circuit-level simulations. Developed at Berkeley University using the BSIM4 model, PTM is designed to support early-stage design analysis through a compact device model.

6.1.1 TCAD modeling and parameters

In mixed-modeling simulations for SRAMs, the NMOS transistor is typically selected over the PMOS transistor due to its higher vulnerability to SEU effects. Figure 6.1 illustrates the simplified NMOS transistor structure implemented in ECORCE. Table 6.1 presents the parameters and their corresponding values utilized in the simulations. These parameters are essential for accurate modeling.

For planar-bulk CMOS technology, the transistor's channel length is generally associated with the technology node. However, actual values may vary with manufacturer, as design optimizations for performance or power efficiency can influence parameter selection. In this study, channel length values are based on PTM specifications. Other key parameters (such as oxide thickness, drain/source doping, and well doping) are also derived from PTM guidelines. The drain/source width is typically about 2.5 times the

channel length, as recommended in previous studies [95]. This configuration ensures an accurate representation of the NMOS device structure for SEU cross-section estimation.

Given the typically undisclosed composition of the Back-End-Of-Line ($BEOL$) layer, the modeling proposed here assuming an 8 μm thick silicon dioxide (SiO_2) layer. Although this approximation is not perfect, it serves as a practical solution for simulating the energy loss of impinging particles. The substrate is modeled using a 20 μm thick bulk silicon (Si) layer. Additionally, the transistor structure includes a 1 μm border width on both sides, which is essential for calculating the SEU cross-section based on the particle impact position. A narrower border could affect the SEU cross-section calculation by potentially overlooking faults occurring near the device's edges, while increasing the border width would require a higher number of particle injections. This will increase the accuracy, but also the simulation time. After testing border widths ranging from 0.5 μm to 3 μm, we found that 1 μm provided a good trade-off for this analysis. The substrate doping is fixed at 6×10^{16} cm^{-3}, which optimizes transistor performance.

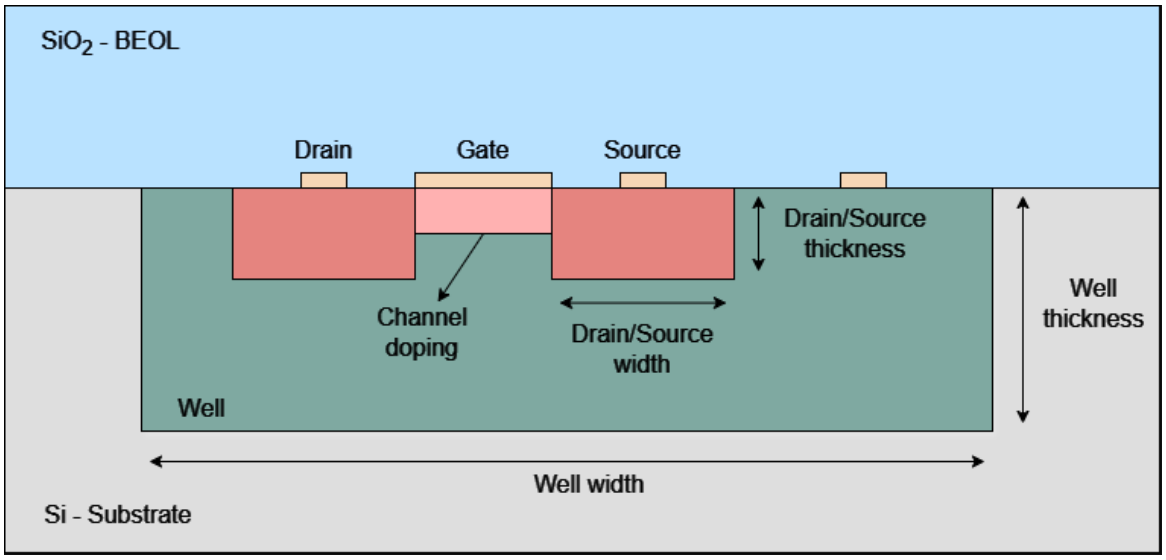

Figure 6.1: Structure of the 2D TCAD bulk-planar transistor implemented on ECORCE.

Conversely, specifying certain parameters, such as the thicknesses of the doping regions and the channel doping value, poses a more intricate challenge. In this work, the parameter values that ensure transistor characteristics consistent with SPICE simulations were selected. The values used are presented in Table 6.1, and further details regarding these choices are discussed in Section 6.3.

The NMOS transistor was simulated in ECORCE with a mesh precision of 3 nm, utilizing approximately 4,500 mesh nodes. Electrical characterization required about 11 minutes using four cores of a standard commercial processor. Figure 6.2 illustrates the analysis of the drain current (I_{drain}) versus the gate voltage (V_{gate}) for a transistor in 65 nm technology, comparing the results with those from the predictive SPICE model. The leakage current, threshold voltage, and saturation current show close correspondence between the two simulation methods. However, minor discrepancies in the curve shape are present, which may be attributed to the different physical laws accounted for in the ECORCE simulation compared to the simplified ones in the SPICE predictive model.

Furthermore, the higher sloop of the spice curve probably is induced by interface states already existing in the component before irradiation and that have not been define for this TCAD model.

Table 6.1: TCAD parameters for different technology nodes [50, 95]

Parameter	Technology node	
	65 nm	45 nm
Oxide thickness	1.2 nm	1.0 nm
Channel width	65 nm	45 nm
Drain/Source doping	$2.00 \times 10^{22} cm^3$	$2.00 \times 10^{22} cm^3$
Well doping	$2.54 \times 10^{18} cm^3$	$3.40 \times 10^{18} cm^3$
Drain/Source width	0.1625 μm	0.125 μm
BEOL thickness	8 μm	8 μm
Substrate thickness	20 μm	20 μm
Border width	1 μm	1 μm
Substrate doping	$6.00 \times 10^{16} cm^3$	$6.00 \times 10^{16} cm^3$
Drain/Source thickness	0.040 μm	0.030 μm
Well thickness	0.5 μm	0.5 μm
Channel doping	$2.50 \times 10^{18} cm^3$	$2.95 \times 10^{18} cm^3$

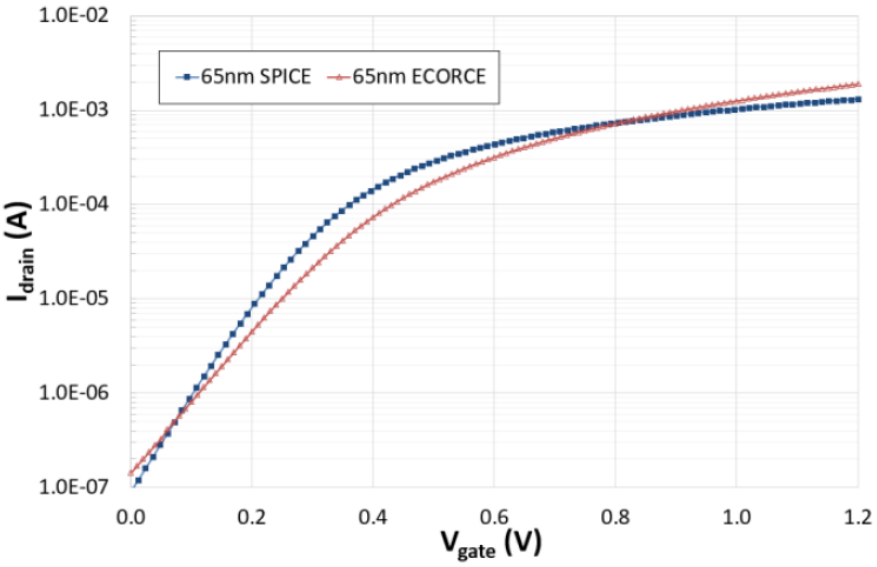

Figure 6.2: The I_{drain} vs V_{gate} curve of the NMOS transistor for 65 nm modeling.

6.1.2 SPICE implementation

The SPICE model is used to simulate the remaining five transistors of the 6T SRAM cell. For this, it is necessary to define each transistor's width (W) to length (L) ratio. Proper sizing of transistors in the cell is crucial for ensuring reliable read and write operations. To optimize the read operation, the cell ratio (CR) is expressed as $CR = (W_{N1}/L_{N1})/(W_{N3}/L_{N3})$, while for the write operation, the pull-up ratio (PR) is defined

as $PR = (W_{P1}/L_{P1})/(W_{N3}/L_{N3})$ [99]. In this work, the design choices include a cell ratio of 1.5 and a pull-up ratio of 1.0. The minimum W/L used for each technology follows an approximate ratio of 2, representing a standard choice that balances cell area and access time, while providing good static and dynamic noise margins [99]. This configuration offers a practical trade-off between cell area efficiency and performance. However, it is essential to note that these values can be adjusted to meet specific design requirements, allowing flexibility based on performance, power, or area constraints.

6.1.3 SEU cross-section calculation

In recent years, various simulation approaches have been developed to evaluate the SEU cross-section, many of which offer high accuracy but at a considerable computational cost. In this proposed methodology, the emphasis is on a simplified approach with targeted ion injections along the x-axis, maintaining a precise spacing of 0.1 μm between each injection. Given the dimensions of a 65 nm transistor, for example, this approach requires only 29 injections per ion to evaluate its impact on the transistor. This study analyzes the effects of six different ions, selected from the RADiation Effects Facility (RADEF) heavy ions 16.3 MeV/u database to ensure a wide range of scenarios is covered. Figure 6.3 illustrates the methodology used to calculate the SEU cross-section.

In the first step, for each injection we check the SEU occurrence (Red points in Figure 6.3(a)). With this, we can calculate the sensitivity along the x-axis, denoted as B_x. It is important to note that since we chose a 0.1 μm step between each injection, there is some uncertainty in this range. To take this into account, a margin of error of 0.05 μm (half of the step) was added. Next, we calculate the sensitive region extending to the drain, referred to as b_x. By adding the transistor width (W, which is 0.18 μm for the 65 nm node and 0.09 μm for the 45 nm node) with twice the value of b_x, we obtain the sensitive region along the z-axis, denoted as B_z. Equation 6.1 show this calculation. The following step involves calculating the initial area, which in this study, is approximated as a rectangular geometric area (see Figure 6.3(b)). Multiplying B_x by B_z yields the SEU cross-section for the NMOS transistor.

$$Bz = 2(bx) + W \tag{6.1}$$

In an SRAM cell, bit storage relies on a pair of inverters in a feedback loop configuration, meaning that one NMOS transistor and one PMOS transistor are always in the OFF-state simultaneously. To incorporate the effect of the PMOS transistor without requiring an additional simulation, we account for the cell ratio between the NMOS and PMOS transistors. With a chosen cell ratio of 1.5, we divide the calculated SEU cross-section for the NMOS by this 1.5. The result of this calculation is added to the cross-section calculated for the NMOS to obtain the total SEU cross-section for the SRAM cell.

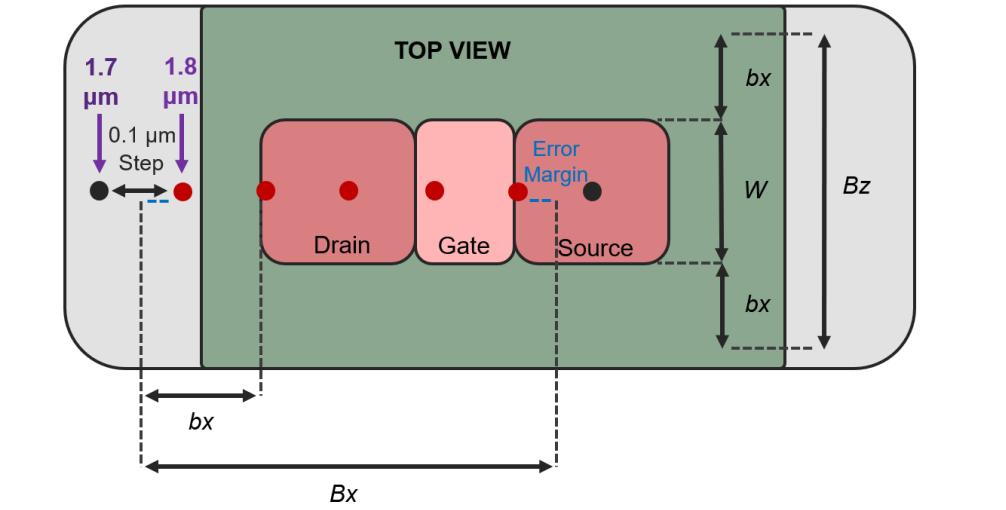

(a)

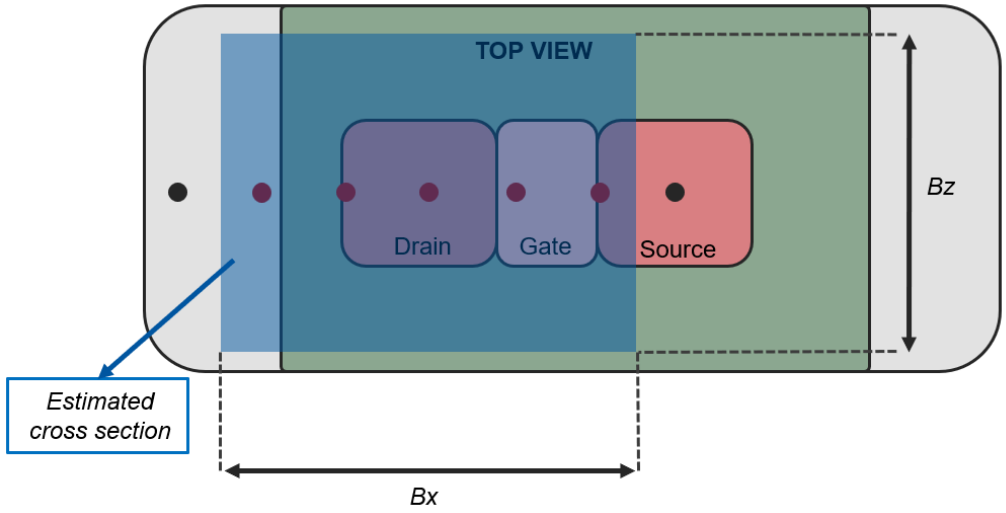

(b)

Figure 6.3: Transistor SEU cross-section estimation methodology: (a) x-axis injection and (b) area estimation.

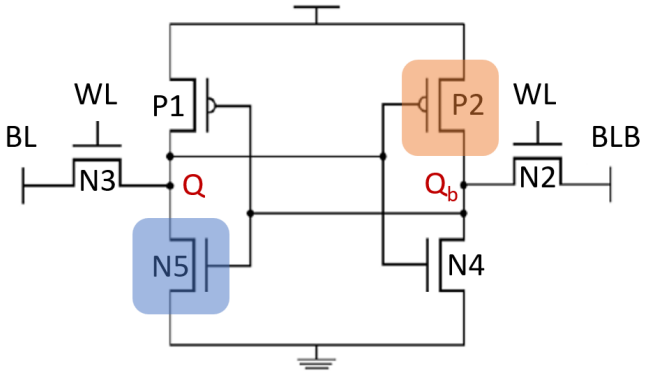

Figure 6.4: Total SEU cross-section of the cell. Blue rectangular area is the NMOS SEU cross-section, while the orange area is estimated by the cell ratio (CR=1.5).

6.2 Experimental data validation

In this section, the estimated SEU cross-section of a 6T SRAM cell under heavy-ion irradiation was compare with experimental data from the literature [101, 107]. We also included a comparison with PredicSEE tool methodology presented in the Chapter 5. Based on TCAD simulation results, a Weibull curve is generated to fit the calculated data points, with an error margin of 1×10^{-10} cm^2/bit.

For the 65 nm SRAM, results are shown in Figure 6.5, which demonstrate a good agreement between simulation and experimental data for medium-high LET values. However, a divergence is observed in the threshold LET (LET_{th}) region, where our simulations did not capture upsets at 1.3 MeV.cm^2/mg, and our result for 2.3 MeV.cm^2/mg slightly underestimates the cross-section. This discrepancy can be attributed to simplifications made in modeling the SiO_2 thickness in the BEOL layer, the well doping, and the substrate doping. When ions pass through the BEOL, they lose energy, which impacts carrier generation. At low LET values, where the ion-induced voltage peak is close to the transistor's threshold, minor variations in carrier generation can significantly influence cross-section. Additionally, a notable error bar is seen at 2.3 MeV.cm^2/mg due to the 0.1 μm step size used in ion injection.

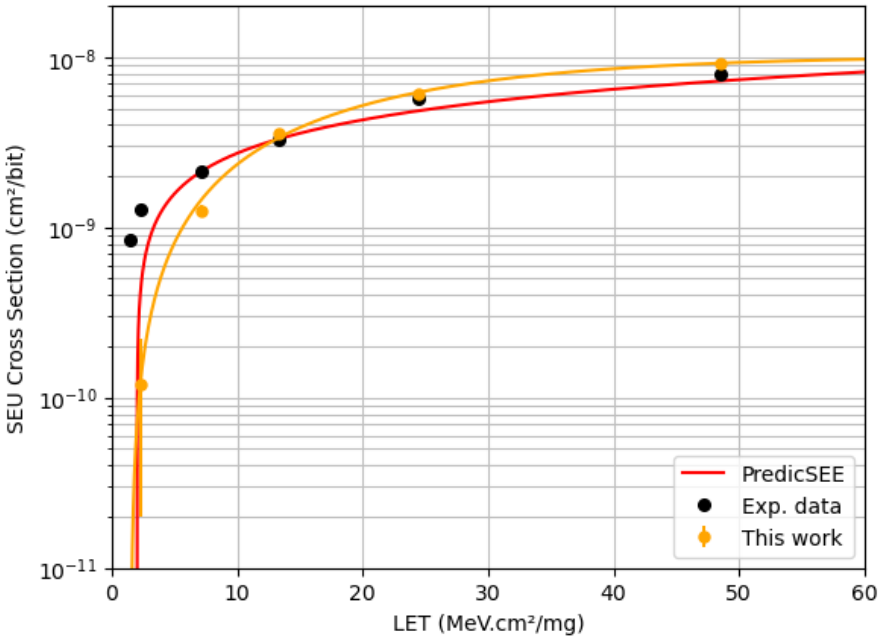

Figure 6.5: Heavy-ion SEU cross-section for 65 nm SRAM. Experimental data taken from [101].

The SEU cross-section estimation for the 45 nm SRAM shows even better agreement between simulation and experimental results, as illustrated in Figure 6.6. Both the threshold LET and saturation regions align well with experimental data, and the predictive SPICE model proves more accurate for this technology node. As a result, parameter approximations in the model have a more positive impact on simulation accuracy, highlighting the methodology's viability, especially when SPICE model parameters closely match the actual device characteristics.

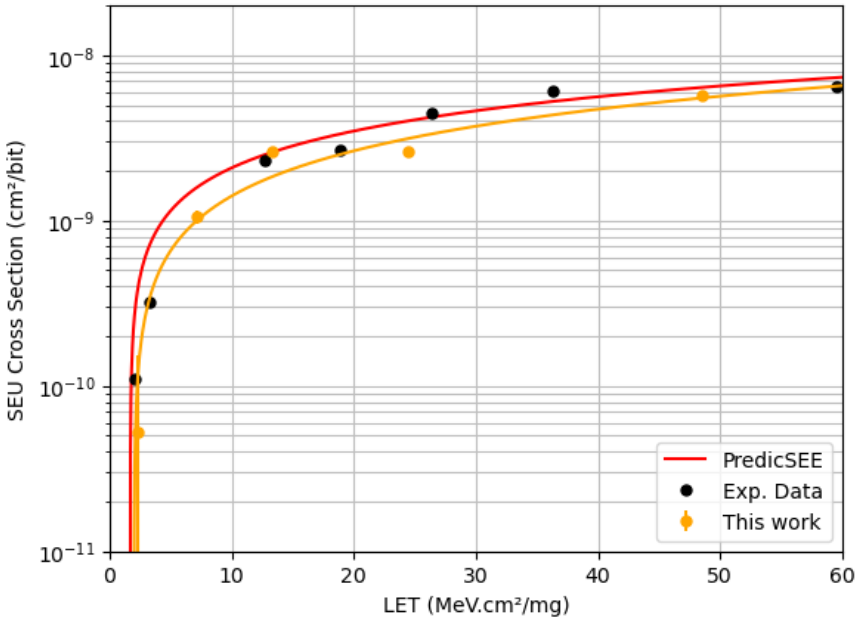

Figure 6.6: Heavy-ion SEU cross-section for 45 nm SRAM. Experimental data taken from [107].

The proposed methodology provides an excellent solution for predicting SEU cross-section at medium-high LET values and standard supply voltages. Despite a slight accuracy reduction in the LET_{th} region for the 65 nm node, these results are impressively accurate considering the significant approximations made at both the circuit and device levels. No fitting adjustments were applied to enhance SEU cross-section results. Another significant advantage is the reduced simulation time: typically, simulating a single ion's impact on an SRAM cell can take days depending on the TCAD setup [115], whereas our approach yields complete results across a range of LET values in approximately 15 hours.

When we compare this results with the values obtained using the PredicSEE, we can observe a consistent result. Both approaches provide a similar Weibull curve. However there is a difference in the sloop of the curve. PredicSEE shows a better agreement in the LET_{th} region. These two approaches present different methods for estimating the SEU cross-section, requiring further research to understand which factors impact this difference. One point to be highlighted is that in the TCAD analysis the cell layout and the proximity of their transistors are not considered.

6.3 Influence of different TCAD parameters on the accuracy

This novel methodology aims to simplify the challenges associated with limited technological information and the complexity of running TCAD simulations. By identifying key parameters with a substantial impact on simulation outcomes, users can prioritize these critical parameters over others with minimal influence. This work has identified five essential parameters, not defined by SPICE models, which are crucial to the analysis: well thickness, well width, drain/source thickness, substrate doping value, and channel doping value.

- **Well thickness:** this parameter is pre-set at 0.5 μm in our model, as variations from 0.25 μm to 2.0 μm **show minimal effects on the SEU cross-section**. Although increasing well thickness can improve charge collection by enlarging the active region, it can also reduce the carrier mobility due to the additional doping, increasing recombination rates.

- **Well width:** similar to well thickness, well width affects the SEU cross-section by **influencing charge collection efficiency and carrier mobility**. Adequate mesh granularity around the drain/source regions is essential to prevent inaccuracies in charge transport calculations. We maintain a minimum clearance of 50 nm between the well and the drain/source areas to ensure simulation precision.

- **Substrate doping value:** we set the substrate doping at 6×10^{16} cm^{-3} for all simulations to optimize transistor performance. Increasing this value to 1×10^{17} cm^{-3} affects fault detection at 2.3 MeV.cm^2/mg and increases leakage current, **impacting SEU cross-section calculations for low-LET particles** by raising the LET threshold and reducing charge collection.

- **Drain/Source thickness: this parameter directly affects leakage current**. To achieve optimal control, the drain/source thickness should be equal to or less than the channel width. For our simulations, we use a thickness of 40 nm for a 65 nm channel and 30 nm for a 45 nm channel.

- **Channel doping value:** The channel doping value is selected based on benchmarks from the SPICE model, and **it should be lower than the well doping**. This parameter is crucial for optimizing transistor characterization as it impacts in the leakage current, threshold voltage, and saturation current.

6.4 conclusions

The proposed simplified methodology for estimating SEU cross-sections demonstrated a strong correlation with actual irradiation data, though they do not perfectly match. However, these results are achieved without complex implementation or manufacturers PDK data. By utilizing only academic and predictive models, the proposed approach accurately estimated the SEU cross-section for two different technology nodes and a broad LET range of impinging particles. These results confirm that this approach is both efficient and effective to estimate SEU cross-sections for heavy-ion irradiation.

This study focused exclusively on bulk-planar CMOS technologies, necessitating further validation to extend its applicability to other advanced technologies, such as Fully-Depleted Silicon On Insulator (FDSOI) and Fin Field-Effect Transistor (FinFET) structures. Additionally, our approach emphasized performance gains by limiting the simulations to 2D modeling. Nevertheless, a comparable methodology could be adapted to include 3D simulations, potentially enhancing the accuracy of SEU cross-section estimations by capturing three-dimensional effects in device structures.

Chapter 7

Modeling SiC Schottky diodes susceptibility for SEB

Wide bandgap semiconductors, such as silicon carbide (SiC) power devices, have gained significant interest for use in harsh environments, particularly space, due to their superior electrical and thermal properties compared to traditional silicon-based devices [116, 117]. With a critical electric field strength approximately 10 times higher than silicon, SiC enables a voltage-blocking layer (n-epitaxial layer) that is about 10 times thinner, with a significantly higher donor density for the same breakdown voltage. This characteristic pushes beyond the limitations of Si-based power electronics, enabling devices to operate efficiently in high-temperature, high-power, and high-frequency environments.

Despite these advantages, the vulnerability of SiC Schottky barrier diodes (SBDs) to heavy ions has become a significant concern due to Single Event Burnout (SEB) and large leakage current after irradiation. Several studies have investigated these failure mechanisms, but the explanations remain controversial. S. Kuboyama et al. [118] was the first one to identify the thermal runaway process as a mechanism responsible for the susceptibility of SiC SBDs to heavy ions. A. Javanainen et al. [119] suggested that the damage was induced by high temperatures exceeding the melting point of SiC (3100 K) at the Schottky contact, resulting from enhanced current flow along the ion track attributable to impact ionization. A. Akturk et al. [120] reported that SEB in SiC power devices arises from impact ionization and fast thermal transients, which is completely different from the conduction of parasitic bipolar transistors in silicon power devices. C. Martinella et al. [121] attributed the degradation in leakage current to ion-induced, highly localized energy pulses in SiC power MOSFETs and junction barrier Schottky (JBS) diodes. Finally, C. Peng [122] indicated that heavy ion incidence raises the lattice temperature within SiC devices, with higher bias voltages leading to melting.

These studies highlight the critical role of temperature increases in the degradation of SiC devices. At high biases, temperatures can reach SiC's melting point during irradiation. Even at lower biases, however, temperature increase can damage the Schottky junction due to the lower melting point of the Schottky metal contact, leading to the formation of leakage current pathways [119, 120, 121, 122]. Building on this understanding, significant advancements have been made in recognizing SiC's susceptibility to heavy ion-induced degradation as a critical issue. However, the fundamental mechanisms driving this phenomenon remain inadequately characterized and insufficiently explained. This study addresses this gap by demonstrating that SiC's high critical

electric field, a key advantage of these devices, is also the primary factor behind their susceptibility to heavy ion irradiation. Using TCAD simulations, this work models these physical mechanisms and compares the behavior of SiC and silicon SBDs.

7.1 Schottky diode modeling

Schottky diodes typically have a similar layout. Devices consist of a metal-semiconductor contact (anode) made of platinum, gold, aluminum, titanium or nickel, and an n-type substrate [123]. Figure 7.1 illustrates the structure of these devices. The cylindrical or 3D geometry is essential for electrical and thermal coupled simulations, as it enables axial-symmetric charge deposition along the ion track and supports the quantitative analysis of radial heat flow from the track. Modern SiC SBDs have a structure called Junction Barrier Schottky (JBS), where p+ regions are placed periodically at the contact to reduce the thermionic emission current under reverse bias conditions. However, their sensitivity is experimentally demonstrated to be similar to the structure showed in Figure 7.1 [122].

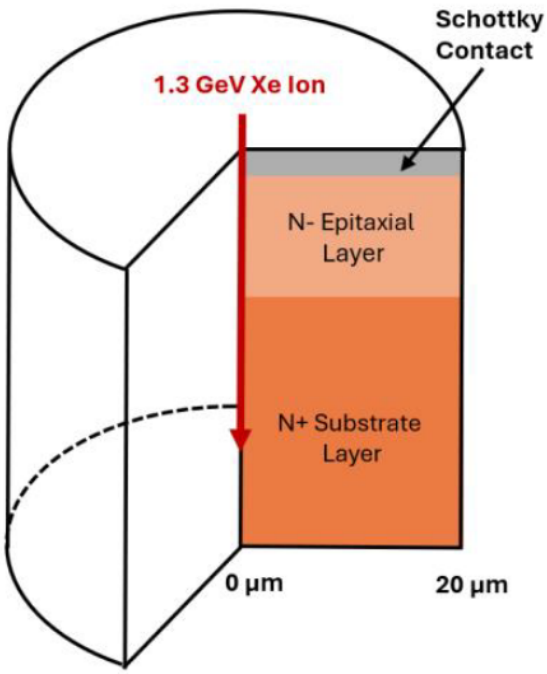

Figure 7.1: Cylindrical geometry and structure of the SBD used for simulations.

The ECORCE tool was employed to model the Schottky diodes [114]. ECORCE TCAD tool integrates a drift-diffusion model with the heat equation, enabling thermodynamic simulations that incorporate lattice temperature. This tool also accounts for a realistic LET profile during ion injection, rather than assuming a constant LET. Additionally, ECORCE features a dynamic mesh generator that optimizes mesh distribution at each modeling step, ensuring a high-quality grid that is independent of the TCAD user. These capabilities are crucial for understanding the underlying mechanisms while

maintaining efficient use of computational resources. To our knowledge, the dynamic mesh capability is only available in ECORCE. Furthermore, ECORCE provides state-of-the-art material models for SiC, making it particularly well-suited for investigating the underlying mechanisms while maintaining computational efficiency.

The electrical and thermal models applied in this study align with those used in prior research [124, 125, 126, 127, 128], as summarized in Table 7.1. Key material parameters, including bandgap energy, effective density of states, and intrinsic carrier density, were derived from the energy band structure of the crystalline material [125]. While these models were not explicitly developed for the extreme temperatures near SiC's melting point, considering that they are modeled by simple functions of temperature, they can then be easily extrapolated.

For mobility parameters, which are crucial in device simulations for accurately predicting the device's electrical behavior, we employed thermodynamic equations incorporating Joule heating effects. In this context, the interaction between carrier temperature and phonons linked to lattice temperature is considered negligible. Instead, the equation parameters are expressed directly as functions of lattice temperature.

This approach and models have already been validated in previous works [124]. It is important to note that the models have physics basis, and must produce values that prevent convergence problems or mathematical issues, generating physically plausible results for meaningful analysis.

The primary aim of this work is to identify the main physical mechanisms responsible for heavy ion-induced degradation in SiC and explain why this degradation is less severe in Si-based devices. To achieve this, Si and SiC SBDs were modeled with parameters listed in Table 7.1. These parameters were selected to produce electric fields in the epi layer near the lower limit of the critical electric field under nominal bias conditions: -600 V for the SiC diode and -200 V for the Si diode. The differences in parameters between Si and SiC reflect the commercial advantages of SiC, including thinner epi layers and higher doping values [116, 117]. To ensure realistic comparisons, the parameters were based on values used in industry and available literature [124, 128, 129]. However, for further clarity, both devices were also evaluated under identical conditions to isolate behavioral differences.

The response of the diodes under ion irradiation was analyzed using a 1.3 GeV Xe ion, widely used in experimental facilities due to its high LET. The ion range, LET profile, and ion track model followed the framework proposed in [124], accounting for variations in stopping power between Si and SiC. For SiC, the initial LET was 61.54 $MeV.cm^2/mg$ with a range of 64.4 μm, whereas for Si, the initial LET was 58.93 $MeV.cm^2/mg$ with a range of 94.5 µm. These differences reflect the distinct interactions between the ion and each material, further highlighting the unique vulnerabilities of SiC.

Table 7.1: Electrical and Thermal models for SiC [124, 125, 126, 127, 128]

Parameter	**Equation**	**Unit**	Remarks
Bandgap energy [125]	$E_g(T) = 3.27 - 6.5 \times 10^{-4}(\frac{T^2}{T+1300})$	eV	Negative at T > 6100 K. Modified to be saturated at T > 5000 K with a value of 0.8 eV
Effective density of states in the conduction band [125].	$N_e(T) = 3.25 \times 10^{15}(T^{1.5})$	cm^{-3}	
Effective density of states in the valence band [125].	$N_v(T) = 4.8 \times 10^{15}(T^{1.5})$	cm^{-3}	
Intrinsic carrier density [125].	$N_i(T) = \sqrt{N_c N_v}\exp(-\frac{E_g}{2kT})$	cm^{-3}	Calculated from 3 parameters given above.
Thermal conductivity [125].	$K(T) = \frac{611}{T-115}$	$\frac{W}{cmK}$	Values for 6H-SiC are usually used. Experimental data available up to 2300 K
Electron mobility	See reference [126].		Experimental data available up to 800 K.
Hole mobility	See reference [130].		Experimental data available up to 580 K.
Field dependence of mobility	See reference [127].		Experimental data available up to 730 K for electrons. The same applied for holes.
Impact ionization	See reference [128].		More details in the section 7.3.1.

Table 7.2: Parameters for Si and SiC SBD structures.

Parameter		Si	SiC
n- epitaxial layer	thickness (μm)	12.0	3.7
	doping (cm^{-3})	1×10^{15}	1×10^{16}
n+ substrate layer	thickness (μm)	108.0	116.3
	doping (cm^{-3})	1×10^{19}	1×10^{19}

7.2 Main mechanism of thermal runaway

During ion impact, electron-hole pairs are generated along the ion track, as illustrated in 7.2. Initially, the electric charge remains neutral along the ion path. However, under the influence of the electric field applied in the epi layer, electrons (e-) and holes (h+) are driven in opposite directions. As a result, a positive charge accumulates near the Schottky contact. So, electrons are pushed deeper into the device volume while holes cross the Schottky contact at a speed determined by the recombination rates (2.57×10^6 cm/s for electrons and 1.93×10^6 cm/s for holes). This charge separation amplifies the electric field near the Schottky contact while simultaneously reducing it in the epi layer (Figure 7.3).

When the local electric field reaches the critical threshold, impact ionization is triggered, producing additional electron-hole pairs near the Schottky contact (Figure 7.4). This process results in a localized increase in temperature, eventually reaching a burnout point. Over time, an equilibrium is established between the electric field and the enhanced electrical conductivity generated by the additional electron-hole pairs near the contact. The electric field stabilizes in this state, persisting until all ion-generated carriers are either collected or recombined.

Figure 7.5 compares the properties of 4H-SiC with those of traditional Si devices [131, 132]. A key distinction between SiC and Si Schottky diodes lies in the electric field at which impact ionization is triggered. For the SiC Schottky diode, impact ionization begins at an electric field of 3 MV/cm, whereas for the Si diode, it is triggered at 0.3 MV/cm. This represents a 10 times factor in the critical electric field values.

In practical operation, the electric field within the diode typically exceeds this critical threshold, as equilibrium between the electric field and the electrical conductivity is achieved near the Schottky contact. The resulting power heat density (W_j) caused by the Joule effect is defined as the product of the electric field (E) and the current density (J). Given that J is directly proportional to E, the power heat density scales approximately with E^2. Consequently, the power heat density near the Schottky contact in SiC diodes is approximately 100 times higher than in Si diodes. This significant difference underscores the elevated thermal and electrical stresses experienced by SiC devices under high electric fields.

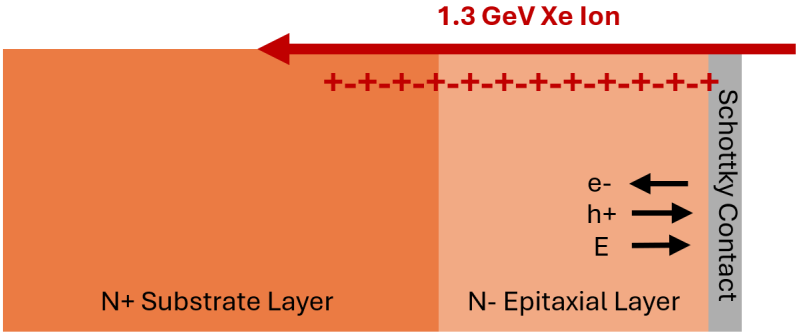

Figure 7.2: First step: generation of electron-hole pairs and displacement of charges depending on the electric field ($t = 0$).

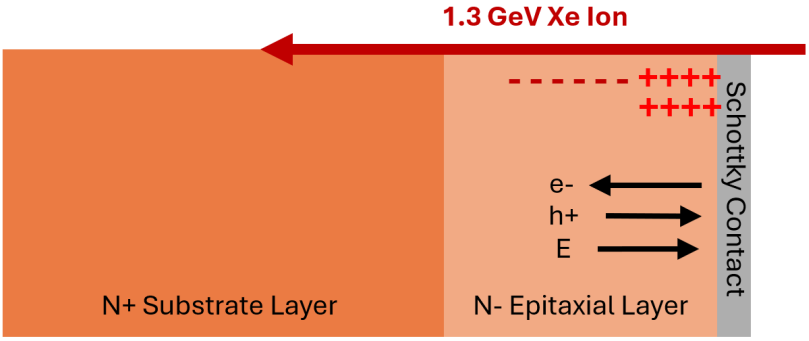

Figure 7.3: Second step: charges are separated by the electric field, a high positive charge appears at the contact. The electric field in the epi layer is reduced, while the electric field increases near the Schottky contact. It speeds up the pair separation at this point.

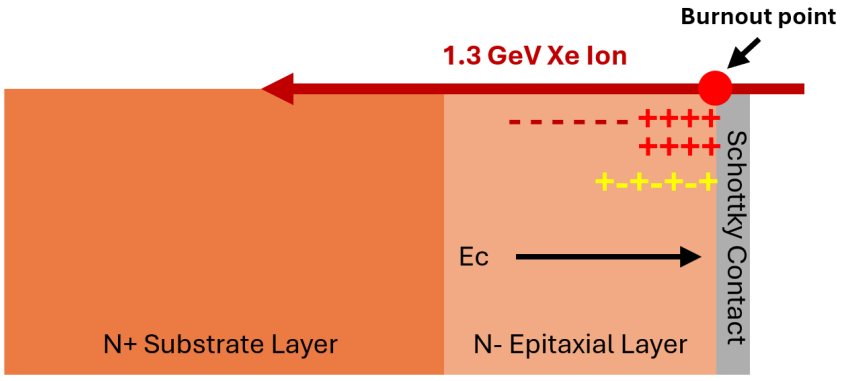

Figure 7.4: Third step: the impact ionization is triggered. Additional pairs are generated by impact ionization (yellow). The electric field is limited when the impact ionization rate is high enough.

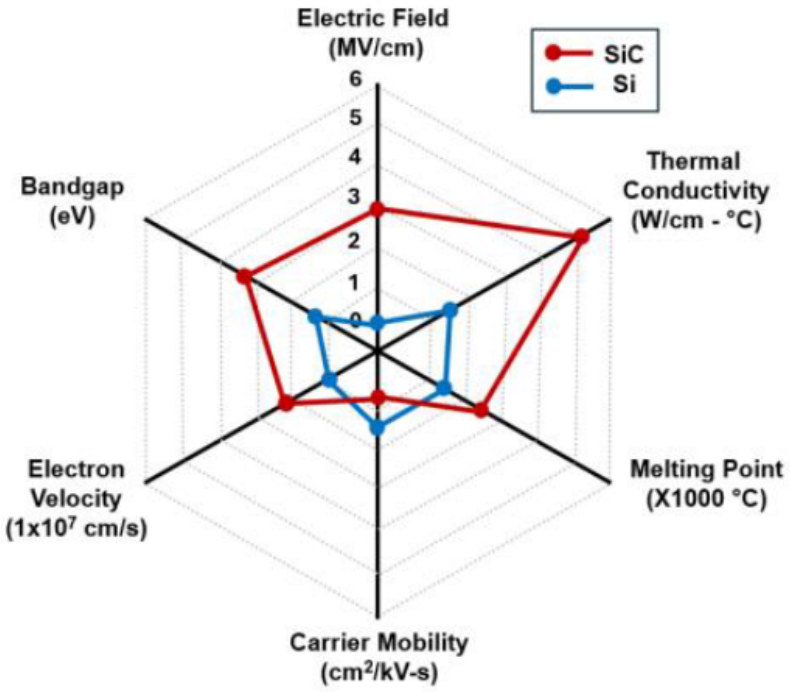

Figure 7.5: Chart to compare the Si and SiC properties [133].

7.3 TCAD modeling results

This section presents the modeling results comparing the behavior of SiC and Si Schottky diodes under heavy ion irradiation, focusing on the key physical mechanisms responsible for device degradation.

7.3.1 Impact ionization modeling

In order to effectively apply the main mechanisms presented in the previous section, it is important to understand how the impact ionization on Si and SiC was modeled. Y. Okuto [134] highlighted that, for Si, the ionization coefficients are functions of electric field strength, position within the junction and temperature. Based on this, we can calculate the impact ionization by Equation 7.1:

$$a = a_{300}[1 + c(T - 300)]\epsilon \exp - \frac{b_{300}[1 + d(T - 300)]^2}{\epsilon} \tag{7.1}$$

where T is the temperature in kelvin and ε is the modulus of the electric field. The a_{300}, b_{300}, c, and d are constants listed in Table 7.3 a_{300} and b_{300} are fitted based on 300 K of temperature.

The ratio of ionization as a function of the electrical field strength obtained using the expression (1) for Si presented a very good agreement ($\approx 4\%$ of error) with experimental results for most commercial devices evaluated in [134].

For SiC devices, T. Hatakeyama [128] shows that the ionization coefficients need also to include the doping density of the diode layers. Then the impact ionization can be modeled by:

$$\alpha = a\gamma \exp\left(-\frac{b\gamma}{F}\right) \tag{7.2}$$

$$\gamma = \frac{\tanh \frac{\hbar\omega_{op}}{2k_B T_0}}{\tanh \frac{\hbar\omega_{op}}{2k_B T}} \tag{7.3}$$

where F represents the magnitude of the electric field. $\hbar\omega_{op}$ is the optical phonon energy and can be extracted by fitting the temperature dependence of breakdown voltage vs. doping density characteristics ($\hbar\omega_{op}$=0.19 eV) [128]. The a and b are constants presented in Table 7.3 T and T_0 are temperature parameters.

Table 7.3: Ionization coefficients for Si and 4H-SiC used in ECORCE modeling [128, 129]

Material	**Parameter**	**Units**	$\mathbf{e^-}$	$\mathbf{h^+}$
Si	a_{300}	V^{-1}	0.426	0.243
	b_{300}	V/cm	4.81×10^5	6.53×10^5
	c	K^{-1}	3.05×10^{-4}	5.35×10^{-4}
	d	K^{-1}	6.86×10^{-4}	5.67×10^{-4}
4H-SiC	a	cm^{-1}	1.76×10^8	3.41×10^8
	b	V/cm	3.30×10^7	2.50×10^7

Finally, using Equation 7.1 for Si and Equations 7.2 and 7.3 for SiC, we can calculate the total impact ionization induced for e-h carries:

$$\alpha_{tot} = \alpha_e e V_e (\alpha_h h V_h) \tag{7.4}$$

where e is the electron density, h the hole density, V_e and V_h are the carries mobility multiply for the modulus of the electric field.

It is important to note that for both Si and SiC, we use the same Equation 7.4. To demonstrate the results of the ionizing impact, Figure 7.6 displays the modeling performed with ECORCE at 300 K of temperature, and using $e = 1 \times 10^{15}\ cm^{-3}$ and $h = 1 \times 10^{15}\ cm^{-3}$. It shows that the evolution of impact ionization rate in Si, for an electric field range between 0 and 1 MV/cm, is similar than the one in SiC, for a range between 0 and 6 MV/cm.

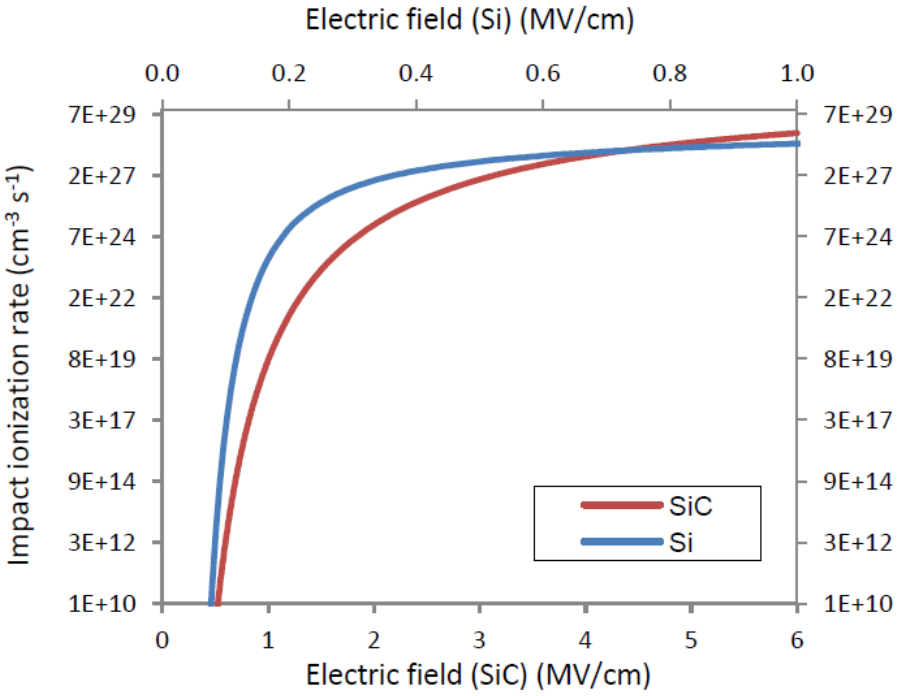

Figure 7.6: Impact ionization rate as a function of electric field for Si (blue) and SiC (red).

7.3.2 Thermal runaway results

To address the main mechanisms discussed in the Section 7.2, Figure 7.7 presents the maximum temperature, electric field, and thermal Joule power density as a function of time for -600 V biased SiC diode (red curves) and -200 V biased Si diode (blue curve). Fig. 7a shows the calculated values of power heat density (W_j) for both diodes, while the Fig. 7b presents the electric field in time that reaches its maximum (E_{max}), as follows:

- at t = 547 ps, E_{max} = 0.88 MV/cm, W_j = 3.75 W μm^{-3} for the Si diode.
- at t = 59 ps, E_{max} = 6.2 MV/cm, W_j = 613 W μm^{-3} for the SiC diode.

These results validate the earlier explanation regarding the burnout sensitivity of SiC diodes. In Si Schottky diodes, impact ionization acts as a self-regulating mechanism. When the electric field reaches the critical threshold, impact ionization generates additional electron-hole pairs, increasing the local carrier density. This increase in carriers enhances the electrical conductivity, which, in turn, reduces the electric field within the device. By lowering the electric field, the process prevents further escalation of Joule heating, thereby mitigating the risk of thermal runaway and device burnout. In contrast, for SiC Schottky diodes, the critical electric field for impact ionization is much higher. As a result, the Joule heating effect can rise uncontrollably and leading to burnout.

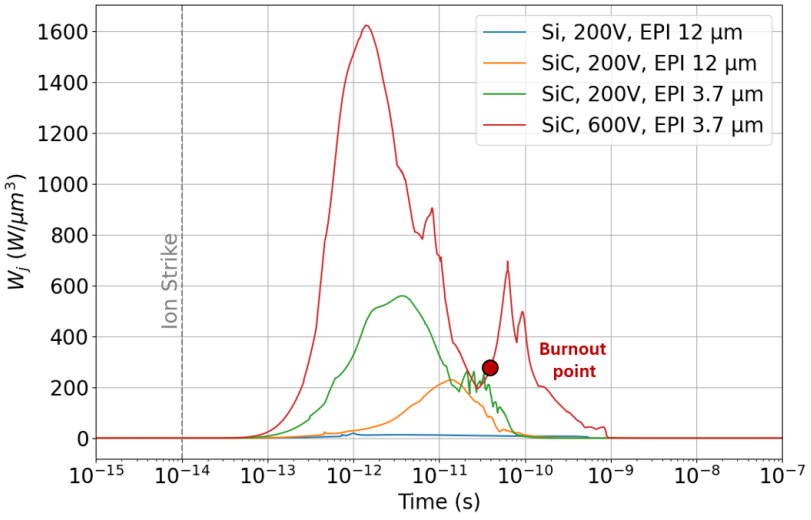

(a)

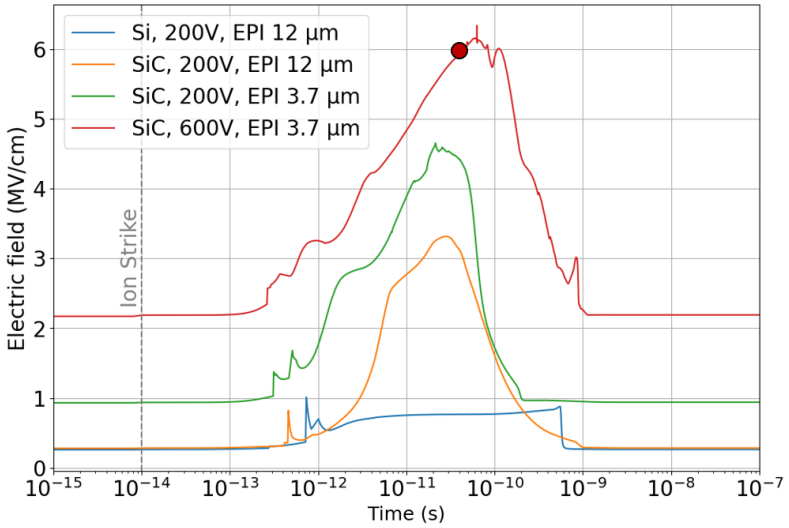

(b)

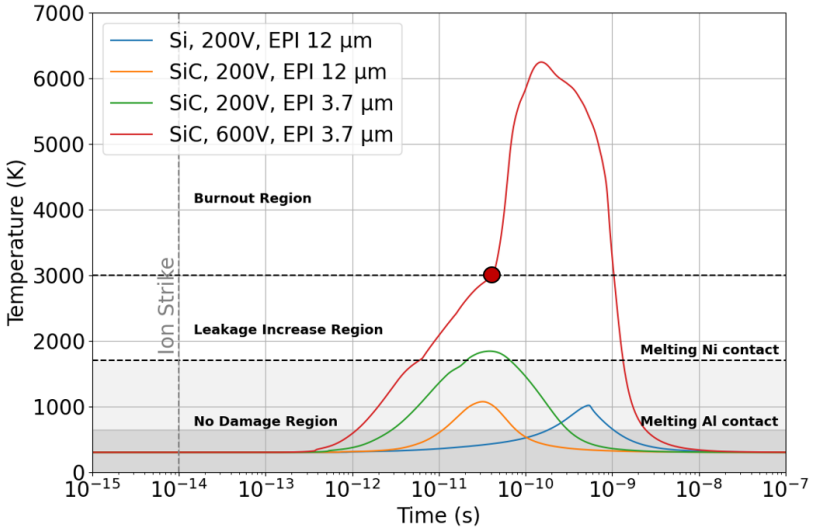

(c)

Figure 7.7: Simulation results as a function of time: (a) Power heat density, (b) Electric field, and (c) Temperature. The red dots highlight the diode burnout point.

It is well known that reducing the applied bias during irradiation helps mitigate burnout. To illustrate this effect, we present results for the SiC diode biased at -200 V (green curves in Figure 7.7). A key distinction between SiC and Si diodes lies in their structural parameters, particularly the epi layer thickness and doping levels. To isolate and analyze the impact of these structural differences, we also include results for a SiC diode modeled with the same structural parameters as the Si-based device (orange curve). The epi layer used has a thickness of 12 μm and a doping concentration of $1 \times 10^{15} cm^{-3}$.

Figure 7.7c reveals three distinct operational regions based on temperature. First, when the temperature exceeds the melting point of SiC, burnout occurs. Second, if the temperature falls between the melting point of SiC and the melting point of the Schottky contact material, damage will occur at the contact region, resulting in an increase in leakage current. Finally, if the temperature remains below the melting point of the Schottky contact material, no failures are expected.

The specific melting point of the Schottky contact material depends on the metal used, which influences the thermal resilience of the contact. These findings align closely with experimental results reported in prior studies [119, 120, 121, 122], providing further validation of the modeled behavior and underlying mechanisms.

The temperature for the -200 V biased SiC diodes (green and orange curves) is lower than the one for the -600 V biased SiC diode (red curve) but still high enough to induce damages and induce increase in leakage current (aluminum material). We can observe that both the maximum electric field and the maximum power heat density are also high. This sensitivity of SiC Schottky diodes at low bias voltage has already been highlighted by experiments [118]. However, for a SiC diode using the same structural parameters of the Si device (12 μm thickness and 10^15 cm^{-3} doping) and considering the many advantages of SiC material, we expected that no damage could occur. It appears that even with these reduced constraints, the temperature still reaches a value that can damage the Schottky material. Finally, as expected, the Si diode shows the lowest temperature, but it occurs later and shorter. We can expect reduced damages even if the temperature is still in the region where leakage increase will occur.

The temperature for the SiC diodes biased at -200 V (green and orange curves) is lower than that for the -600 V biased SiC diode (red curve). However, it remains sufficiently high to cause damage in the Schottky contact and increase leakage current, particularly when aluminum is used. Both the maximum electric field and the maximum power heat density for the -200 V SiC diodes are also significant, contributing to their sensitivity. This heightened sensitivity of SiC Schottky diodes, even at low bias voltages, has been corroborated by previous experimental studies [118].

Interestingly, for the SiC diode modeled with the same structural parameters as the Si diode (an epi layer thickness of 12 μm and doping of 1×10^{15} cm^{-3}), it was initially expected that no damage would occur, given the intrinsic advantages of SiC materials. However, the results indicate that even under these less demanding conditions, the temperature still reaches levels capable of damaging the Schottky contact.

In contrast, the Si diode exhibits the lowest temperature among the scenarios studied. Moreover, the high-temperature phase for the Si diode occurs later and lasts for a much shorter duration. As a result, even if the temperature approaches the melting point of the aluminum contact, the short time span minimizes the risk of significant damage.

All these effects are consistent with the trends that have been discussed in the literature considering experimental data [116, 117, 118, 119, 120, 121, 122]. However, these trends represent only secondary effects generated by the critical electric field. To our knowledge, the main mechanism described in this paper has never been mentioned before.

7.3.3 Band-to-band tunneling analysis

Another effect that plays a significant role in SiC Schottky diodes and still unresolved is the Band-to-Band tunneling (BBT) [135]. The BBT process occurs when electrons tunnel directly from the valence band to the conduction band. While impact ionization needs an electric field higher than the critical electric field and free carriers to be triggered, BBT only needs a high electric field to be triggered. So, when the electric field increases, carriers are removed and the impact ionization rate is lowered. In this sense, Figures 7.8 and 7.9 present the correlation between the impact ionization and BBT, demonstrating the different impacts depending on the structure of the Schottky diodes.

Figure 7.8 illustrates the impact ionization rate, which aligns with the peak electric field for Si diode and are very close for SiC diodes. This synchronization indicates that the highest rate of carrier generation through impact ionization and tunneling occurs when the electric field reaching its maximum intensity. This phenomenon underscores the interplay between impact ionization and Band-to-Band Tunneling (BBT), as both processes are highly dependent on the electric field strength.

However, Figure 7.9 highlights a notable difference in the behavior of BBT after this peak event. In the Si diode, BBT quickly reduces following the maximum impact ionization rate, which corresponds with the reduction in electric field strength and the subsequent stabilization of the diode. This rapid decline in BBT reflects a self-limiting mechanism in Si devices where impact ionization temporarily increases the carrier density but does not sustain high BBT rates due to the lower electric field. In contrast, the diode SiC at 600 V exhibits a persistent and elevated BBT rate even after the impact ionization peak. This sustained BBT can be attributed to the higher critical electric field inherent in SiC devices and the elevated temperature conditions that are reached during the ionization. The high electric field in SiC maintains the conditions necessary for BBT, leading to continuous tunneling current that exacerbates leakage and increases the likelihood of thermal runaway, which lead to the burnout.

To further investigate the relationship between temperature, electric field, and their impact on these mechanisms, Figure 7.10 presents the analysis of the impact ionization rate as a function of temperature. Figure 7.11 shows the behavior of band-to-band tunneling (BBT) as a function of temperature. Figures 7.10 and 7.11 are obtained

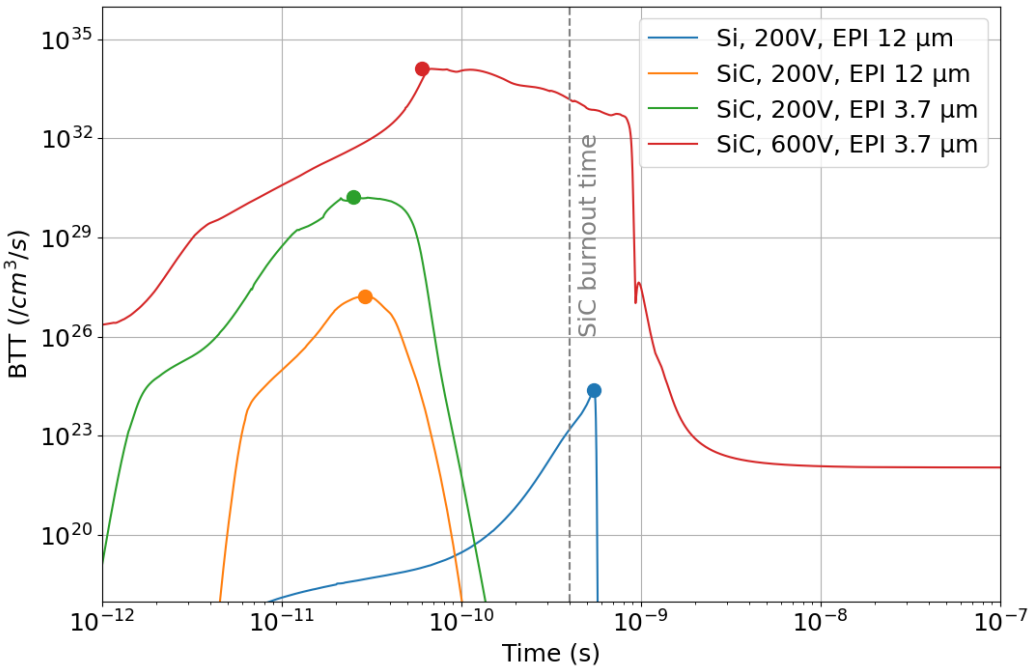

Figure 7.8: Band-to-Band tunneling as a function of time. Burnout occurs only for red curve.The maximum BTT is highlighted for each curve.

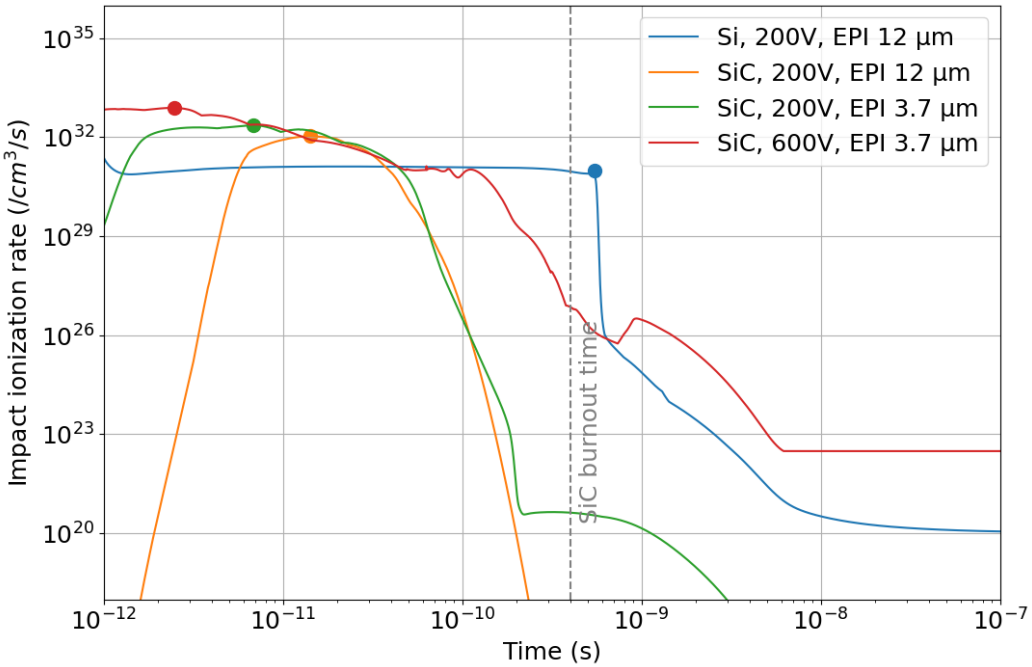

Figure 7.9: Impact ionization rate as a function of time. Burnout occurs only for red curve. The maximum impact ionization rate is highlighted for each curve.

considering a maximum electric fields for the materials: 0.88 MV/cm for Si and 6.33 MV/cm for SiC. Additionally, Figure 7.12 illustrates the variation of BBT as a function of the electric field at a temperature of 300 K for both materials. The objective of this analysis is to understand the influence of temperature and electric field on the BBT in Si and SiC materials.

Figure 7.10 illustrates the decrease in the impact ionization rate as temperature increases, with the analysis extending up to the melting point of each material. This decreasing of the impact ionization rate is expected, as higher temperatures result in greater thermal agitation, which reduces the carries mobility. As temperature rises, carriers experience a higher number of collisions with phonons (thermal vibrations of the crystal lattice). This scattering reduces the effective energy that carriers can accumulate in an electric field, making it less likely for them to reach the energy levels necessary to generate new electron-hole pairs through impact ionization. Furthermore, the carriers' energy becomes more dispersed due to thermal agitation, which decreases the concentration of high-energy carriers. Since impact ionization depends on collisions of carriers with sufficient energy to excite electrons into the conduction band, the likelihood of such events decreases, resulting in a reduced impact ionization rate.

Figure 7.11 shows that as temperature increases, the band-to-band tunneling (BBT) also increase, particularly, in SiC diodes. This behavior can be attributed to the intrinsic properties of SiC under high electric fields. Figure 7.12 demonstrates that BBT rates increase alongside the electric field. In SiC, the energy barrier for tunneling is significantly reduced under strong electric fields. Consequently, carriers in SiC have a higher probability of tunneling through the lowered energy barrier, resulting in a substantial rise in BBT rates compared to silicon, leading to sustained tunneling current.

In summary, impact ionization is influenced by the density of free electron-hole carriers, which decreases with increasing electric field due to carrier transport dynamics. Temperature also significantly affects both impact ionization and BBT: as temperature rises, impact ionization decreases, while BBT increases.

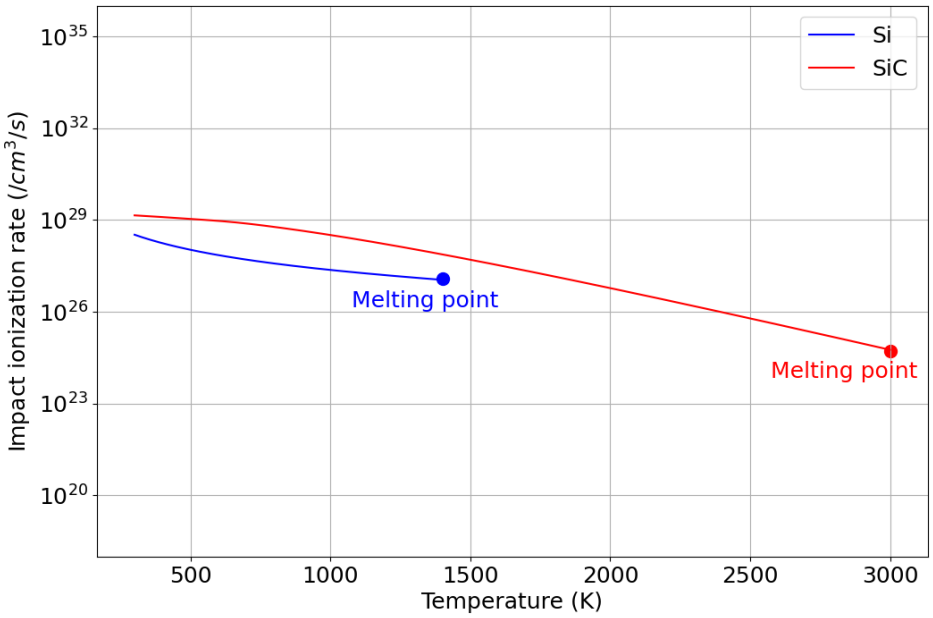

Figure 7.10: Impact ionization rate as a function of temperature.

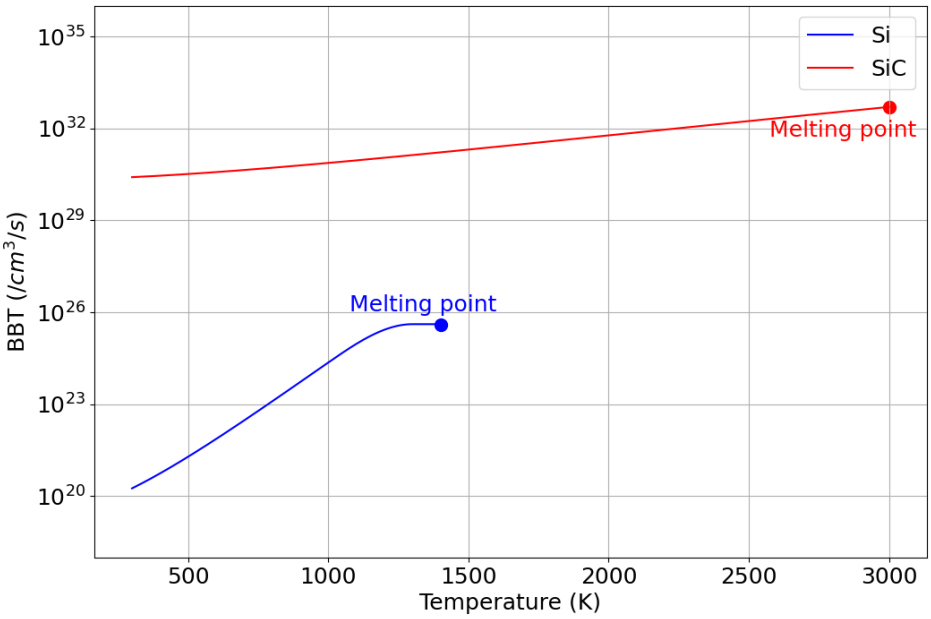

Figure 7.11: Band-to-Band tunneling as a function of temperature.

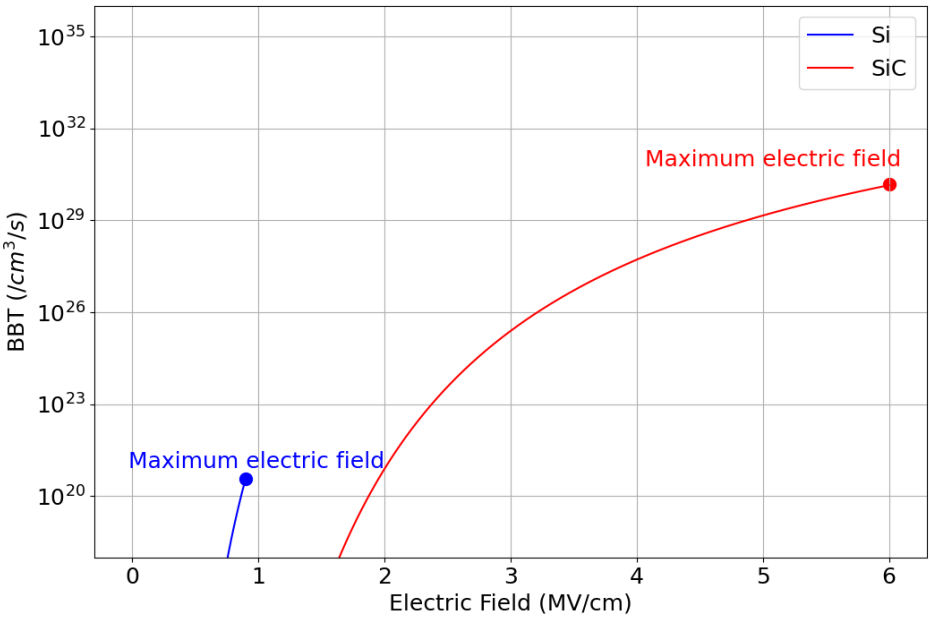

Figure 7.12: Band-to-Band tunneling as a function of electric field.

7.4 Conclusion

By comparing the physical mechanisms in SiC and Si Schottky diodes through TCAD, this work shows that the critical electric field is the main mechanism responsible for SiC susceptibility under heavy ion irradiation. We show that the impact ionization act as a protection for the Si Schottky diode, since the electric field is ceiled at a low value and due that the power heat density stays low. In the case of SiC, once the impact ionization starts, the electrostatic potential energy is already too high due the high electric field. For this reason, the power heat density exceeds the value that the device can handle safely.

The analysis of BBT supports this conclusion, showing that BBT plays a crucial role in the SiC Schottky diodes, distinguishing them significantly from Si diodes. BBT rates rise significantly in SiC diodes due to the reduction of the tunneling energy barrier under strong electric fields. This persistent BBT in SiC is primarily driven by the high electric fields inherent to SiC, which continuously sustain the conditions necessary for tunneling. In SiC, the critical electric field is much higher than in Si, allowing the diode to maintain a high tunneling rate even in the absence of new carriers generated by ionization. This prolonged BBT leads to continuous leakage current, making SiC diodes vulnerable to thermal runaway.

It can be assumed that similar effects may occur in other wide-bandgap semiconductors. However, properties such as high thermal conductivity and mobility laws may mitigate this issue.

Chapter 8

Conclusions

8.1 Thesis summary

This thesis proposes and explores complementary alternative modeling approaches for SEE in electronics. The study addresses various methodologies, including analytical models, Monte Carlo analysis, TCAD simulations, and multi-physics techniques.

In Chapter 3, an analytical model for Soft Error Rate (SER) prediction for neutrons is proposed. The model separates the interaction of radiation with matter from the geometry considerations of the sensitive volume, allowing express the SER as the sum of two components calculable for any threshold Linear Energy Transfer (LET_{th}) and sensitive volume size. Comparison with existing Monte Carlo simulation in the literature showed excellent agreement, validating its accuracy. Additionally, the study indicates that as technology scales down, the contribution of neutrons in the 1–10 MeV energy range to the SER is expected to decline, even as the LET_{th} decreases due to miniaturization.

Chapter 4 introduces a streamlined method for calculating and predicting the proton SEE cross-section. At low energy levels, a notable increase in the proton differential cross-section is observed, which makes unfeasible a direct Monte Carlo approach due the extended computation times to capture the tail of the low-energy recoiling ions spectrum. This study proposes a simplified modeling approach using only four input parameters (BEOL layer thickness, sensitive region thickness, technology LET_{th}, and heavy-ion cross-section data), we were able to compute the SEE cross-section for incident protons. The results show a good match with experimental data in both shape and magnitude across different technological nodes. The findings also emphasize that Coulomb elastic scattering on the nucleus is a significant contributor to SEE for protons in the 1–10 MeV energy range.

In Chapter 5, a multi-physics framework is introduced, integrating simplified electrical modeling with the diffusion–collection model and Monte Carlo simulations to estimate SEE cross-sections for heavy-ions using the PredicSEE tool. The results exhibit a strong correlation with experimental irradiation data, without the need for fitting the simulation results or accessing process design kit (PDK) data, establishing this method as a robust approach for calculating the SEE cross-section for heavy-ion irradiation.

Chapter 6 introduces an innovative approach for estimating the SEU cross-section using simplified two-dimensional Technology Computer-Aided Design (TCAD) modeling. This method overcomes challenges related to limited access to technological data and the complexity of TCAD simulations by utilizing academic and predictive SPICE models to derive most of the simulation parameters. The results show a strong correlation between simulation outcomes and experimental data, indicating that this approach is effective for assessing SEE cross-section predictions in conventional devices.

In Chapter 7, a detailed analysis investigates the increased susceptibility to ion-induced Burnout in silicon carbide (SiC) Schottky diodes compared to silicon (Si) Schottky diodes. While SiC's high critical electric field makes it attractive for power applications, the study reveals that this characteristic also contributes to its vulnerability to Single Event Burnout (SEB). The research uncovers the underlying physical mechanisms responsible for this effect, marking a novel contribution to the field.

SiC technologies as been expected to be ground breaking material for power devices, however because the hight sensitivity to burnout induced by ion this promising technologies can only be used in ground level, forbiden for space and avionics environments. We can suspect that even in ground level, vary rare cases, even neutron by generating secondary ions can generate burnout in this components. Of course, this have a low probability, but for large scale , like automotive can be a concern. Now the exact mechanism responsible for the failures of SiC under ion-irradiation is highlighted, and we can expected find a mitigation method to solve that issue.

Overall, this thesis assesses the advantages and limitations of various alternative modeling approaches, while providing significant insights into critical concerns related to radiation effects on electronic components. The findings offer valuable contributions to the understanding and prediction of SEE.

8.2 Contributions to the RADNEXT EU Project

This PhD thesis is part of the RADNEXT EU Project, which aims to establish a comprehensive network for radiation effects testing, providing access to radiation facilities and advancing radiation-hardening technologies for electronic components. The research conducted as part of this thesis is included in Work Package 8 (WP08), which focuses on the development and application of modeling tools to complement experimental efforts, thereby enhancing the understanding of radiation-induced effects in electronic devices. The main contributions of this thesis to RADNEXT EU project during its duration are as follows:

- **Simulation results of the importance of 1-10 MeV energy range on the SER for neutrons:** These research are detailed in Chapter 3 of this thesis and available in RADNEXT deliverable report D08.1 [136]. The probability that an secondary ion reaches the sensitive volume has been computed analytically. On the other end, the nuclear physics part has been calculated with the DHORIN database code. Two main functions have been derived: $I_V(LET_{th})$, which is related to the

nuclear reactions occurring inside the sensitive volume, and $I_S(LET_{th})$, which is related to those occurring outside. The atmospheric neutrons at 1-10 MeV and the 1-200 MeV energy ranges are investigated. The main conclusion is thus that we should not expect a drastic increase of the SER due to low energy neutrons in atmosphere, even if the sensitivity is increasing (as expressed by the decreasing LET_{th}). This research focus on neutrons in the atmosphere, but the methodology can be replicated for other environments such as accelerators.

- **Recommendation for simulating low energy protons:** This study, detailed in Chapter 4 of this thesis and presented within the framework of the RADNEXT deliverable D08.3 [136]. In this work, we provide an in-depth analysis of low-energy proton interactions with silicon. It examines both direct proton ionization and elastic scattering mechanisms, including nuclear and Coulombic scattering. The findings reveal that to accurately calculating the SEE cross-section for low-energy protons requires accounting for Coulombic scattering, the thickness of the BEOL, and the distance traveled by secondary ions before reaching the sensitive region. These parameters are essential for determining the LET distribution. Furthermore, the study underscores that using a simple step function for SEE cross-section calculations, as it can lead to significant discrepancies in the results. Instead, we propose the employing a power or weibull law, derived from heavy-ion experimental data, as a more reliable approach.

- **Simulation results and report on circuit modelling:** This work is thoroughly discussed in Chapter 5 of this thesis and documented in the RADNEXT deliverable report D08.4 [136]. Here, we evaluate the accuracy of a proposed alternative modeling approach by comparing it with experimental data. The primary objective of this work is to identify the limitations of the proposed approach and provide recommendations for its effective application in predicting radiation effects at the circuit level. The methodology combines simplified electrical modeling with the diffusion-collection model and Monte Carlo simulations to estimate SEE cross-sections. A notable advantage of this approach is that it does not require access to the technology's PDK or any fitting of simulation parameters. The results demonstrate a strong correlation with experimental data, indicating that the methodology effectively predicts SEE mechanisms, also considering the voltage scaling situation. However, the accuracy of the simulations decreases slightly in low LET scenarios and near-threshold voltage ranges. To enhance accuracy, the model could be refined by incorporating the internal capacitance of nodes (not only the input and output values), and fine-tuning critical parameters such as the doping profile.

- **Neutron test campaign:** In July 2024, a radiation test campaign was conducted as part of this thesis at ChipIR, a neutron facility located at the end of the ISIS spallation neutron source beamline, at the Rutherford Appleton Laboratory in Didcot, UK. ChipIR is specifically designed for studying single event effects (SEEs) and is optimized to replicate a neutron spectrum closely resembling that of the atmosphere [137]. The primary objective of this campaign was to gain practical

experience in radiation testing and to collect experimental data related to SRAM memories. This data will be used to evaluate the accuracy and limitations of alternative modeling approaches. The test setup consists of a Field-Programmable Gate Array (FPGA) controller coupled with a test board developed for this experiment. The controller managed the write and read operations of the memories. Figure 8.1 shows the FPGA Module used. The test board, detailed in Figure 8.2, contained four SRAM memories: two with a 32 Mbit and two with a 16 Mbit. During testing, one memory executed a dynamic test pattern while the remaining three operated in static mode. The FPGA controller utilized the HARV-SoC architecture to harden the processor against SEEs [138]. Errors detected during testing were logged systematically for analysis. Additionally, a current monitoring system was developed to manage the experiment from the control room. This system continuously monitored the current and voltage levels of the boards. Any unexpected increase in current triggered an automatic power cycle to protect the components, although manual intervention was also possible. This setup was developed to maximize beam time efficiency, running over 10 hours without interruption. Figure 8.3 illustrates the detailed configuration of the test setup used during this campaign. The Devices Under Test (DUTs) were Commercial Off-The-Shelf (COTS) 40 nm SRAMs. Table 8.1 details the specifications of the tested devices. The results of this test campaign are still under evaluation. Further data analysis, including a detailed comparison with simulation results, is ongoing and will be presented in future work.

Table 8.1: Specification of tested devices.

Reference	Technology	Size	Nominal voltage
IS61WV204816BLL-10TLI	40 nm	32 Mbit	3.3 V
IS61WV102416BLL-10TLI	40 nm	16 Mbit	3.3 V

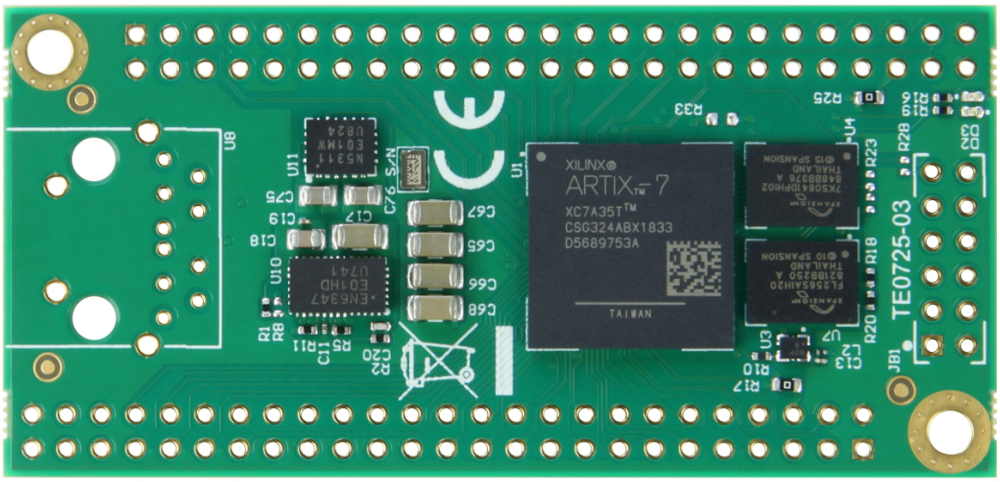

Figure 8.1: Controler FPGA Module with AMD Artix™ 7A35T-2C [139].

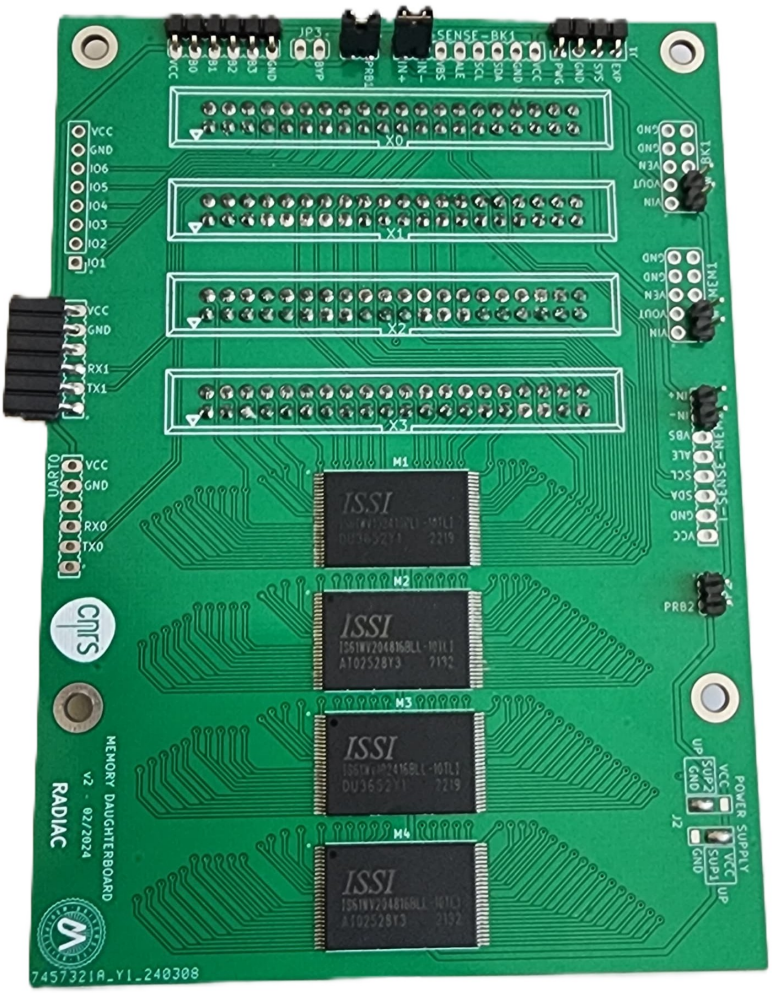

Figure 8.2: Memory daughter board.

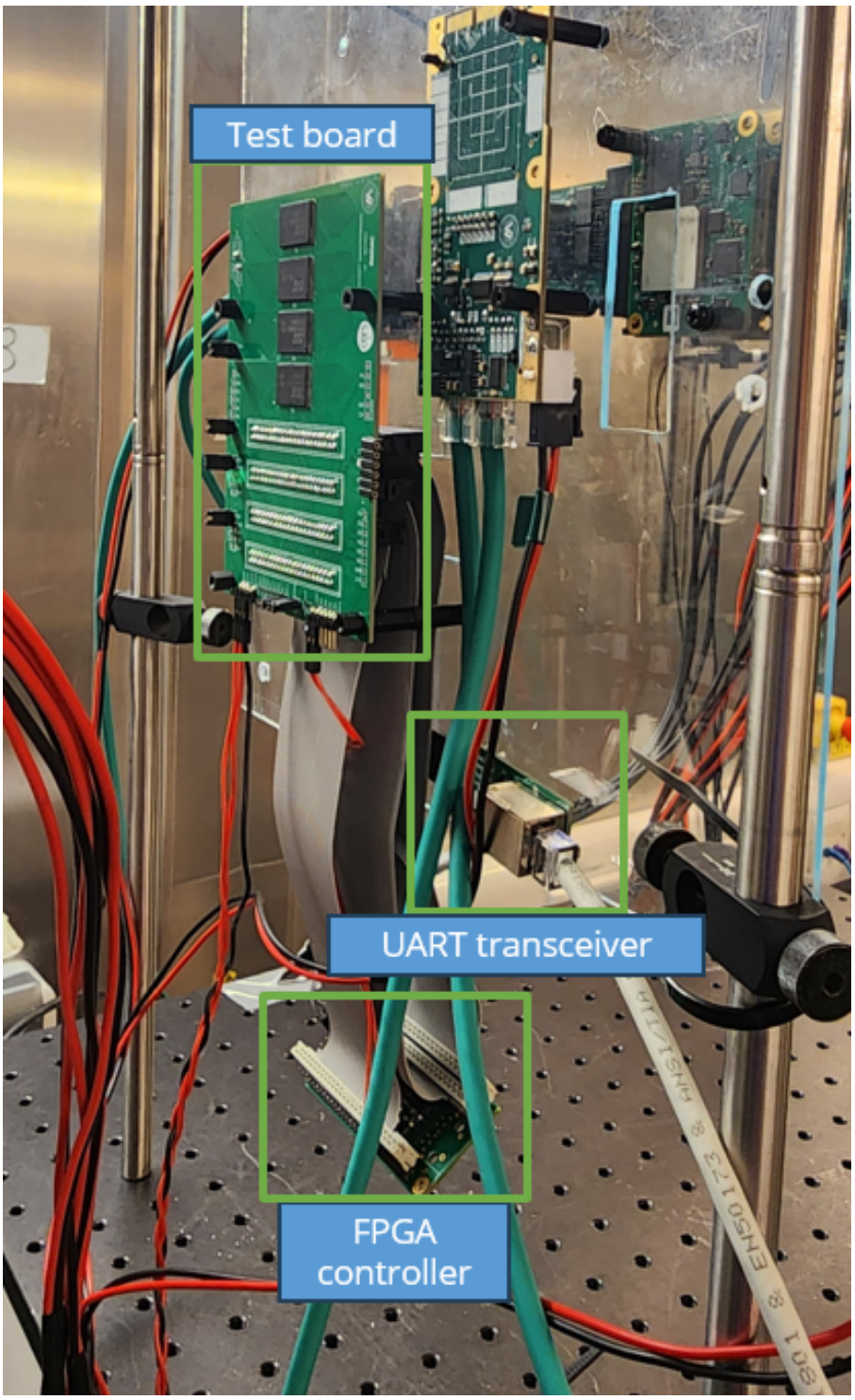

Figure 8.3: 40 nm SRAM neutron beam test setup.

Another key aspect within the scope of the RADNEXT project is the dissemination of these findings to the broader scientific community. To achieve this, the results have been shared extensively through contributions to international journals and presentations at various conferences.

Publications:

- F. Wrobel, Y.Q. Aguiar, **C. M. Marques**, G. Lerner, R.G. Alía, F. Saigné, and J. Boch., "An Analytical Approach to Calculate Soft Error Rate Induced by Atmospheric Neutrons", MDPI Electronics, 2022. DOI: 10.3390/electronics12010104.
- **C. M. Marques**, L. H. Brendler, F. Wrobel, A. L. Zimpeck, W. E. C. Bartra, P. F. Butzen, C. Meinhardt, "A Detailed Electrical Analysis of SEE on 28 nm FD-SOI SRAM Architectures", IEEE Symposium on Integrated Circuits and Systems Design (SBCCI), 2023. DOI: 10.1109/SBCCI60457.2023.10261665.
- **C. M. Marques**, F. Wrobel, Y.Q. Aguiar, A. Michez, J. Boch, F. Saigné, and R.G. Alía., "A Methodology to Estimate Single-Event Effects Induced by Low-Energy Protons", MDPI Eng, 2023. DOI: 10.3390/eng5010017.
- **C. M. Marques**, F. Wrobel, Y.Q. Aguiar, A. Michez, F. Saigné, J. Boch, L. Dilillo, and R.G. Alía., "Evaluation of a Simplified Modeling Approach for SEE cross-section Prediction: A Case Study of SEU on 6T SRAM Cells", MDPI Electronics, 2024. DOI: 10.3390/electronics13101954.
- **C. M. Marques**, A. Michez, F. Wrobel, S. Kuboyama, F. Saigné, Y.Q. Aguiar, L. Dilillo, and R.G. Alía., "Why SiC Schottky Diodes Are More Sensitive to Ion-induced Burnout Than Si Schottky Diodes?", Proceedings of Radiation Effects on Components and Systems (RADECS), 2024.
- **C. M. Marques**, A. Michez, F. Wrobel, S. Kuboyama, F. Saigné, Y.Q. Aguiar, L. Dilillo, and R.G. Alía., "Physical Explanation for the Higher Sensitivity to Ion-Induced Burnout in SiC Schottky Diodes Compared to Si Schottky Diodes", submitted IEEE Transactions on Nuclear Science (under review).

Presentations:

- Poster presentation, 18th International School on the Effects of Radiation on Embedded Systems for Space Applications (SERESSA), Geneva - Switzerland, 2022.
- Oral presentation, "Use of Single Event Effect prediction tool", RADNEXT 1st annual meeting, Geneva - Switzerland, 2022.
- Oral presentation, "SEU cross-section prediction", RADNEXT 2nd annual meeting, Seville - Spain, 2023.
- Oral presentation, "A Detailed Electrical Analysis of SEE on 28 nm FDSOI SRAM Architectures", IEEE Symposium on Integrated Circuits and Systems Design (SBCCI), Rio de Janeiro - Brazil, 2023.
- Oral presentation, "SEE cross-section prediction using PredicSEE tool", G-RADNEXT Workshop, Geneva - Switzerland, 2023.

- Poster presentation, "Why SiC Schottky Diodes Are More Sensitive to Ion-induced Burnout Than Si Schottky Diodes?", Radiation Effects on Components and Systems (RADECS), Maspalomas - Spain, 2024.
- Oral presentation, "SEU cross-section calculation using 2D TCAD modeling", RADNEXT 3rd annual meeting, Didcot - United Kingdom, 2024.

8.3 Future works

Many studies presented in this thesis can be extended for future developments. Potential directions include:

- Validation for Emerging Technologies: While this thesis primarily focuses on bulk-planar CMOS technologies, validating the proposed methodologies for advanced nodes such as Fully-Depleted Silicon-On-Insulator (FDSOI) and Fin Field-Effect Transistor (FinFET) technologies could demonstrate their applicability across a wider range of semiconductor devices.
- 3D TCAD Modeling: Extending the current 2D TCAD-based SEU cross-section methodology to include 3D modeling could provide a more comprehensive analysis of three-dimensional effects in device structures, potentially enhancing prediction accuracy for advanced and highly scaled technologies.
- Evaluation of SPICE Model Accuracy: Incorporating more precise SPICE models, possibly utilizing actual Process Design Kit (PDK) data when available, could improve simulation accuracy, particularly in low-LET regions where small parameter variations can significantly influence results.
- Analysis of Experimental Data: Further analysis of the experimental data obtained during the test campaign, combined with a comparison of alternative approaches proposed in this thesis, could yield deeper insights and validate the methodologies more robustly.

Bibliography

[1] R.C. Baumann. "Radiation-induced soft errors in advanced semiconductor technologies". In: *IEEE Transactions on Device and Materials Reliability* 5.3 (2005), pp. 305–316. DOI: 10.1109/TDMR.2005.853449.

[2] Matthew J. Gadlage et al. "Scaling Trends in SET Pulse Widths in Sub-100 nm Bulk CMOS Processes". In: *IEEE Transactions on Nuclear Science* 57.6 (2010), pp. 3336–3341. DOI: 10.1109/TNS.2010.2071881.

[3] G. Hubert, L. Artola, and D. Regis. "Impact of scaling on the soft error sensitivity of bulk, FDSOI and FinFET technologies due to atmospheric radiation". In: *Integration* 50 (2015), pp. 39–47. ISSN: 0167-9260. DOI: 10.1016/j.vlsi.2015.01.003.

[4] Sascha Lüdeke et al. "Proton Direct Ionization in Sub-Micron Technologies: Test Methodologies and Modeling". In: *IEEE Transactions on Nuclear Science* 70.4 (2023), pp. 667–677. DOI: 10.1109/TNS.2023.3255008.

[5] F. Wrobel et al. "Heavy Ion SEU Cross Section Calculation Based on Proton Experimental Data, and Vice Versa". In: *IEEE Transactions on Nuclear Science* 61.6 (2014), pp. 3564–3571. DOI: 10.1109/TNS.2014.2368613.

[6] Balaji Narasimham et al. "Scaling trends and bias dependence of the soft error rate of 16 nm and 7 nm FinFET SRAMs". In: *2018 IEEE International Reliability Physics Symposium (IRPS)*. 2018, pp. 4C.1–1–4C.1–4. DOI: 10.1109/IRPS.2018.8353583.

[7] James M. Cannon et al. "Electrical Measurement of Cell-to-Cell Variation of Critical Charge in SRAM and Sensitivity to Single-Event Upsets by Low-Energy Protons". In: *IEEE Transactions on Nuclear Science* 68.5 (2021), pp. 815–822. DOI: 10.1109/TNS.2021.3061672.

[8] Mario Sacristán Barbero et al. "Characterization of Fragmented Ultrahigh-Energy Heavy Ion Beam and Its Effects on Electronics Single-Event Effect Testing". In: *IEEE Transactions on Nuclear Science* 71.8 (2024), pp. 1557–1564. DOI: 10.1109/TNS.2024.3396737.

[9] J. T. Wallmark and S. M. Marcus. "Minimum Size and Maximum Packing Density of Nonredundant Semiconductor Devices". In: *Proceedings of the IRE* 50.3 (1962), pp. 286–298. DOI: 10.1109/JRPROC.1962.288321.

[10] D. Binder, E. C. Smith, and A. B. Holman. "Satellite Anomalies from Galactic Cosmic Rays". In: *IEEE Transactions on Nuclear Science* 22.6 (1975), pp. 2675–2680. DOI: 10.1109/TNS.1975.4328188.

[11] Timothy C. May and Murray H. Woods. "A New Physical Mechanism for Soft Errors in Dynamic Memories". In: *16th International Reliability Physics Symposium*. 1978, pp. 33–40. DOI: 10.1109/IRPS.1978.362815.

[12] C. S. Guenzer, E. A. Wolicki, and R. G. Allas. "Single Event Upset of Dynamic Rams by Neutrons and Protons". In: *IEEE Transactions on Nuclear Science* 26.6 (1979), pp. 5048–5052. DOI: 10.1109/TNS.1979.4330270.

[13] M. Rodgers et al. “2001 Technology Roadmap for Semiconductors”. In: *Computer* 35.01 (2002), pp. 42–53. ISSN: 1558-0814. DOI: 10.1109/2.976918.

[14] T. Granlund, B. Granbom, and N. Olsson. “Soft error rate increase for new generations of SRAMs”. In: *IEEE Transactions on Nuclear Science* 50.6 (2003), pp. 2065–2068. DOI: 10.1109/TNS.2003.821593.

[15] Oluwole A. Amusan et al. “Charge Collection and Charge Sharing in a 130 nm CMOS Technology”. In: *IEEE Transactions on Nuclear Science* 53.6 (2006), pp. 3253–3258. DOI: 10.1109/TNS.2006.884788.

[16] N. N. Mahatme et al. “Analysis of soft error rates in combinational and sequential logic and implications of hardening for advanced technologies”. In: *2010 IEEE International Reliability Physics Symposium*. 2010, pp. 1031–1035. DOI: 10.1109/IRPS.2010.5488680.

[17] L. Artola and G. Hubert. “Modeling of Elevated Temperatures Impact on Single Event Transient in Advanced CMOS Logics Beyond the 65-nm Technological Node”. In: *IEEE Transactions on Nuclear Science* 61.4 (2014), pp. 1611–1617. DOI: 10.1109/TNS.2014.2301877.

[18] Sergeh Vartanian et al. “Single Event Effects Results for COTS Microcontrollers and Microprocessors”. In: *2023 IEEE Radiation Effects Data Workshop (REDW) (in conjunction with 2023 NSREC)*. 2023, pp. 1–5. DOI: 10.1109/REDW61050.2023.10265843.

[19] Rubén García Alía et al. “Heavy Ion Energy Deposition and SEE Intercomparison Within the RADNEXT Irradiation Facility Network”. In: *IEEE Transactions on Nuclear Science* 70.8 (2023), pp. 1596–1605. DOI: 10.1109/TNS.2023.3260309.

[20] RADNEXT. “RADiation facility Network for the EXploration of effects for indusTry and research”. In: URL: https://radnext.web.cern.ch.

[21] NASA. “Nasa’s van allen probes reveal previously undetected radiation belt around earth”. In: URL: https://www.nasa.gov.

[22] SÉbastien Bourdarie and Michael Xapsos. “The Near-Earth Space Radiation Environment”. In: *IEEE Transactions on Nuclear Science* 55.4 (2008), pp. 1810–1832. DOI: 10.1109/TNS.2008.2001409.

[23] F. W. Sexton. “Measurement of single event phenomena in devices and ics”. In: 1992.

[24] Peter Meyer, Reuven Ramaty, and William R. Webber. “Cosmic rays—astronomy with energetic particles”. In: *Physics Today* 27.10 (Oct. 1974), pp. 23–32. ISSN: 0031-9228. DOI: 10.1063/1.3128914.

[25] K. Nagashima and I. Morishita. “Twenty-two year modulation of cosmic rays associated with polarity reversal of polar magnetic field of the sun”. In: *Planetary and Space Science* 28.2 (1980), pp. 195–205. ISSN: 0032-0633. DOI: https://doi.org/10.1016/0032-0633(80)90095-1.

[26] Mihir Desai and Joe Giacalone. “Large gradual solar energetic particle events”. In: *Living Reviews in Solar Physics* 13.1 (2016), p. 3.

[27] IVj Dorman and LI Dorman. “Solar wind properties obtained from the study of the 11-year cosmic-ray cycle: 1”. In: *Journal of Geophysical Research* 72.5 (1967), pp. 1513–1520.

[28] NOAA. “Space weather prediction center”. In: URL: https://www.swpc.noaa.gov.

[29] TRAD. "OMERE software". In: URL: https://www.trad.fr/en/space/omere-software/.

[30] J.L. Barth, C.S. Dyer, and E.G. Stassinopoulos. "Space, atmospheric, and terrestrial radiation environments". In: *IEEE Transactions on Nuclear Science* 50.3 (2003), pp. 466–482. DOI: 10.1109/TNS.2003.813131.

[31] Matteo Cecchetto. "Experimental and simulation study of neutron-induced single event effects in accelerator environment and implications on qualification approach". PhD thesis. Université Montpellier, 2021.

[32] Yi-Pin Fang and Anthony S. Oates. "Muon-Induced Soft Errors in SRAM Circuits in the Terrestrial Environment". In: *IEEE Transactions on Device and Materials Reliability* 15.1 (2015), pp. 115–122. DOI: 10.1109/TDMR.2015.2396673.

[33] Seiya Manabe et al. "Estimation of Muon-Induced SEU Rates for 65-nm Bulk and UTBB-SOI SRAMs". In: *IEEE Transactions on Nuclear Science* 66.7 (2019), pp. 1398–1403. DOI: 10.1109/TNS.2019.2916191.

[34] F. Lei et al. "An atmospheric radiation model based on response matrices generated by detailed Monte Carlo Simulations of cosmic ray interactions". In: *IEEE Transactions on Nuclear Science* 51.6 (2004), pp. 3442–3451. DOI: 10.1109/TNS.2004.839131.

[35] Weijun Ni et al. "Possible atmospheric-like neutron beams at CSNS". In: *Radiation Physics and Chemistry* 152 (2018), pp. 43–48.

[36] JEDEC. "The International Technology Roadmap for Semiconductors". In: URL: https://www.jedec.org/standards-documents/docs/jesd-89a.

[37] IEC. "Process Management for Avionics–Atmospheric Radiation Effects–Part 1: Accommodation of Atmospheric". In: *Radiation Effects via Single Event Effects within Avionics Electronic Equipment* (2006).

[38] ESA. "ESCC 22900 - Total dose steady-state irradiation test method". In: URL: https://escies.org/escc-specs/published/22900.pdf.

[39] Vincent Girones et al. "Comparison of High Energy X-Ray and Cobalt-60 Irradiations on MOS Capacitors". In: *IEEE Transactions on Nuclear Science* 71.8 (2024), pp. 1879–1886. DOI: 10.1109/TNS.2024.3366432.

[40] Jialei Wang. "A Flexible SRAM based SEE Radiation Monitor". PhD thesis. Katholieke Universiteit Leuven, 2022.

[41] CERN. "The CERN accelerator complex in 2019". In: URL: https://cds.cern.ch/record/2684277.

[42] CERN. "CERN Document Server". In: URL: https://cds.cern.ch/record/2684277.

[43] J.L. Autran and D. Munteanu. *Soft Errors: From Particles to Circuits*. CRC Press, 2015. DOI: 10.1201/b18132.

[44] J.F Ziegler. "The TRansport of Ions in Matter. IBM-Research". In: (1996). URL: http://www.srim.org/.

[45] Ygor Quadros de Aguiar et al. *Single-Event Effects, from Space to Accelerator Environments: Analysis, Prediction and Hardening by Design*. 2025.

[46] Kevin M. Warren et al. "Monte-Carlo Based On-Orbit Single Event Upset Rate Prediction for a Radiation Hardened by Design Latch". In: *IEEE Transactions on Nuclear Science* 54.6 (2007), pp. 2419–2425. DOI: 10.1109/TNS.2007.907678.

[47] Guillaume Hubert et al. “Operational SER Calculations on the SAC-C Orbit Using the Multi-Scales Single Event Phenomena Predictive Platform (MUSCA SEP^3)”. In: *IEEE Transactions on Nuclear Science* 56.6 (2009), pp. 3032–3042. DOI: 10.1109/TNS.2009.2034148.

[48] W.E. Calienes et al. “Evaluation of heavy-ion impact in bulk and FDSOI devices under ZTC condition”. In: *Microelectronics Reliability* 76-77 (2017), pp. 655–659. ISSN: 0026-2714. DOI: https://doi.org/10.1016/j.microrel.2017.06.063.

[49] Cleiton M. Marques et al. “Evaluation of a Simplified Modeling Approach for SEE Cross-Section Prediction: A Case Study of SEU on 6T SRAM Cells”. In: *Electronics* 13.10 (2024). ISSN: 2079-9292. DOI: 10.3390/electronics13101954.

[50] Wei Zhao and Yu Cao. “New generation of predictive technology model for sub-45nm design exploration”. In: *7th International Symposium on Quality Electronic Design (ISQED'06)*. 2006, 6 pp.–590. DOI: 10.1109/ISQED.2006.91.

[51] Dávid Lucsányi et al. “G4SEE: A Geant4-Based Single Event Effect Simulation Toolkit and Its Validation Through Monoenergetic Neutron Measurements”. In: *IEEE Transactions on Nuclear Science* 69.3 (2022), pp. 273–281. DOI: 10.1109/TNS.2022.3149989.

[52] Vincent Correas et al. “Innovative Simulations of Heavy Ion Cross Sections in 130 nm CMOS SRAM”. In: *IEEE Transactions on Nuclear Science* 54.6 (2007), pp. 2413–2418. DOI: 10.1109/TNS.2007.910038.

[53] Frédéric Wrobel and Frédéric Saigné. “MC-ORACLE: A tool for predicting Soft Error Rate”. In: *Computer Physics Communications* 182.2 (2011), pp. 317–321. ISSN: 0010-4655. DOI: https://doi.org/10.1016/j.cpc.2010.10.005. URL: https://www.sciencedirect.com/science/article/pii/S001046551000384X.

[54] G. C. Messenger. “Collection of Charge on Junction Nodes from Ion Tracks”. In: *IEEE Transactions on Nuclear Science* 29.6 (1982), pp. 2024–2031. DOI: 10.1109/TNS.1982.4336490.

[55] P.E. Dodd and L.W. Massengill. “Basic mechanisms and modeling of single-event upset in digital microelectronics”. In: *IEEE Transactions on Nuclear Science* 50.3 (2003), pp. 583–602. DOI: 10.1109/TNS.2003.813129.

[56] M. Andjelkovic et al. “An overview of the modeling and simulation of the single event transients at the circuit level”. In: *2017 IEEE 30th International Conference on Microelectronics (MIEL)*. 2017, pp. 35–44. DOI: 10.1109/MIEL.2017.8190065.

[57] Giuseppe Battistoni et al. “Overview of the FLUKA code”. In: *Annals of Nuclear Energy* 82 (2015). Joint International Conference on Supercomputing in Nuclear Applications and Monte Carlo 2013, SNA + MC 2013. Pluri- and Trans-disciplinarity, Towards New Modeling and Numerical Simulation Paradigms, pp. 10–18. ISSN: 0306-4549. DOI: https://doi.org/10.1016/j.anucene.2014.11.007. URL: https://www.sciencedirect.com/science/article/pii/S0306454914005878.

[58] S. Agostinelli et al. “Geant4—a simulation toolkit”. In: *Nuclear Instruments and Methods in Physics Research Section A: Accelerators, Spectrometers, Detectors and Associated Equipment* 506.3 (2003), pp. 250–303. ISSN: 0168-9002. DOI: https://doi.org/10.1016/S0168-9002(03)01368-8.

[59] Yulia A. Novichkova et al. “Approach to Integration of a Synthesis Tool and PDK for Commercial EDA”. In: *2021 XV International Scientific-Technical Conference on Actual Problems Of Electronic Instrument Engineering (APEIE)*. 2021, pp. 24–27. DOI: 10.1109/APEIE52976.2021.9647544.

[60] J. F. Ziegler and W. A. Lanford. “Effect of Cosmic Rays on Computer Memories”. In: *Science* 206.4420 (1979), pp. 776–788. DOI: 10.1126/science.206.4420.776.

[61] J.R. Letaw and E. Normand. “Guidelines for predicting single-event upsets in neutron environments (RAM devices)”. In: *IEEE Transactions on Nuclear Science* 38.6 (1991), pp. 1500–1506. DOI: 10.1109/23.124138.

[62] Y. Tosaka et al. “Simple method for estimating neutron-induced soft error rates based on modified BGR model”. In: *IEEE Electron Device Letters* 20.2 (1999), pp. 89–91. DOI: 10.1109/55.740661.

[63] L.W. Connell, F.W. Sexton, and A.K. Prinja. “Further development of the Heavy Ion Cross section for single event UPset: model (HICUP)”. In: *IEEE Transactions on Nuclear Science* 42.6 (1995), pp. 2026–2034. DOI: 10.1109/23.489249.

[64] R. A. Reed et al. “Anthology of the Development of Radiation Transport Tools as Applied to Single Event Effects”. In: *IEEE Transactions on Nuclear Science* 60.3 (2013), pp. 1876–1911. DOI: 10.1109/TNS.2013.2262101.

[65] Heather Quinn et al. “The Effect of 1–10-MeV Neutrons on the JESD89 Test Standard”. In: *IEEE Transactions on Nuclear Science* 66.1 (2019), pp. 140–147. DOI: 10.1109/TNS.2018.2884908.

[66] Frédéric Wrobel et al. “An Analytical Approach to Calculate Soft Error Rate Induced by Atmospheric Neutrons”. In: *Electronics* 12.1 (2023). ISSN: 2079-9292.

[67] F. Wrobel. “Detailed history of recoiling ions induced by nucleons”. In: *Computer Physics Communications* 178.2 (2008), pp. 88–104. ISSN: 0010-4655. DOI: 10.1016/j.cpc.2007.08.005.

[68] Frédéric Wrobel. “Élaboration d’une base de données des particules responsables des dysfonctionnements dans les composants Électroniques exposés à des flux de protons ou de neutrons. Application au calcul des taux d’erreurs dans les mémoires SRAM en environnement radiatif naturel”. PhD thesis. Montpellier 2, 2002.

[69] F. Wrobel and P. Iacconi. “Parameterization of neutron-induced SER in bulk SRAMs from reverse Monte Carlo Simulations”. In: *IEEE Transactions on Nuclear Science* 52.6 (2005), pp. 2313–2318. DOI: 10.1109/TNS.2005.860751.

[70] P. Roche et al. “Comparisons of soft error rate for SRAMs in commercial SOI and bulk below the 130-nm technology node”. In: *IEEE Transactions on Nuclear Science* 50.6 (2003), pp. 2046–2054. DOI: 10.1109/TNS.2003.821588.

[71] G. Hubert et al. “Prediction of transient induced by neutron/proton in CMOS combinational logic cells”. In: *12th IEEE International On-Line Testing Symposium (IOLTS’06)*. 2006, 9 pp.–. DOI: 10.1109/IOLTS.2006.51.

[72] Efrem Sh. Sukhovitskiĭ Osamu Iwamoto Weili Sun Yukinobu Watanabe and Satoshi Chiba. “Evaluation of Cross Sections for Neutrons and Protons up to 200 MeV on Silicon Isotopes”. In: *Journal of Nuclear Science and Technology* 39.sup2 (2002), pp. 120–123. DOI: 10.1080/00223131.2002.10875055.

[73] Avraham Akkerman, Joseph Barak, and Nir M. Yitzhak. “Role of Elastic Scattering of Protons, Muons, and Electrons in Inducing Single-Event Upsets”. In: *IEEE Transactions on Nuclear Science* 64.10 (2017), pp. 2648–2660. DOI: 10.1109/TNS.2017.2747658.

[74] Kenneth P. Rodbell. “Low-Energy Protons—Where and Why “Rare Events” Matter”. In: *IEEE Transactions on Nuclear Science* 67.7 (2020), pp. 1204–1215. DOI: 10.1109/TNS.2020.2986642.

[75] Brian D. Sierawski et al. “Impact of Low-Energy Proton Induced Upsets on Test Methods and Rate Predictions”. In: *IEEE Transactions on Nuclear Science* 56.6 (2009), pp. 3085–3092. DOI: 10.1109/TNS.2009.2032545.

[76] P. Caron et al. “Physical Mechanisms of Proton-Induced Single-Event Upset in Integrated Memory Devices”. In: *IEEE Transactions on Nuclear Science* 66.7 (2019), pp. 1404–1409. DOI: 10.1109/TNS.2019.2902758.

[77] Andrea Coronetti et al. “Assessment of Proton Direct Ionization for the Radiation Hardness Assurance of Deep Submicron SRAMs Used in Space Applications”. In: *IEEE Transactions on Nuclear Science* 68.5 (2021), pp. 937–948. DOI: 10.1109/TNS.2021.3061209.

[78] Rubén García Alía et al. “Direct Ionization Impact on Accelerator Mixed-Field Soft-Error Rate”. In: *IEEE Transactions on Nuclear Science* 67.1 (2020), pp. 345–352. DOI: 10.1109/TNS.2019.2951307.

[79] E.L. Petersen. “Approaches to proton single-event rate calculations”. In: *IEEE Transactions on Nuclear Science* 43.2 (1996), pp. 496–504. DOI: 10.1109/23.490896.

[80] Insoo Jun et al. “Proton nonionizing energy loss (NIEL) for device applications”. In: *IEEE Transactions on Nuclear Science* 50.6 (2003), pp. 1924–1928. DOI: 10.1109/TNS.2003.820760.

[81] C. Vial et al. “A new approach for the prediction of the neutron-induced SEU rate”. In: *IEEE Transactions on Nuclear Science* 45.6 (1998), pp. 2915–2920. DOI: 10.1109/23.736547.

[82] J.-M. Palau et al. “Device simulation study of the SEU sensitivity of SRAMs to internal ion tracks generated by nuclear reactions”. In: *IEEE Transactions on Nuclear Science* 48.2 (2001), pp. 225–231. DOI: 10.1109/23.915368.

[83] Stefaan Tavernier. “Interactions of Particles in Matter”. In: *Experimental Techniques in Nuclear and Particle Physics*. Berlin, Heidelberg: Springer Berlin Heidelberg, 2010, pp. 23–53. DOI: 10.1007/978-3-642-00829-0_2.

[84] International Atomic Energy Agency—Nuclear Data Section. In: (2024), accessed on October 2024. URL: Availableonline:https://www-nds.iaea.org.

[85] P. Calvel et al. “An empirical model for predicting proton induced upset”. In: *IEEE Transactions on Nuclear Science* 43.6 (1996), pp. 2827–2832. DOI: 10.1109/23.556873.

[86] J Raynal. “CEA Saclay Report No. CEA-N-2772”. In: *ICTP International Seminar Course* (1994), accessed on October 2024. URL: Availableonline:https://www.scirp.org/reference/ReferencesPapers?ReferenceID=1459220.

[87] Brian D. Sierawski et al. “Contribution of low-energy (10 MeV) neutrons to upset rate in a 65 nm SRAM”. In: *2010 IEEE International Reliability Physics Symposium*. 2010, pp. 395–399. DOI: 10.1109/IRPS.2010.5488796.

[88] Andrea Coronetti et al. “SEU characterization of commercial and custom-designed SRAMs based on 90 nm technology and below”. In: *2020 IEEE Radiation Effects Data Workshop (in conjunction with 2020 NSREC)*. 2020, pp. 1–8. DOI: 10.1109/REDW51883.2020.9325822.

[89] F. Wrobel et al. “The Power Law Shape of Heavy Ions Experimental Cross Section”. In: *IEEE Transactions on Nuclear Science* 64.1 (2017), pp. 427–433. DOI: 10.1109/TNS.2016.2608004.

[90] Michel Kruglanski et al. “Last upgrades and development of the space environment information system (SPENVIS)”. In: *2009 European Conference on Radiation and Its Effects on Components and Systems*. 2009, pp. 563–565. DOI: 10.1109/RADECS.2009.5994715.

[91] P. Roche et al. “Application of the TIARA Radiation Transport Tool to Single Event Effects Simulation”. In: *IEEE Transactions on Nuclear Science* 61.3 (2014), pp. 1498–1500. DOI: 10.1109/TNS.2014.2318778.

[92] Robert A. Reed et al. “Physical Processes and Applications of the Monte Carlo Radiative Energy Deposition (MRED) Code”. In: *IEEE Transactions on Nuclear Science* 62.4 (2015), pp. 1441–1461. DOI: 10.1109/TNS.2015.2454446.

[93] Ketil Roed et al. “FLUKA Simulations for SEE Studies of Critical LHC Underground Areas”. In: *IEEE Transactions on Nuclear Science* 58.3 (2011), pp. 932–938. DOI: 10.1109/TNS.2010.2097605.

[94] Ygor Q. Aguiar et al. “Mitigation and Predictive Assessment of SET Immunity of Digital Logic Circuits for Space Missions”. In: *Aerospace* 7.2 (2020). ISSN: 2226-4310. DOI: 10.3390/aerospace7020012. URL: https://www.mdpi.com/2226-4310/7/2/12.

[95] Frédéric Wrobel et al. “Soft Error Triggering Criterion Based on Simplified Electrical Model of the SRAM Cell”. In: *IEEE Transactions on Nuclear Science* 60.4 (2013), pp. 2537–2541. DOI: 10.1109/TNS.2012.2235148.

[96] Matteo Cecchetto et al. “0.1–10 MeV Neutron Soft Error Rate in Accelerator and Atmospheric Environments”. In: *IEEE Transactions on Nuclear Science* 68.5 (2021), pp. 873–883. DOI: 10.1109/TNS.2021.3064666.

[97] T. Merelle et al. “Criterion for SEU occurrence in SRAM deduced from circuit and device Simulations in case of neutron-induced SER”. In: *IEEE Transactions on Nuclear Science* 52.4 (2005), pp. 1148–1155. DOI: 10.1109/TNS.2005.852319.

[98] Cleiton M. Marques et al. “Evaluation of a Simplified Modeling Approach for SEE Cross-Section Prediction: A Case Study of SEU on 6T SRAM Cells”. In: *Electronics* 13.10 (2024). ISSN: 2079-9292. DOI: 10.3390/electronics13101954. URL: https://www.mdpi.com/2079-9292/13/10/1954.

[99] A. Pavlov and M. Sachdev. *CMOS SRAM Circuit Design and Parametric Test in Nano-Scaled Technologies: Process-Aware SRAM Design and Test*. Springer Science and Business Media, 2008. DOI: ISBN0792379918.

[100] Mohanty S.P. Singh J. and D.K. Pradhan. *Robust SRAM Designs and Analysis*. Springer Science and Business Media, 2012. DOI: 10.1007/978-1-4614-0818-5.

[101] Jialei Wang et al. “Study of SEU Sensitivity of SRAM-Based Radiation Monitors in 65-nm CMOS”. In: *IEEE Transactions on Nuclear Science* 68.5 (2021), pp. 913–920. DOI: 10.1109/TNS.2021.3072328.

[102] Randy W. Mann and Benton H. Calhoun. “New category of ultra-thin notchless 6T SRAM cell layout topologies for sub-22nm”. In: *2011 12th International Symposium on Quality Electronic Design*. 2011, pp. 1–6. DOI: 10.1109/ISQED.2011.5770761.

[103] Ghasem Pasandi and Sied Mehdi Fakhraie. “A new VDD- and GND-floating rails SRAM with improved read SNM and without multi-level voltage regulator”. In: *2014 22nd Iranian Conference on Electrical Engineering (ICEE)*. 2014, pp. 377–381. DOI: 10.1109/IranianCEE.2014.6999568.

[104] F. Boeuf et al. “0.248/spl mu/m/sup 2/ and 0.334/spl mu/m/sup 2/ conventional bulk 6T-SRAM bit-cells for 45nm node low cost - general purpose applications”. In: *Digest of Technical Papers. 2005 Symposium on VLSI Technology, 2005.* 2005, pp. 130–131. DOI: 10.1109/.2005.1469240.

[105] Balobas D. Apostolidis G. and N. Konofaos. “Design and simulation of 6T SRAM cell architectures in 32nm technology”. In: *Journal of Engineering Science and Technology Review*. 2016, pp. 145–149. DOI: 10.25103/jestr.095.23.

[106] Gary M. Swift et al. “Static Upset Characteristics of the 90nm Virtex-4QV FPGAs”. In: *2008 IEEE Radiation Effects Data Workshop*. 2008, pp. 98–105. DOI: 10.1109/REDW.2008.25.

[107] C. Weulersse et al. “Prediction of proton cross sections for SEU in SRAMs and SDRAMs using the METIS engineer tool”. In: *Microelectronics Reliability* 55.9 (2015). Proceedings of the 26th European Symposium on Reliability of Electron Devices, Failure Physics and Analysis, pp. 1491–1495. ISSN: 0026-2714. DOI: https://doi.org/10.1016/j.microrel.2015.06.117. URL: https://www.sciencedirect.com/science/article/pii/S0026271415300718.

[108] Slawosz Uznanski et al. “Heavy Ion Characterization and Monte Carlo Simulation on 32 nm CMOS Bulk Technology”. In: *IEEE Transactions on Nuclear Science* 58.6 (2011), pp. 2652–2657. DOI: 10.1109/TNS.2011.2170852.

[109] E. H. Cannon et al. “Heavy Ion, High-Energy, and Low-Energy Proton SEE Sensitivity of 90-nm RHBD SRAMs”. In: *IEEE Transactions on Nuclear Science* 57.6 (2010), pp. 3493–3499. DOI: 10.1109/TNS.2010.2086482.

[110] Daisuke Kobayashi. “Scaling Trends of Digital Single-Event Effects: A Survey of SEU and SET Parameters and Comparison With Transistor Performance”. In: *IEEE Transactions on Nuclear Science* 68.2 (2021), pp. 124–148. DOI: 10.1109/TNS.2020.3044659.

[111] M. Raine et al. “Estimation of the Single-Event Upset Sensitivity of Advanced SOI SRAMs”. In: *IEEE Transactions on Nuclear Science* 65.1 (2018), pp. 339–345. DOI: 10.1109/TNS.2017.2779786.

[112] S. Guagliardo et al. “Single Event Latchup Cross Section Calculation from TCAD Simulations - Effects of the Doping Profiles and Anode to Cathode Spacing”. In: *2019 19th European Conference on Radiation and Its Effects on Components and Systems (RADECS)*. 2019, pp. 01–05. DOI: 10.1109/RADECS47380.2019.9745682.

[113] Patrick Nsengiyumva et al. “A Comparison of the SEU Response of Planar and FinFET D Flip-Flops at Advanced Technology Nodes”. In: *IEEE Transactions on Nuclear Science* 63.1 (2016), pp. 266–272. DOI: 10.1109/TNS.2015.2508981.

[114] A. Michez, S. Dhombres, and J. Boch. “ECORCE: A TCAD Tool for Total Ionizing Dose and Single Event Effect Modeling”. In: *IEEE Transactions on Nuclear Science* 62.4 (2015), pp. 1516–1527. DOI: 10.1109/TNS.2015.2449281.

[115] Slawosz Uznanski et al. “Single Event Upset and Multiple Cell Upset Modeling in Commercial Bulk 65-nm CMOS SRAMs and Flip-Flops”. In: *IEEE Transactions on Nuclear Science* 57.4 (2010), pp. 1876–1883. DOI: 10.1109/TNS.2010.2051039.

[116] Pavel Hazdra et al. “Radiation Resistance of High-Voltage Silicon and 4H-SiC Power p-i-n Diodes”. In: *IEEE Transactions on Electron Devices* 68.1 (2021), pp. 202–207. DOI: 10.1109/TED.2020.3038713.

[117] Bangyao Mao et al. “Nondestructive Spectroscopic Investigation of N-Type 4H-SiC Defects Irradiated With Low Fluence 16.5 MeV/u Ta Ions”. In: *IEEE Transactions on Nuclear Science* 71.2 (2024), pp. 154–159. DOI: 10.1109/TNS.2024.3359261.

[118] Satoshi Kuboyama et al. “Anomalous Charge Collection in Silicon Carbide Schottky Barrier Diodes and Resulting Permanent Damage and Single-Event Burnout”. In: *IEEE Transactions on Nuclear Science* 53.6 (2006), pp. 3343–3348. DOI: 10.1109/TNS.2006.885165.

[119] Arto Javanainen et al. “Heavy-Ion-Induced Degradation in SiC Schottky Diodes: Incident Angle and Energy Deposition Dependence”. In: *IEEE Transactions on Nuclear Science* 64.8 (2017), pp. 2031–2037. DOI: 10.1109/TNS.2017.2717045.

[120] A. Akturk et al. “Terrestrial Neutron-Induced Failures in Silicon Carbide Power MOSFETs and Diodes”. In: *IEEE Transactions on Nuclear Science* 65.6 (2018), pp. 1248–1254. DOI: 10.1109/TNS.2018.2833741.

[121] C. Martinella et al. “Heavy-Ion Microbeam Studies of Single-Event Leakage Current Mechanism in SiC VD-MOSFETs”. In: *IEEE Transactions on Nuclear Science* 67.7 (2020), pp. 1381–1389. DOI: 10.1109/TNS.2020.3002729.

[122] Chao Peng. “Study on Failure Mechanisms of SiC Power Devices Induced by Heavy Ion Irradiation”. In: *2023 5th International Conference on Radiation Effects of Electronic Devices (ICREED)*. 2023, pp. 1–5. DOI: 10.1109/ICREED59404.2023.10390869.

[123] Islam S.M. Kumar S. et al. Shekhawat R.S. “Fabrication and Characterization of a Silicon Carbide Based Schottky Barrier Diode”. In: *J. Electron. Mater.* 52 (2023), 7221–7229. DOI: 10.1007/s11664-023-10647-9.

[124] Satoshi Kuboyama et al. “Thermal Runaway in SiC Schottky Barrier Diodes Caused by Heavy Ions”. In: *IEEE Transactions on Nuclear Science* 66.7 (2019), pp. 1688–1693. DOI: 10.1109/TNS.2019.2914494.

[125] Michael E Levinshtein, Sergey L Rumyantsev, and Michael S Shur. *Properties of Advanced Semiconductor Materials: GaN, AIN, InN, BN, SiC, SiGe*. John Wiley & Sons, 2001.

[126] TT Mnatsakanov et al. “Carrier mobility model for simulation of SiC-based electronic devices”. In: *Semiconductor science and technology* 17.9 (2002), p. 974.

[127] Matthias Roschke and Frank Schwierz. “Electron mobility models for 4H, 6H, and 3C SiC [MESFETs]”. In: *IEEE Transactions on electron devices* 48.7 (2001), pp. 1442–1447.

[128] Tetsuo Hatakeyama. “Measurements of impact ionization coefficients of electrons and holes in 4H-SiC and their application to device simulation”. In: *physica status solidi (a)* 206.10 (2009), pp. 2284–2294.

[129] Hong Zhang et al. “Sensitivity of heavy-ion-induced single event burnout in SiC MOSFET”. In: *Chinese Physics B* 31.1 (2022), p. 018501.

[130] Hideharu Matsuura et al. “Dependence of acceptor levels and hole mobility on acceptor density and temperature in Al-doped p-type 4H-SiC epilayers”. In: *Journal of Applied Physics* 96.5 (2004), pp. 2708–2715.

[131] Faisal Mehmood Shah et al. “Comparative performance evaluation of temperature dependent characteristics and power converter using GaN, SiC and Si power devices”. In: *2018 IEEE 12th International Conference on Compatibility, Power Electronics and Power Engineering (CPE-POWERENG 2018)*. 2018, pp. 1–7. DOI: 10.1109/CPE.2018.8372523.

[132] Davide Cittanti, Enrico Vico, and Iustin Radu Bojoi. "New FOM-Based Performance Evaluation of 600/650 V SiC and GaN Semiconductors for Next-Generation EV Drives". In: *IEEE Access* 10 (2022), pp. 51693–51707. DOI: 10.1109/ACCESS.2022.3174777.

[133] Olivier Deblecker, Zacharie De Grève, and Christophe Versèle. "Comparative study of optimally designed DC-DC converters with SiC and Si power devices". In: *Advanced Silicon Carbide Devices and Processing* (2015), pp. 143–173.

[134] Y Okuto and CR Crowell. "Threshold energy effect on avalanche breakdown voltage in semiconductor junctions". In: *Solid-State Electronics* 18.2 (1975), pp. 161–168.

[135] Yutoku Murakami et al. "Theoretical analysis of tunneling current in 4H-SiC Schottky barrier diodes under reverse-biased conditions based on the complex band structure". In: *Japanese Journal of Applied Physics* 62.SC (2023), SC1042.

[136] RADNEXT. "Deliverables reports". In: URL: https://radnext.web.cern.ch/deliverables/.

[137] Carlo Cazzaniga et al. "Fast Neutron Measurements for the Characterization of the ChipIr Beamline". In: *IEEE Transactions on Nuclear Science* 71.8 (2024), pp. 1520–1526. DOI: 10.1109/TNS.2024.3416540.

[138] André M. P. Mattos et al. "Using HARV-SoC for Reliable Sensing Applications in Radiation Harsh Environments". In: *2023 9th International Workshop on Advances in Sensors and Interfaces (IWASI)*. 2023, pp. 227–232. DOI: 10.1109/IWASI58316.2023.10164578.

[139] trenzfpga. "TE0725 - Technical Reference Manual". In: URL: https://wiki.trenz-electronic.de/display/PD/TE0725+TRM.